HIGH TEMPERATURE MECHANICAL SPECTROSCOPY OF FINE-GRAINED ZIRCONIA AND ALUMINA CONTAINING NANO-SIZED REINFORCEMENTS

THÈSE N^O 3994 (2008)

PRÉSENTÉE LE 11 JANVIER 2008
À LA FACULTÉ DES SCIENCES DE BASE
LABORATOIRE DE NANOSTRUCTURES ET NOUVEAUX MATÉRIAUX ÉLECTRONIQUE
PROGRAMME DOCTORAL EN PHYSIQUE

ÉCOLE POLYTECHNIQUE FÉDÉRALE DE LAUSANNE

POUR L'OBTENTION DU GRADE DE DOCTEUR ÈS SCIENCES

PAR

Claudia IONASCU

Physicienne diplômée de l'Université ouest de Timisoara, Roumanie
et de nationalité roumaine

acceptée sur proposition du jury:

Prof. G. Meylan, président du jury
Prof. R. Schaller, directeur de thèse
Dr N. Baluc, rapporteur
Prof. G. Fantozzi, rapporteur
Prof. J. San Juan, rapporteur

ÉCOLE POLYTECHNIQUE
FÉDÉRALE DE LAUSANNE

Suisse
2008

Résumé

Des échantillons de zircone polycristalline (3Y-TZP) non-renforcée et renforcée avec des nanotubes de carbone multiparois (CNTs) ou des «whiskers» de carbure de silicium (SiCw) ou encore des nano-particules de carbure de silicium (SiCp) ont été élaborés et étudiés par spectroscopie mécanique, complétée par des observations de microscopie électronique et des essais de fluage. De plus, afin de comparer à la zircone, des échantillons d'alumine polycristalline, pure et dopée par des nano-particules de carbure de silicium, ont été également étudiés.

Le spectre des pertes mécaniques à hautes températures de la zircone 3Y-TZP présente un fond exponentiel (augmentation exponentielle avec la température) accompagné d'une diminution du module élastique de cisaillement au-dessus de 1200 K. Un pic de frottement intérieur qui se transforme en fond exponentiel apparaît dans les spectres obtenus en fonction de la fréquence (spectre isotherme). Le pic ne dépend pas de l'amplitude de la contrainte appliquée, tandis que l'augmentation exponentielle dépend de l'amplitude au-dessus d'un certain seuil. Ce résultat a pu être relié à la réaction d'interface nécessaire à l'accommodation de la déformation lors du fluage. Les pertes mécaniques à hautes températures dépendent aussi de la taille des grains. Plus petite est la taille de grain, plus élevées sont les pertes mécaniques. La présence d'impuretés dans la poudre de «départ» de la zircone conduit à un déplacement du spectre de perte mécanique vers de plus basses températures.

Le dopage de la zircone avec différentes quantités de CNTs a comme conséquence une diminution du niveau des pertes mécaniques par rapport à la zircone pure. Un pic de frottement intérieur qui évolue en un fond exponentiel apparaît dans le spectre des pertes mécaniques décrit en fonction de la température pour une concentration plus élevée de CNTs. Dopée avec des CNTs, la zircone présente une déformation plus faible que la zircone pure lors d'essais de fluage en compression.

Les additions de différentes quantités de whiskers de type SiCw à la zircone conduisent aussi à une diminution du niveau des pertes mécaniques. Un pic à haute température apparaît dans le spectre mesuré en fonction de la température. Ce pic est mieux résolu par rapport au fond pour une concentration plus élevée de SiCw. La courbe de fluage est inférieure dans la zircone dopée avec SiCw que dans la zircone pure. Les ajouts de SiCp à la zircone déplacent parfois le spectre des pertes mécaniques vers de plus basses températures. La zircone dopée avec différentes quantités de SiCp présente un pic ou des pics dans le

Résumé

spectre décrit en fonction de la température ou de la fréquence. La hauteur des pics dépend de la quantité de SiCp ajouté dans la zircone.

Semblable à la zircone, le spectre des pertes mécaniques de l'alumine se compose d'une augmentation du fond exponentiel et d'une diminution du module dynamique de cisaillement au-dessus de 1200 K. Des additions de SiCp abaissent le niveau des pertes mécaniques à haute température par rapport à l'alumine pure.

La déformation plastique à haute température de la zircone et de l'alumine est interprétée au moyen d'un modèle théorique de glissement aux joints de grains. Quand le glissement des joints de grains n'est pas limité par des obstacles comme les jonctions multiples, les aspérités ou autres défauts, le fluage de l'échantillon apparaît et un fond exponentiel caractérise le spectre des pertes mécaniques. L'ajout des renforts de taille nanométrique sur les joints de grains conduit à une diminution du fond exponentiel. Ceci signifie que le glissement aux joints de grains est plus difficile et par conséquent une meilleure résistance au fluage est observée.

Les valeurs des paramètres d'activation obtenues à partir des graphes d'Arrhenius sont apparentes. Deux méthodes ont été utilisées pour corriger ces valeurs apparentes. Cependant, même si les valeurs corrigées paraissent plus raisonnables que les valeurs obtenues à partir des graphes d'Arrhenius, elles n'apportent pas d'information exploitable. On admet alors que les valeurs apparemment trop élevées des paramètres d'activation rendent compte d'une microstructure changeante des joints de grains avec la température. L'évolution de la structure des joints de grains avec la température créerait des courts-circuits pour la diffusion, ce qui réduit l'effet d'ancrages des renforts nanométriques.

Mots-clés: spectroscopie mécanique, essai de fluage, microscopie électronique de balayage et de transmission, zircone, alumine, Nanotubes de carbone multi-parois, «whiskers» de carbure de silicium, nanoparticules de carbure de silicium.

Abstract

Polycrystalline zirconia (3Y-TZP grade) unreinforced and reinforced with mul-
tiwalled carbon nanotubes (CNTs) or silicon carbide whiskers (SiCw) or silicon
carbide particles (SiCp) have been processed and studied by mechanical spec-
troscopy with complementary observations of electron microscopy and creep
tests. Moreover, for comparison with zirconia, polycrystalline alumina speci-
mens, unreinforced and reinforced with silicon carbide nanoparticles, have also
been studied.

The high-temperature mechanical loss spectrum of pure zirconia presents an
exponential background (exponential increase with temperature) accompanied
by a decrease of the dynamic shear modulus above 1200 K. A dissipation peak,
which transforms into an exponential increase, appears in the spectra obtained
as a function of frequency (isothermal spectrum). The peak does not depend on
the amplitude of the applied stress, whereas the exponential increase is stress
dependent above a certain threshold. This result has been linked to the inter-
face reaction, which plays an important role in deformation accommodation
during creep. The high-temperature mechanical loss is grain size dependent.
Smaller the grain size, higher the mechanical loss. The presence of the impuri-
ties in the starting powder of zirconia leads to a shift of the entire mechani-
cal-loss spectrum towards lower temperatures.

Doping zirconia with different amounts of CNTs results in a decrease of the
isothermal-mechanical loss level with respect to pure zirconia. A dissipation
peak that transforms into an exponential increase is present for a higher
amount of CNTs in the mechanical-loss spectrum as a function of temperature.
Zirconia doped with CNTs exhibits a lower creep strain than pure zirconia
when submitted to a compressive stress at high temperature. Also, addition of
different amounts of SiCw to zirconia leads to a decrease of the mechanical-loss
level. A high-temperature dissipation peak is presents in the isochronal spec-
trum. The peak is better resolved for a higher amount of SiCw. The creep-strain
curve is lower in SiCw-doped zirconia than in pure zirconia at high tempera-
ture. Addition of SiCp to zirconia may shift or not the mechanical-loss spectrum
towards lower temperatures. Doping zirconia with different amounts of SiCp
results in the appearance of a peak or peaks in the high temperature isochronal
and isothermal spectrum. The height of the peaks depends on the amount of
SiCp to zirconia.

Similar to zirconia, the high-temperature mechanical loss spectrum of alumina
consists of an exponential increase of the mechanical loss and a decrease in the

Abstract

dynamic shear modulus above 1200 K. Additions of SiCp lower the high-temperature mechanical loss with respect to the one in pure alumina.

High-temperature plastic deformation of pure zirconia and alumina is interpreted in terms of a theoretical model of GB sliding. When GB sliding is not limited by obstacles like multiple junctions, GB asperities or other defects, creep occur and an exponential background is observed in the mechanical-loss spectrum. Addition of nano-sized reinforcements on the GBs results in a decrease of the exponential background. This means that the GB sliding is more difficult and as a consequence a better creep resistance is observed.

The activation parameters obtained from the Arrhenius plots were apparent. Two methods are used to correct the apparent values. However, even if the corrected values seem more reasonable than the values obtained from the Arrhenius plots, they do not bring useful information. It is proposed that apparent too high values of the activation enthalpy account for the evolution of the GB microstructure with temperature. Thermal evolution of the GB microstructure is believed to offer short circuit paths for GB diffusion, which allows the pinning nano-sized reinforcements to be overcome. Then pinning effect is less efficient.

Keywords: mechanical spectroscopy, creep test, scanning and transmission electron microscopy, zirconia, alumina, multiwalled carbon nanotubes, silicon carbide whiskers, silicon carbide particles.

Contents

Contents

Introduction

Ceramics make up a group of materials that has attracted a lot of interest in the last 30 years, although mankind used them probably since the existence of humanity (shaping clays, dishes, bricks, etc).

Ceramics are defined as any of various hard, brittle, heat- and corrosion-resistant materials made by firing clay or other minerals and consisting of one or more metals in combination with one or more nonmetals, usually including oxygen [1].

Ceramics can be subdivided in different groups considering the chemical composition, microstructure and their applications [2].
- From chemical composition (oxide, non-oxide) and atomic structure (glassy-amorphous, crystalline) point of view:
    - Silicate ceramics – glassy phase with a pronounced pore structure, such as SiO_2 with addition of Al_2O_3, MgO, BeO, ZrO_2, etc.
    - Oxide ceramics, such as ZrO_2, TiO_2, Al_2O_3, MgO, BeO.
    - Non-oxide, such as, nitrides, carbides, sialons, borides, etc.
- From applications point of view:
    - Traditional ceramics (pottery, bricks, sanitary, etc.).
    - Advanced ceramics, such as electronic ceramics (sensors, insulators, etc), optical ceramics (window, lasers), magnetic ceramics, structural ceramics (with applications in mechanical engineering, chemical engineering, biological technology) and special ceramics, such as reactor ceramics (absorbers, breeders, nuclear fuels).

Zirconium dioxide or *zirconia* (ZrO_2) is one of the most studied ceramic materials. It has a high melting point (2988 K) [3] and a low thermal conductivity. Pure zirconia has a monoclinic crystal structure at room temperature and transitions to tetragonal and cubic at increasing temperatures. The volume expansion associated with this polymorphic transformation induces very large stresses, and it will cause pure zirconia to crack during cooling from high temperatures. Several different oxides are added in a certain degree to pure zirconia to stabilize the tetragonal and/or cubic phases, such as Y_2O_3, Ce_2O_3, CaO, MgO [4-7]. Zirconia is very useful in its stabilized state. A special case is that of polycrystalline tetragonal zirconia (TZP) that is indicative of polycrystalline zirconia composed of only the metastable tetragonal phase. Stabilized zirconia is used as grinding media and engineering ceramics due to its hardness and high thermal shock resistance. It is also used in oxygen sensors and fuel cell

membranes because it has a unique ability to let the oxygen vacancy to move freely through the crystal structure at high temperatures. This ionic conductivity (and low electronic conductivity) make it one of the most useful electroceramics [8]. Another application is the production of subframes for the construction of dental restorations such as crowns and bridges. Apple Computer filed a patent for using zirconia casing for mobile devices [9].

Aluminium oxide or *alumina* (Al_2O_3) is a good thermal and electrical insulator. It has a high melting point (2327 K) [3]. It mostly occurs in the crystalline form called α-alumina or corundum. Its hardness makes it suitable for use as abrasive and a component for cutting tools. It is also used as storage medium for the purposes of fuel generation.

The fine-grained ceramics, such as Al_2O_3, Y_2O_3-stabilized ZrO_2, etc, are usually processed via a powder metallurgy method, for example hot pressing or cold uniaxial pressing followed by sintering of the powder compacts. Dense materials can be obtained by this method with a density almost equal to the theoretical one and grain sizes less than one micron.

The high-temperature mechanical behavior of fine-grained ceramics is strongly connected to the microstructure (shape of the grains, grain size and interface between the grains). The grain boundaries (GBs) could be clean or wetted with a thin amorphous layer resulting from sintering aids [10, 11].

As a consequence, the GBs play a crucial role in the high-temperature ductility or even structural superplasticity of polycrystalline ceramics [12-17]. One important property is that the grains retain their initial shape even after large elongations. This feature makes ceramics important candidates for different industrial applications, for instance preparation of components made by superplastic forming or by superplastic sintering forging like metals.

Nowadays, the GB sliding is recognized by the ceramic community as being the main mechanism responsible for the high-temperature deformation of polycrystalline ceramics [15, 16, 18-22]. Also, the GB sliding is the main mechanism for failure of the mechanical properties during the transition from brittle-to-ductile [23].

When GBs are wetted by an amorphous phase the sliding process is enhanced and the transition from brittle-to-ductile appears at lower temperatures. Hiraga [24] and Morita [25] have shown that by an addition of a small amount of SiO_2 the creep rate is increased 100 times in 3Y-TZP. However, the observation of this intergranular phase is very difficult at room temperature. The silica was observed in the multiple junctions after a certain SiO_2-addition to 3Y-TZP (> 0.3 wt. %) [25, 26]. When GBs are clean, the deformation also takes place by GB sliding. At the present time, the interpretation of the creep-controlling me-

chanism at high temperatures in ceramics, such as ZrO_2 and Al_2O_3, is still a subject of controversy.

The aim of this thesis work is to study the high-temperature deformation of 3 mol % yttria-stabilized tetragonal zirconia polycrystals (3Y-TZP): pure, impure and reinforced with different nano-sized inclusions, such as multiwalled carbon nanotubes or silicon carbide whiskers or silicon carbide particles. Moreover, with regard to zirconia ceramics, alumina undoped and reinforced with SiC particles is also studied. Nano-sized reinforcements are believed to pin the GBs, improving then the creep resistance of the ceramics. As mechanical spectroscopy is sensitive to GB sliding, it will be need to test the pinning efficiency of the mentioned nano-sized fibers or particles.

The mechanical spectroscopy is very sensitive to the dynamics of the structural defects and allows us to indentify the anelastic and microcreep phenomena that take place in materials. Together with the GB sliding, mechanical spectroscopy can also be used for investigating the accommodation processes accompanying the superplasticity.

Outline

Chapter1 presents a brief overview of the structural defects, plastic and even superplastic deformation in polycrystalline ceramics.

In *Chapter2,* the theoretical formalism of the mechanical spectroscopy and different relaxation models are discussed.

The preparation of the samples, microstructural analysis and the experimental setup are described in *Chapter 3*.

In *Chapter 4,* the experimental results obtained in zirconia pure, impure and doped with multiwalled carbon nanotubes or silicon carbide whiskers or silicon carbide particles are presented and analyzed. For comparison, the results obtained in alumina pure and doped with silicon carbide particles are presented.

Interpretation, discussions and possible further research are given in *Chapter 5*.

Chapter 1

Scientific background

1.1   Microstructure of ceramics

Crystalline materials contain structural defects, such as interstitial and substitutional atoms, vacancies, dislocations, grain boundaries and second phases. In polycrystalline ceramics most of the structural defects result from material processing. Ceramics are processed by powder metallurgy starting from very fine powders (sub-micrometric size). The resulting product of sintering is a fine-grained material. As a consequence, the most important structural defects in fine-grained ceramics are "grain boundaries" (GBs).

Depending on the purity of starting powders a viscous phase may appear in ceramics. This phase may be located along the GBs or collected in pockets at the GB junctions (Figure 1.1).
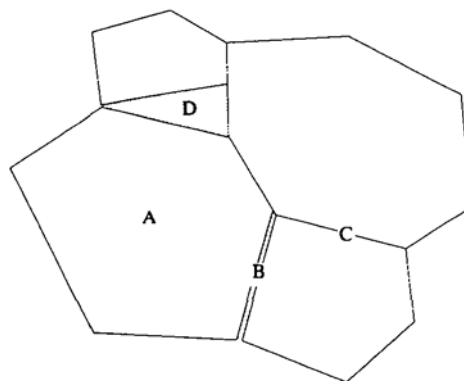
Figure 1.1: Schematic representation of a polycrystalline ceramic: A a grain, B an amorphous layer between two grains, C a clean GB and D an amorphous pocket at the triple junctions.

In general, structural defects determine the physical properties of solids, especially the mechanical ones. In ceramics, GBs play an important role in the mechanical properties. GB sliding at high temperature is responsible for plastic or even super-plastic deformation in fine-grained ceramics.

1.2 High-temperature plasticity of ceramics

At high temperature, plastic deformation of ceramics proceeds by mutually accommodating GB sliding and diffusion creep. According to which mechanism provides a greater amount of strain, one speaks of diffusion creep or GB sliding, but never dissociated. The plastic deformation depends on stress, temperature, and the material's history. The plastic flow or creep rate $\dot{\varepsilon}$ is generally described by a phenomenological equation of the form:

$$\dot{\varepsilon}(\sigma, T) \propto \sigma^n \left(\frac{1}{d}\right)^p exp\left(-\frac{\Delta H_{act}}{kT}\right) \qquad (1.1)$$

where σ is the applied stress, n the stress exponent, d the grain size, p the grain size exponent, ΔH_{act} the activation enthalpy, k the Boltzmann constant and T the temperature. The parameters n, p and ΔH_{act} are characteristic of the creep controlling mechanism.

The relation between GB sliding and diffusion creep is shown in Figure 1.2, where several hexagonal grains are subjected to a stress field. GB sliding creates voids or overlaps that have to be accommodated by diffusion. Indeed, diffusion creep creates the driving force for GB sliding and vice versa. These two processes are strongly coupled and mutually accommodated. Thus, one cannot exist without the other.
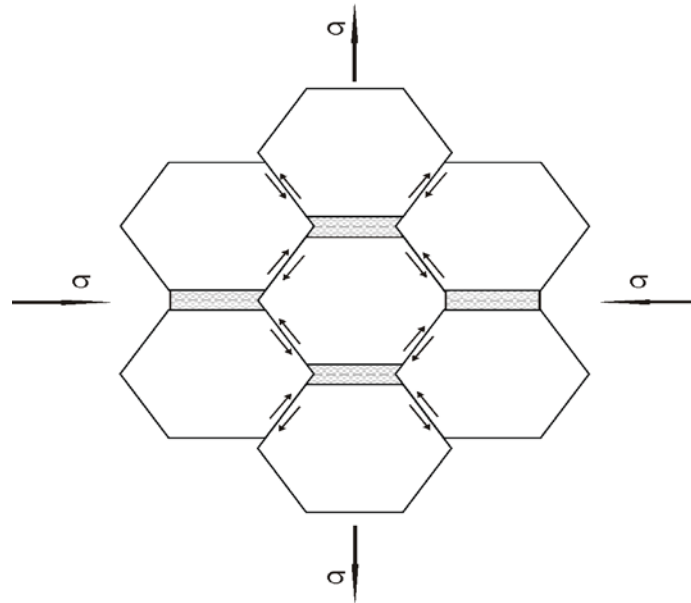

Figure 1.2: Deformed polycrystal under a stress field σ. GB sliding creates voids, which must be filled by diffusion.

When GB sliding involves only several contacting grains the deformation process is instantaneously accommodated during sliding. On the contrary,

when all the grains participate in sliding, the accommodation is not anymore instantaneous and it concurs with GB sliding. Sliding takes place until it is hindered by stronger obstacles, such as GB steps, asperities, triple junctions or second phase particles.

The accommodation processes are:
- Diffusion: flow of matter either through the bulk [27, 28] or along the GBs [29].
- Dislocation activity: emission of sub-boundary dislocations [30] or climbing of GB-dislocations [31, 32].
- A combination of both processes operating in parallel [33, 34].

Raj and Ashby [35] pointed out that in most of the cases Nabarro-Herring creep [27, 28] or Coble creep [29] are identical to GB sliding accommodated by diffusion.

1.2.1 Diffusion controlled creep

The deformation via diffusion controlled creep theories is based on the hypothesis that the surfaces or GBs are perfect sources and sinks of vacancy. The deformation rate is governed by the vacancy diffusion between sources and sinks. The driving force is the chemical potential (or partial molar free energy), which develops between specimen surfaces that come under tension and compression when the stress is applied. In this case the deformation is treated by two diffusion processes (Figure 1.3).
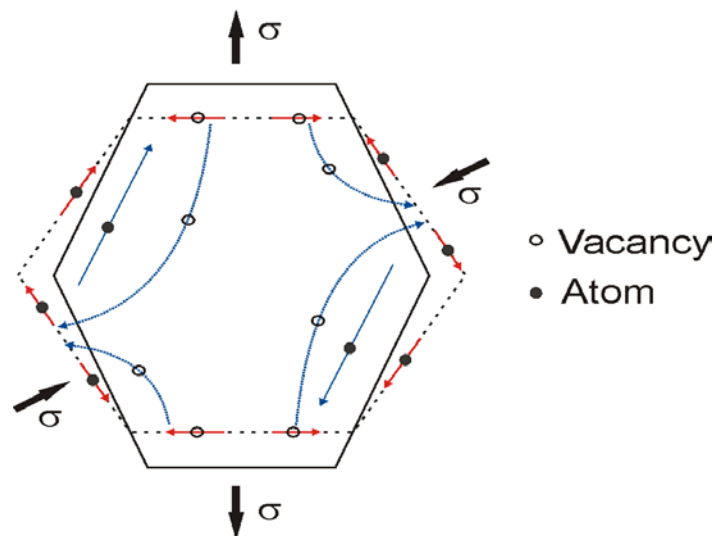

Figure 1.3: Schematic representation of the diffusion paths: one way is the migration of vacancy from boundaries in tension towards boundaries in compression and oppositely the transport of matter (Nabarro-Herring creep) and the other way along GBs (Coble creep).

One path way for diffusion is the vacancy migration from the boundaries under tension towards the ones under compression and transport of matter occurs in the opposite direction. As a result, the grains elongate in the direction of the tensile stress. This accommodation process is called Nabarro-Herring creep or volume diffusion creep [27, 28]. The second path way of matter transport, which is faster, is the diffusion along the GBs and it is called Coble creep [29].

The plastic flow or creep equations are:
- for Nabarro-Herring creep:

$$\dot{\varepsilon}(\sigma, T) \propto \frac{\sigma}{d^2} exp\left(-\frac{\Delta G_V}{kT}\right) \tag{1.2}$$

- for Coble creep :

$$\dot{\varepsilon}(\sigma, T) \propto \delta \frac{\sigma}{d^3} exp\left(-\frac{\Delta G_{GB}}{kT}\right) \tag{1.3}$$

where σ is the applied stress, d the grain size, δ the GB thickness, kT has the usual meaning, ΔG_V and ΔG_{GB} are the free activation enthalpies related to volume and GB diffusion, respectively.

The differences between the above diffusion processes lie in the activation enthalpy values (volume diffusion or along GBs) and in the fact that the plastic flow depends on d^{-2} in the case of Nabarro-Herring creep and on d^{-3} for Coble creep. Coble creep dominates Nabarro-Herring creep for small grain sizes and for low temperature.

1.2.2 Mutually accommodating grain-boundary sliding and diffusion creep

The mutually accommodating GB sliding and diffusion creep was first analyzed by Raj and Ashby [35]. They considered the general problem of sliding on a non-planar GB and, in particular, the cases of purely elastic and diffusion-accommodated GB sliding (Figure 1.4).

The transport of matter is induced by the difference in the chemical potential of the vacancies between boundaries in tension or compression. In this process the transport of matter takes place either through the bulk (volume) or along the GBs.
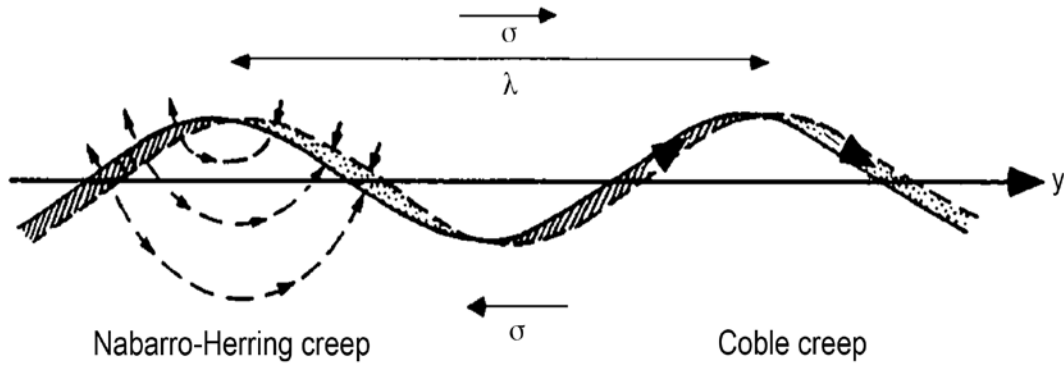
Figure 1.4: GB sliding accommodated by diffusion creep for a sinusoidal GB (after Raj and Ashby [35]).

Raj and Ashby [35] found for a polycrystalline material the following plastic flow equation:

$$\dot{\varepsilon} \propto \alpha \frac{\Omega}{kT} \frac{1}{d^2} \sigma \left(D_V + \frac{\pi \delta}{\lambda} D_{GB} \right) \qquad (1.4)$$

where α is a numerical factor, σ the applied stress, Ω the atomic volume, δ the GB thickness, λ the wavelength of sinusoidal profile of the GBs ($\lambda \sim 2d$), kT the usual meaning, D_V and D_{GB} are the volume and GB diffusion coefficients.

When the accommodation occurs by volume diffusion the equation (1.4) is similar to the one given by Nabarro-Herring creep (1.2). However, for GB diffusion alone, the equation (1.4) resembles to the one of Coble creep (1.3).

The creep rate is directly proportional to σ, d^{-2} in the case of lattice diffusion and to d^{-3} for GB diffusion.

1.2.3   Interface-reaction controlled creep

In the above models the GBs are considered as perfect sources and sinks of vacancy and the creep rate is as a result limited by the vacancy diffusion.

Artz et al. [32] developed a theoretical model taking into consideration the emission or absorption of vacancies by the GB-dislocations which are climbing in the GB plane. When the overall creep rate is lower than the diffusion creep rate we are dealing with an interface-reaction controlled mechanism. This model is applicable to "clean" GBs and with a high density of GB-dislocations (Figure 1.5).

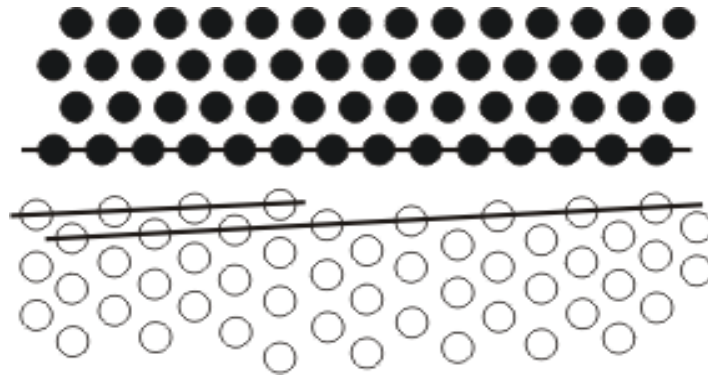*Figure 1.5: A GB-dislocation. The GB-dislocations are sources and sinks for vacancies. Dislocation motion controls the creep rate by emitting or absorbing vacancy. When the dislocation movement is limited by solute atoms, the controlling mechanisms are solute dragging or activation of dislocation spiral sources [33].*

To maintain the vacancy sources two conditions must be fulfilled:
- A constant density of the GB-dislocation. This is controlled by the activity of spiral GB-dislocation sources (Bardeen-Herring sources) [33].
- A high mobility of dislocations. It can be limited by friction or pinning forces exerted by impurities or GB precipitates.

By taking into consideration that the mobility of GB-dislocations is limited by solute dragging and that spiral sources are responsible for the creation of dislocations, Burton [33] found the following equation to express the plastic flow:

$$\dot{\varepsilon}(\sigma, T) \propto \frac{b_n}{CkT} \frac{\sigma^2}{d} D_S \qquad (1.5)$$

where b_n is the component of Burger's vector perpendicular to the GB plane, d the grain size, kT has the usual meaning, C and D_S are the solute concentration and diffusion coefficient, respectively. The activation enthalpy is equal to the diffusion enthalpy of solute atom.

In this case the creep rate is directly proportional to σ^2 and d^{-1}. However, in most of the polycrystalline ceramics the microstructure does not present a high dislocation activity and therefore the most important process involved in plastic deformation is diffusion creep.

1.2.4   Solution-precipitation controlled creep

A different situation arises in polycrystalline ceramics where the GBs contain a second phase, which can be amorphous or even liquid at high temperature [36-39]. This phase results either from the sintering aids (additives to improve

the sample density) or from liquid-forming impurities (Al$_2$O$_3$, SiO$_2$) added to the starting powder. The inter-granular phase is thermodynamically stable at high temperatures and has a thickness of the order of a few nanometers, typically 2 nm [10]. The deformation of polycrystalline materials with such an intergranular-glassy phase takes place by GB sliding accommodated by solution precipitation [40-43].

Raj and Chung [40] proposed an island model for the boundary surface to ensure that the boundary does not slide although lubricated by the glassy phase. In this model some regions have a good fit between adjacent grains and support the normal traction. The idea of the island model is that the atoms from one surface in compression dissolve into the glassy phase and diffuse through the boundary plane in the direction of the surface in tension, and then precipitates on this surface. This process is called solution-diffusion-precipitation creep (Figure 1.6).
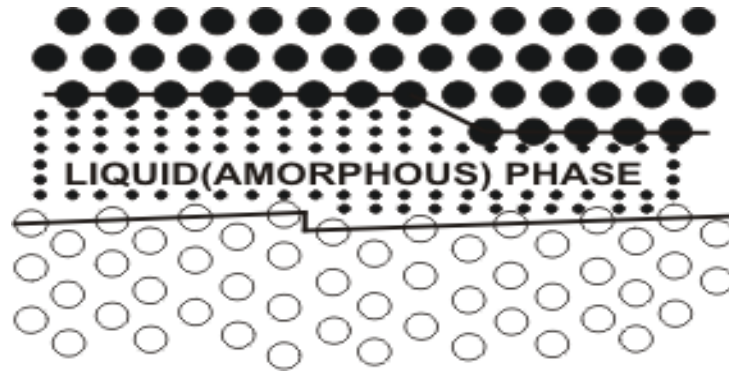
Figure 1.6: The intergranular phase controls the creep rate by providing a faster diffusion path for the atoms along the GBs. An atom from one boundary step dissolves into the phase, diffuses in the direction of the applied stress and precipitates on the other boundary (a new step is forming). The solution and precipitation of atoms results in step motion.

The plastic flow for interface-reaction controlled creep is given by:

$$\dot{\varepsilon}(\sigma, T) \propto \frac{\Omega^2}{kT} \frac{\sigma}{d} exp\left(-\frac{\Delta G_{diss}}{kT}\right) \qquad (1.6)$$

The plastic flow for diffusion-controlled creep, similar to the Coble's creep equation (1.3) is expressed as:

$$\dot{\varepsilon}(\sigma, T) \propto \delta \frac{\Omega}{kT} \frac{\sigma}{d^3} exp\left(-\frac{\Delta G_{GB}}{kT}\right) \qquad (1.7)$$

where σ is the applied stress, Ω the atomic volume, d the grain size, δ the GB thickness, kT has the usual meaning. ΔG_{diss} is the free activation en-

thalpy needed to detach an atom from a crystal ledge and to dissolve it into the glassy phase and ΔG_{GB} is the free activation enthalpy that is equal to the GB self-diffusion energy.

The creep rate is again directly proportional to σ and d^{-1} when creep is controlled by interface reaction or to d^{-3} when creep is controlled by GB diffusion.

Wakai [44] proposed a "step model" of solution-precipitation creep. The GBs play the role of sites of dissolution or precipitation and the deformation rate is controlled by the density and mobility of the steps. This model is analogous to the formalism concerning the GB-dislocations which are responsible for interface-reaction controlled creep in materials with "clean" GBs.

1.3   Superplasticity in fine-grained ceramics

Superplastic-like behavior is divided into two classes:
- Transformational superplasticity occurs with a change of phase during thermal cycling. For example, zirconia suffers this type of superplasticity during monoclinic-to-tetragonal transformation [45].
- Structural superplasticity or simple superplasticity takes place without a phase change.

Superplasticity is phenomenologically defined as the ability of a crystalline material to exhibit extremely large elongation in tension at elevated temperatures without necking, in other words, to achieve high ductility under tension prior to failure. The classical requirements for structural superplastic deformation are fine-grained structures and elevated temperatures, approximately above half of the absolute melting point. In ceramics, superplasticity appears at high temperature and relatively low applied stress (stress exponent n ≤ 2) for structures of fine equiaxed grains (grain size d < 1 μm) which are stable during deformation and do not exhibit any intergranular brittleness.

Ceramics such as oxides, nitrides, carbides and their composites are strong, hard, and stiff materials. They are known to be brittle and lack of ductility at room temperature. However, as discovered by Wakai in 1986 [13], fine-grained yttria stabilized zirconia polycrystals (Y-TZP) may reach very high-tensile ductility at high temperature. Such behavior refers to superplasticity and as a consequence, fine-grained ceramics present a large technical interest because of their shaping ability. Many investigations were performed not only on Y-TZP and its composites, but also in a wide range of fine-grained metals (grain size d < 10 μm), intermetallics and ceramics such as alumina, silicon carbide, silicon nitride, alumina-zirconia [46-48]. For example, a remarkably large elongation

of 2.510 % has been achieved at a high strain rate in zirconia composites by Kim et al. [49, 50]. The superplastic aspects can be used in industry to fabricate ceramic components by superplastic forming [51], superplastic forming concurrent with diffusion bonding and superplastic-sinter forging just like superplastic metals [21]. Moreover, superplasticity plays an essential role in stress assisted densification processes, for example hot-isostatic pressing and hot pressing.

Despite decades of investigation, the nature and the mechanism behind ceramic superplasticity is still not well understood.

1.3.1   Motion and topological evolution of grains

Polycrystalline ceramics may deform under the influence of an applied stress at high temperatures. A large strain results from GB sliding, which is mutually accommodated by the flux of matter along short-diffusion paths (diffusion transport of matter and the movement of lattice dislocations by glide and climb). On one hand, the large grains elongate along the stress axis during creep. On the other, fine grains retain their equiaxed shape even after large elongations (> 1000 %) superplastic-like behavior.

The structure of the GBs in polycrystalline ceramics has similar characteristics to those of oil emulsions and soap froth. Ashby and Verrall [52] developed a two-dimensional model for superplasticity from the observation of flow of soap froth and emulsions. They assumed that in polycrystals the deformation results from a neighboring-switching event. The change in configuration of a four-grain unit by GB sliding with diffusion-accommodation provides a large strain without appreciable deformation of the grains (Figure 1.7).
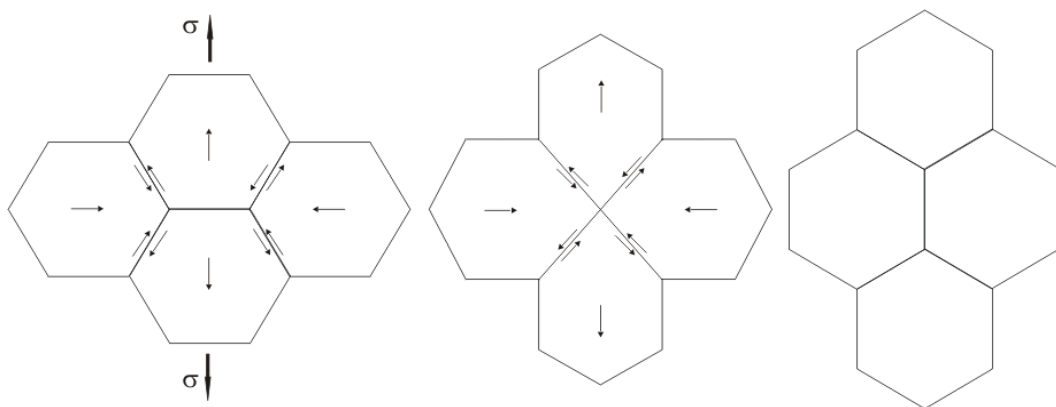

Figure 1.7: Topological model of superplasticity - a neighboring-switching event, where a group of four grains suffer a 55 % strain without deformation of the grains, except locally in the intermediate state to accommodate GB sliding (after Ashby and Verrall [52]).

The initial and final states are thermodynamically identical, although the poly-crystal has been strained by 55 %. There are four irreversible processes which contribute to the creep rate:

- GB sliding accommodated by transport of matter.
- Interface-reaction, expressing that the GBs are not perfect sources and sinks of vacancies.
- GB sliding itself.
- Fluctuation of GB area.

By omitting the interface-reaction processes, Ashby and Verrall [52] found for the creep rate:

$$\dot{\varepsilon}(\sigma, T) = 100 \frac{\Omega}{kT} \frac{1}{d^2} \left(\sigma - \frac{0.72 \Gamma_{GB}}{d}\right) D_V \left(1 + \frac{3.33\delta}{d} \frac{D_{GB}}{D_V}\right) \quad (1.8)$$

where Γ_{GB} is the GB energy, d is the grain size, δ the thickness of the GB, D_V the lattice diffusion coefficient, D_{GB} the GB diffusion coefficient.

The term $0.72\Gamma_{GB}/d$ gives the maximum back stress (threshold stress) in the grain-switching event during which all the grains change their shape instanta-neously. With the exception of threshold stress the equation (1.8) looks very much like the expression (1.4) given for the GB sliding accommodated both by lattice and GB diffusion.

Another model based on diffusion creep was proposed by Gifkins [53] where the grains are composed of a central part, called "core" and a boundary part, called "mantle" (Figure 1.8).

$$\gamma = 0 \qquad\qquad \gamma = 0.58 \qquad\qquad \gamma = 1.15$$
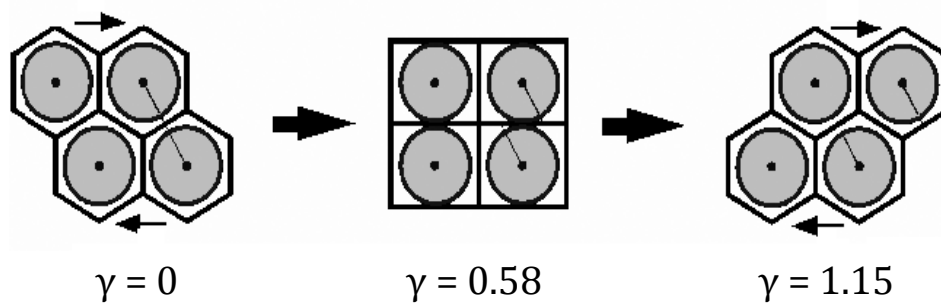
Figure 1.8: Shear deformation in a regular array of grains by Gifkins's "core-mantle" model (after Wakai et al. [54, 55]).

Grains change their shape by deformation of the "mantle", while the "core" moves like a rigid body. The main advantage of this assumption is that the crit-ical strain γ, at which the grain switching occurs (the concept of the threshold stress is involved), is reduced from γ = 1.15 in Ashby and Verall's model to γ = 0.58 for Gifkins's one.

1.3.2   Physical characteristics of ceramic superplasticity

In superplasticity the grain compatibility is maintained during GB sliding by a concurrent-accommodation process, which involves diffusion, dislocation motion and GB migration. In most of the proposed models the accommodation is the rate controlling process.

The general equation of creep rate for the superplasticity of ceramics is given by:

$$\dot{\varepsilon}(\sigma, T) = A \left(\frac{\sigma - \sigma_0}{G}\right)^n \left(\frac{b}{d}\right)^p D \qquad (1.9)$$

where σ is the applied stress, σ_o the threshold stress (dependent on the nature of the GBs [56] and it is zero in many cases), G the shear modulus, n the stress exponent, b is the Burger's vector, d the grain size, p the grain size exponent and A a material constant. D is the diffusion coefficient expressed as $D = D_o exp(Q/kT)$, with D_o the pre-exponential factor, Q the activation energy, which accounts for the underlying controlling mechanism and kT has the usual meaning.

Most of the efforts are focused on the determination of the parameters n, p and Q in order to identify which mechanism controls the superplastic behavior of ceramics [21, 22, 38, 56-62].

The characteristic stress and grain size exponents accounting for different creep rate controlling mechanism are listed in Table 1.1.

Parameters Creep models	n	p
Nabarro-Herring creep	1	2
Coble creep	1	3
Interface-reaction	2	1
Solution-precipitation	1	1 or 3

Table 1.1: The exponents of stress n and inverse-grain size p of the different creep models.

1.4 Mechanical behavior of fine-grained ceramics

High-temperature plastic deformation of fine-grained ceramics may occur by GB sliding, intergranular-dislocation motion or stress-directed diffusion creep [16, 17, 20-22, 46, 56-58, 63-68]. In the presence of an intergranular-amorphous (glass) phase the plastic deformation may occur by solution precipitation [40] or void formation [69].

The high-temperature mechanical behavior of materials, in this case structural ceramics is generally expressed using a steady state creep equation (1.9). The rate-controlling deformation process is usually determined by comparison of the experimental mechanical characteristics (stress exponent n, grain size exponent p and activation energy Q) with the existing theoretical models and the appropriate microstructure characterization.

1.4.1 Polycrystalline zirconia

Since 1986 when Wakai et al. [13] have reported that 3 mol %-yttria stabilized tetragonal zirconia fine-grained polycrystals (3Y-TZP) may exhibit large ductility of more than 120 %, considerable effort has been devoted to understand the superplastic behavior of ceramics [13, 16, 56, 70]. Most of the work has been concentrated on the submicron range of grain size, with 2-4 mol % yttria and at temperatures between 1273 K and 1723 K. Although creep parameters such as strain rate $\dot{\varepsilon}$, stress exponent n, grain size exponent p and activation energy Q are strongly affected by the impurity content [56, 63, 70, 71], the grain size d, the stress regime and the temperature range, GB sliding has been recognized as being the dominant mechanism in the superplastic deformation of ceramics [16, 19, 20, 56, 57, 70, 72, 73].

There are several models explaining the accommodation processes which accompany GB sliding [13], such as dislocation creep [74], interface-reaction controlled diffusion creep [44, 75], diffusion creep [76] and GB sliding with a threshold stress [22, 56, 77].

Several reviews are available concerning the thermo-mechanical behavior of zirconia ceramics and its microscopic interpretation [21, 56-58, 63, 78, 79]. A summary is given below:
- High purity zirconia grades:
  - At low stress $n > 2$ and $p \sim 1$, while at high stress $n = 2$ and $p = 3$.
  - The stress increases for the transition $n = 2$ to $n > 2$ when grain size and/or temperature decrease.
  - In the low stress regime n increases when the stress decreases.
  - The activation energy varies from 500 kJ/mol to 700 kJ/mol, when the stress decreases. No glassy phase enhancing GB diffusion was detected.

- Low purity zirconia grades: the impurity content of the sample can strongly affect the experimental results. For example the stress exponent $n = 2$ over the entire range of stress.

In high-purity Y-TZP the following values have been reported for the creep parameters at low temperatures and/or for fine-grain sizes in the low stress regime: $n = 2$–5 [22, 24, 56, 80, 81], $p \sim 0$ [22, 56] and $Q = 600$–700 kJ/mol [24, 56, 80-83].

In spite of the fact that the earlier studies speculated on the variation in deformation characteristics arising from the presence of amorphous phases at the GBs, recent studies have shown that there are variations in the deformation behavior even in the absence of an amorphous GB phase [73, 84, 85].

The differences in the creep parameters lead to different interpretations of the deformation mechanisms in 3Y-TZP [21, 58, 62, 63, 67]. Four interpretations have been proposed for the possible causes of the observed transition in the stress exponents ($n \simeq 2$ to $n > 2$):
1) Grain growth.
2) Operation of two-sequential processes: GB sliding and interface-controlled process.
3) GB sliding with a threshold stress.
4) Interface-controlled diffusion creep.

The interpretations will be discussed below:
1) Owen and Chokshi [57] reported a concurrent grain growth in 3Y-TZP. It was experimentally observed that in the low stress regime, where the concurrent grain growth is more pronounced, there is a decrease in the strain rate and an apparent increase in the stress exponent. Grain growth leads to significant grain rearrangement and switching, thus the grains retain their equiaxed shape even after a standard-diffusion creep deformation. The concurrent-grain growth and changes in the deformation mechanism lead to apparent values of creep parameters.

2) The approach using two sequential processes is based on the idea that there are two regions for creep: at low stress $n \sim 3$ and $p \sim 1$ and at high stress $n \sim 2$ and $p \sim 3$ [57, 58]. At low stress, deformation is controlled by an interface process [57, 73], while at high stress, deformation is controlled by GB sliding [63, 84]. As noted originally by Lifshitz, GB sliding must be accompanied by diffusion creep in order to maintain the grain adjacency. In this assumption, GB sliding can be considered to act as an accommodation process for diffusion creep and vice-versa.

The deformation rate is independent of the impurity content in the GB sliding

region. In the interface-reaction part the creep rate is strongly dependent on the impurity segregation at the GB (Y^{3+}, Al^{3+}, Si^{4+}). This approach has been rejected by some authors [22, 56, 78], because the activation energy is the same for both regions ($Q = 550$ kJ/mol [57, 58]). There is no physical meaning considering the same activation energy for two different processes, except by coincidence. Jiménez-Melendo and Domínguez-Rodríguez [59] have shown that the activation energy increases constantly when the stress decreases. On the other hand, the stress exponent is found to be constant and equal to $n = 3$ in the lower stress regime. This value is false because it was obtained by a classical creep plot ($log\dot{\varepsilon} - log\sigma$), by changing the strain rate when the stress is changed, n is no longer a constant. In a constant load experiment ($log\dot{\varepsilon} - log\varepsilon$) a large scale of n values ($n = 3 - 5$) have been obtained by many authors [15, 17, 22, 56, 82]. The operation of two sequential mechanisms is not consistent with the analysis of the available data in literature.

3) Jiménez-Melendo and Domínguez-Rodríguez [21, 56, 77] have explained the high-temperature superplastic like behavior of 3Y-TZP in terms of GB sliding with a threshold. A threshold stress is widely used to explain the conventional and high strain rate superplasticity of metallic alloys [86, 87]. In this approach the effective stress is not the applied stress σ, but rather $\sigma - \sigma_o$, where σ_o is the threshold stress. The transition from the high stress to the low stress regime is rationalized very well on the basis of a threshold stress σ_o. When $\sigma \simeq \sigma_o$, in the low stress regime n, p and Q are sensitive to σ_o. At high stress, n, p and Q are insensitive to σ_o.

Within this approach, the stress exponent is an apparent value n_{app}, which is expressed as:

$$n_{app} = 2\frac{log\left(\frac{\sigma_2-\sigma_0}{\sigma_1-\sigma_0}\right)}{log\left(\frac{\sigma_2}{\sigma_1}\right)} \qquad (1.10)$$

where σ_1 and σ_2 are the stresses before and after the jump. The apparent stress exponent increases when the stress is near σ_o [56, 78]. In analogy, the activation energy has an apparent value Q_{app} and can be written as:

$$Q_{app} = Q + 2R\frac{T_1 T_2}{T_1-T_2}\log\left(\frac{\sigma-\sigma_{0,T_2}}{\sigma-\sigma_{0,T_1}}\right) \qquad (1.11)$$

where Q is the true activation energy and σ_{o,T_1} and σ_{o,T_2} are the threshold stresses at the respective temperatures. The apparent activation energy will be equal to the true activation energy when the threshold stress is not a function of temperature. If the threshold stress is a decreasing function of temperature,

the apparent activation energy will increase when the applied stress decreases [56, 77]. Jiménez-Melendo and Domínguez-Rodríguez [59] have shown that the high-stress region is characterized by true values of $n = 2$, $p = 2$ and $Q = 460$ kJ/mol. On the contrary, at low stress all of the three parameters exhibit apparent evolution with the applied stress, grain size and temperature, for example $n > 4$, $p \sim 0$ and $Q > 650$ kJ/mol for lower temperatures and finer grain sizes. The authors derived the following constitutive equation for the GB sliding in high purity 3Y-TZP (for both high and low stress regions):

$$\dot{\varepsilon} = 3 \times 10^{10} \frac{(\sigma - \sigma_0)^2}{T d^2} exp\left(-\frac{460 kJ/mol}{RT}\right) \qquad (1.12)$$

with $\dot{\varepsilon}$ [s^{-1}], σ [MPa], T [K] and d [μm]. The threshold stress σ_o, which depends on temperature and grain size, is given by:

$$\sigma_0 = 5 \times 10^{-4} \frac{exp\left(-\frac{120 kJ/mol}{RT}\right)}{d} \qquad (1.13)$$

The equations (1.12) and (1.13) permit us to give a good interpretation of the stress exponent and the activation energy within the investigated stress and temperature domains.

The threshold stress in 3Y-TZP is temperature and grain size dependent. The activation energy is very close to the lattice diffusion [88, 89] suggesting that the superplasticity in zirconia could be due to GB sliding controlling the lattice diffusion of cation (D_{Zr}) [90].

Murty and Koczak [91] suggested that the threshold stress arises from the mechanism involving the impurity segregation at the GBs. It is believed that the interaction between GB-dislocations and solute atoms, for example yttria or other impurities, is responsible for the threshold stress. Under the application of an electric field (E ~ 1 V), the yttrium cations or other impurities are believed to segregate along the GBs. However, during creep test, the stress exponent did not change before and after the field onset. A flow-stress reduction was experimentally observed and an elongation increase with the application of the electric field. This phenomenon was interpreted by Murty and Koczak [91] as "E effect on the cation mobility along GBs".

The above approach has been largely criticized by some authors [57, 63, 92]. In the model of Jiménez-Melendo and Domínguez-Rodríguez [21, 56, 79] the threshold stress is evaluated from a linear plot $\dot{\varepsilon}^{0.5}$ vs. σ and the extrapolation of the data to zero strain rate gives σ_o. Two main reasons are invoked. First, analysis of the data yields a negative value of σ_o [57, 93] in the low and middle-to-high stress regions. However, a positive value of σ_o is obtained in

the higher stress region. Thus, this model is arbitrary and selective. Secondly, the influence of impurity content leads to a decrease in the transition stress. For example, a low-stress region (high-stress exponent) is not observed in a material with a large content of impurities. So, it is not worth to adopt directly the approach for superplastic metals in ceramics, in spite of the fact that they have similar transition from $n = 2$ to a higher value of n at low stresses.

Domínguez-Rodríguez et al. [90] have shown that the yttrium segregation at the GBs [73, 94-96] leads to a threshold stress that enables grains to slide around each other during deformation. The threshold stress is expressed as:

$$\sigma_0 \propto \frac{1}{d} exp\left(-\frac{2\Delta G}{RT}\right) \qquad (1.14)$$

The charge effect due to impurities segregation at the GBs justifies the existence of the threshold stress in the superplastic-like behavior of 3Y-TZP. It was experimentally observed that the charge effect gives the same grain size and temperature dependence [22, 56, 77].

4) The last approach is the interface-controlled diffusion creep as the rate controlling process proposed by Wakai and Nagano [71].

The standard diffusion models include:
- Nabarro-Herring [27, 28] creep, where the creep parameters are: $n \sim 1$, $p \sim 2$, and $Q = Q_{lattice}$, where $Q_{lattice}$ is the activation energy for lattice diffusion.
- Coble [29] creep, lead to $n = 1$, $p \sim 3$, and $Q = Q_{GB}$, where Q_{GB} is the activation energy for GB diffusion.
- Triple point diffusion in ultra-fine grained materials, where *n = 1*, *p ~ 4*, and $Q = Q_{TP}$, where Q_{TP} is the activation energy for creep along triple lines [63].

The diffusion creep is important at low stresses and in fine-grained materials. Pure diffusion creep is rejected by Owen and Chokshi [57] and Domínguez-Rodríguez et al. [79] because it is not consistent with the stress exponents in the two stress regimes ($n = 3$ and $n = 2$) and it also predicts a change in the microstructure. Scanning electron microscopy (SEM) images taken on 3Y-TZP showed the presence of equiaxed grains even after deformation at low and high stresses. Furthermore, a small aspect ratio is found after creep measurements. The diffusion creep hypothesis cannot be completely rejected because grain growth has been reported in some articles, and it is responsible for the apparent creep parameters.

Nieh et al. [97] suggested that viscous-intergranular dislocations creep is re-

sponsible for the calculated $n \sim 3$. Chokshi [70] observed from the comparison of results obtained in cubic zirconia with tetragonal zirconia, that dislocation creep rates are several orders of magnitude slower than the creep rate observed in 3Y-TZP. Consequently, these data cannot be justified in terms of an intergranular-dislocation creep mechanism.

Morita and Hiraga [98-100] studied the behavior of zirconia 3Y-TZP grade in the high and low stress regions and interpreted their data in terms of an intergranular-dislocation recovery mechanism at high stresses $16-80$ MPa with $n \sim 2.7$, $p \sim 2.3 - 3.3$, a threshold stress at intermediate stresses $9 - 16$ MPa, where $n \sim 5$ and a transition to Nabarro-Herring creep at low stresses ≤ 9 MPa, where $n \sim 1.3$ and $p \sim 1.8$. Activation energy of 580 kJ/mol was found and is the same for all three regions. Morita and Hiraga [100] proved by transmission electron microscopy (TEM), after the samples were cooled rapidly during load, that there is no amorphous phase either along GB or at triple points in 3Y-TZP. Above 15 MPa there was evidence for intergranular-dislocation activity and the density of the dislocation activity increases as the stress increases. At low stresses, Morita and Hiraga [100] supposed that there is a stress concentration at the triple junctions that increases the applied stress by factors of 14 - 25. They proved experimentally the stress concentration by documenting the presence of dislocations pile-up.

Balasubramian and Langdon [62] contested the pile-up theory for materials with submicrometer grain sizes. There are some inconsistencies in reproducing the calculations for different stresses and the number of dislocations reported in each intergranular pile-up creates problems.

Berbon and Langdon [92] suggested, taking into account the experimental results obtained by Owen and Chokshi [57] in 3Y-TZP, that the flow process occurs by Coble creep controlled by movement of the Zr^{4+} ions. Also, as a consequence of the small grain sizes, there is an interface-controlled diffusion creep. They developed a model based on Artz et al. assumptions [32], where the cores of the GB-dislocations are perfect sources and sinks for vacancies and furthermore that the dislocations are equally spaced in the boundary planes, thus all of them climb with the same speed. Under these conditions the Coble equation (1.3) is replaced by [32]:

$$\dot{\varepsilon} = 33.4 \frac{D_{Zr_{GB}} Gb}{RT} \left(\frac{\delta_{Zr}}{b} \right) \left(\frac{b^3}{d} \right) \left(\frac{\sigma}{G} \right) \left(\frac{N^2}{0.5 + N^2} \right) \qquad (1.15)$$

where $D_{ZrO_{GB}}$ is the GB diffusion coefficient for Zr^{4+} ion, N is the number of dislocations in a single GB wall. For coarse grains, N is large and $N^2/(N^2 + 0.5)$ is close to unity, thus the deformation takes place by a Coble mechanism. In fine-grained 3Y-TZP at low stress the additional term is reduced to the creep

rate $\dot{\varepsilon} \propto \sigma^3 D_{GB}/d$ modifying the stress exponent.

Berbon and Langdon [93] suggested that the flow occurs by Coble creep controlled by the movement of Zr^{4+} ions. Thus, for finer-grain sizes the diffusional creep is interface controlled.

Jiménez-Melendo and Domínguez-Rodríguez [59] as well as Owen and Chokshi [57] rejected this model for a few reasons. First, the model predicts that the stress exponent cannot be higher than $n \sim 3$, contrary with the observations that n is not a constant and can reach values of ~ 5 in 3Y-TZP [22, 56, 77, 81, 101, 102] and even of ~ 7 in zirconia single crystal [63], when the stress decreases. Secondly, the model predicts that the activation energy is constant and equal to $Q_{Zr_{GB}}$ in both high and low stress regions. This is not true because Q increases when the stress decreases [22, 56, 79]. It is generally accepted that during Coble creep the grains change their shape to reflect the overall strain within the sample. Some works consider that the grain shape and the grain size remain unchanged [19, 57, 77, 101, 102].

Charit and Chokshi [67] have shown that both the dislocation- and diffusion-creep processes contribute to material deformation. These two mechanisms have to be taken into consideration to interpret the results in ceramics. At very high stresses $\sigma \sim 200$ MPa they obtained a stress exponent $n \sim 7$ with the grain size remaining constant. They attributed the deformation in the very high-stress region to dislocation-controlled creep, according to the results obtained in a single crystal [103] and metallic alloys [104]. According to Charit and Chokshi [67] the creep parameters are different for different stress regions and characterized by:

- In the low stress region, $n \sim 2$, $p < 3$ and $Q \sim 480$ kJ/mol. Results are attributed to interface controlled Coble creep, similar to those described by Artz et al. [32].
- In the intermediate stress region, $n \sim 1$, $p \sim 3$ and $Q \approx 500$ kJ/mol. These values are consistent with Coble GB-diffusion creep.
- In the high stress region, $n \sim 7$ and $p < 1$. Deformation occurs by intergranular-dislocation controlled creep.

Addition of SiO_2 to 3Y-TZP leads to the formation of two distinct stress regions, in which the creep parameters depend on the silica content [24]. Silica additions lead to microstructural changes of 3Y-TZP and consequently, of creep parameters. It was observed that $\dot{\varepsilon}$, n and Q vary with silica content up to a threshold of 3 wt. %. The creep parameters remain almost constant after "saturation". Hiraga et al. [24] have shown that the creep parameters change until an equilibrium condition is reached, when the grains are surrounded by an intergranular-amorphous phase of thickness 0.8 μm. The surplus of silica is collected at the triple junctions forming glassy pockets.

Balasubramian and Longdon [61, 62] analyzed the data in 3Y-TZP and suggested that the movement of intergranular dislocations is not so important in the low stress regions. They developed a deformation-limit diagram using the Berbon and Langdon assumption [92], which provides good information over the entire stress regime. Figure 1.9 shows the deformation-limit diagram. This diagram provides a simple useful tool to interpret and predict the high-temperature experimental behavior of polycrystalline zirconia.
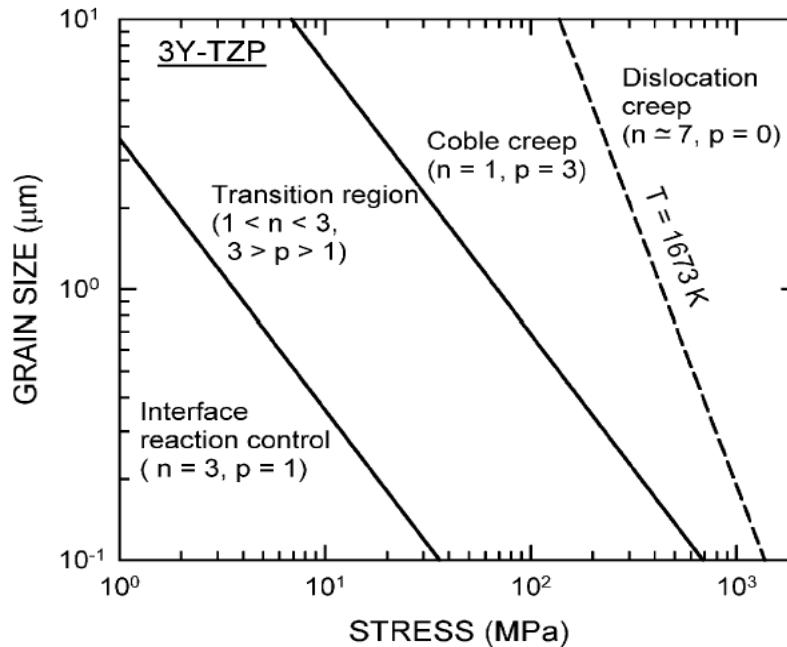

Figure 1.9: A useful tool is the "deformation-limit diagram" to interpret the high-temperature experimental behavior of 3Y-TZP (after Balasubramian and Langdon [61]).

A classification of the existing flow mechanisms in 3Y-TZP at 1673 K over the entire stress regions and for a creep rate of $\dot{\varepsilon} \sim 3 \cdot 10^{-2}$ are given below [61]:
- GB sliding at high stresses and interface-reaction controlled creep [62].
  - n increases from ~ 2 to ~ 3 with decreasing the stress.
  - p decreases from ~ 3 to ~ 1 with decreasing the stress.
  - Q is constant over the entire range of stress.
There is an intergranular-dislocation activity to accommodate GB sliding.
- GB sliding at high stresses and a threshold stress at low stresses [59].
  - p increases with decreasing stress, thus $n \to \infty$.
  - Q increases in the threshold stress region.
There is an intergranular-dislocation activity to accommodate GB sliding.
- Interface-controlled Coble diffusion creep at all stresses [92].
  - n increases from ~ 1 to ~ 3 with decreasing the stress.
  - p decreases from ~ 3 to ~ 1 with decreasing the stress.
  - Q is constant over the entire range of stresses.
There is no intergranular-dislocation activity.

- Dislocation-recovery mechanism at high stresses with a threshold stress and Nabarro-Herring diffusion creep at low stresses [105].
  - n increases with decreasing the stress at high stresses.
  - Q increases with decreasing the stresses at high stresses.
  - A transition to $n = 1$ at low stresses.

There is an intergranular-dislocation activity at stresses higher than 9 MPa, above the region of diffusion creep.

1.4.2 Polycrystalline alumina

Although the first study by tensile creep test in alumina was conducted more than 30 years ago by Davies and Sinha Ray [106], there was not so much interest in pursuing this aspect due to the apparently limited ductility of alumina. A review of literature indicates that there are some inconsistencies in the data reported in the literature as it concerns tensile deformation [107]. Although the influence of the grain growth on the creep parameters (n and Q) has been recognized in many studies, many authors did not include the appropriate correction for concurrent grain growth. It was found that polycrystalline alumina doped with magnesia with grain sizes bigger than 2 µm can suffer an elongation of 44 % (tensile deformation) [108]. It was observed in tensile tests that the grains remained equiaxed, the grains grow and cavitations occurred. A complete analysis of the data (taking into account the concurrent-grain growth) obtained in tensile and compression creep tests are summarized in Figure 1.10.
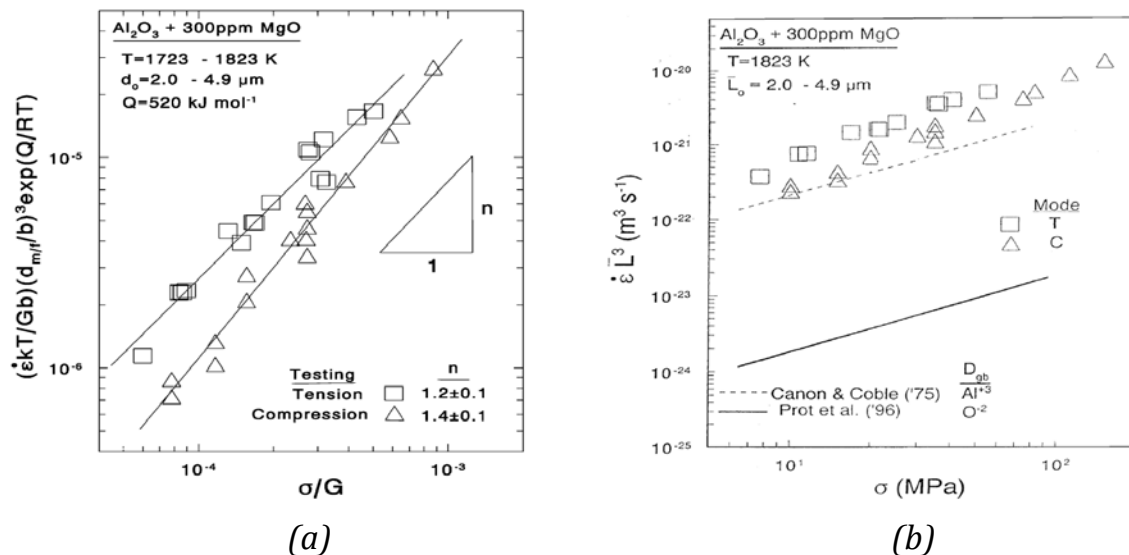

(a)	*(b)*

Figure 1.10: Tensile and compressive creep tests in polycrystalline Al₂O₃ (a) variation of $\dot{\varepsilon}$ with stress, (b) comparison of experimental and theoretical predictions of Coble creep using data for Al and O diffusion (after Chokshi [63]).

The obtained creep parameters were consistent with $n \sim 1$, $p \sim 3$ and $Q \sim 520$ kJ/mol [63]. Thus, the deformation mechanism takes place by Coble creep at high temperature. Unfortunately, there is not sufficient information

available in the literature for diffusion in alumina. In Figure 1.10b are shown the experimental data obtained at 1823 K together with the theoretical predictions for Coble creep using the activation energies of Al and O in the GBs diffusion [63]. Thus, the experimental data are in good agreement with Coble creep. On the contrary, the grains remain equiaxed even after plastic deformation, which is in conflict with grain elongation followed by diffusion creep.

Chokshi [63] proposed a model to solve this conflict. If there is significant grain growth, it will lead to grain switching and this process enables the maintenance of equiaxed grains during diffusion creep [109, 110].

1.4.3   Conclusions

There are a lot of publications concerning the creep behavior of fine-grained ceramics, such as zirconia and alumina. All the results have been discussed with respect to the values of the activation enthalpy ΔH_{act}, grain size exponent p and stress exponent n. Depending on the obtained values for these parameters, the authors have used one of the above mentioned models to interpret their results. It appears that there are many possible interpretations for the creep behavior of a nominally same ceramic, such as yttria doped zirconia. However, the different behaviors may originate in the different grades of zirconia of processed ceramics. As the creep behavior is related to GBs, it is than evident that the chemical composition of GBs plays an important role on the deformation mechanism. Moreover, the GB microstructure can evolve with temperature resulting in different creep mechanisms, which depends not only on stress, but also on temperature. A good indication of this evolution of GB microstructure with temperature is the fact that there is a large dispersion in the apparent values of the activation enthalpy.

In the present thesis work, the high-temperature behavior of fine-grained zirconia and alumina will be studied by mechanical spectroscopy, which means in the low stress regime (σ < 10 MPa). A particular attention will be paid to the stress and the grain size dependence of the mechanical-loss spectra in order to select one of the above interpretations.

Chapter 2

Theory of mechanical spectroscopy

This chapter reviews the fundamental theory of anelastic relaxation and the measurement techniques. Some examples of relaxation processes are presented and especially as it concern the high-temperature mechanical spectroscopy and its relevant examples from literature.

2.1 Relaxation - phenomenology

A relaxation phenomenon is the self-adjustment of a thermodynamic system with time towards a new equilibrium state under the change of an external variable. In other words, the relaxation occurs by the re-adjustment of the relaxed species (elastic dipoles, dislocation motion, GB sliding, etc.).

A relaxation process is described by a normalized relaxation function $\Psi(t)$ called Debye function that characterizes its evolution with time:

$$\Psi(t) = exp\left(-\frac{t}{\tau}\right) \tag{2.1}$$

where τ is the relaxation time. The equation (2.1) is valid only for independent relaxing species. Generally, when the relaxing species interact with each other, the relaxation process follows a Kohlrausch function [111] with a stretched exponential, $0 < \beta < 1$:

$$\Psi(t) = exp\left(-\frac{t}{\tau}\right)^{\beta} \tag{2.2}$$

The above expression was proposed by Kohlrausch as an empirical description of viscoelasticity [111].

2.2 Anelastic relaxation

The concept of anelastic relaxation was first described in 1948 by Zener [112]. The internal friction and mechanical spectroscopy are described in the book of Nowick and Berry [113] and more recently in the textbook of "Mechanical Spectroscopy Q^{-1} 2001" [114].

2.2.1 Standard anelastic solid

Anelasticity [113, 115] appears in the following simple experiment presented in Figure 2.1. A stress σ of a low intensity is applied abruptly to a specimen at time $t = 0$ and held constant during a time t_1. Strain ε is recorded as a function of time. One observes the instantaneous elastic strain $\varepsilon_e = J_u \sigma$, where J_u is the unrelaxed compliance, and the anelastic strain ε_a that increases with time from zero to an equilibrium value ε_a^∞. When equilibrium is reached, total strain $= \varepsilon_e + \varepsilon_a^\infty = J_r \sigma$, where J_r is the relaxed compliance. This evolution from one equilibrium state to a new one, under an applied stress, is called anelastic relaxation and may be defined by two parameters: the relaxation strength $\Delta = \varepsilon_a^\infty / \varepsilon_e = J_r - J_r / J_u$ and the relaxation time τ. If the stress is removed after a certain delay (time t_1 in Figure 2.1), one observes the instantaneous recovery of the elastic strain ε_e and with the relaxation time τ, the recovery of the anelastic strain. In such an experiment the strain is completely recoverable.
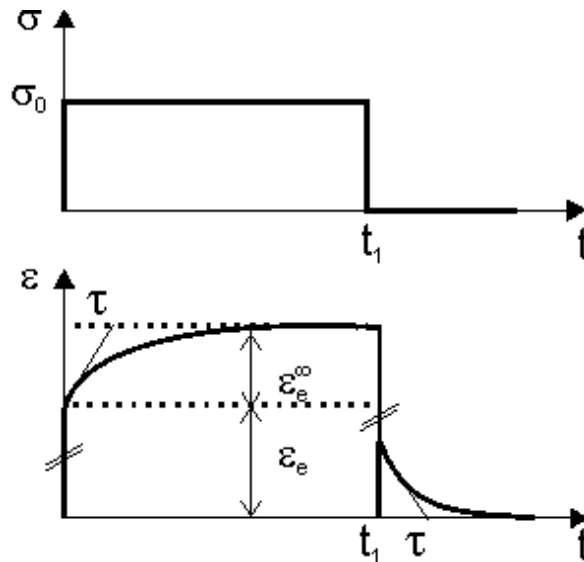

Figure 2.1: Elastic and anelastic strains of a solid submitted to a stress.

From a microscopic point of view, the anelastic strain can be interpreted as being due to the movements of structural defects (elastic dipoles, dislocations or interfaces) from one equilibrium position defined at $\sigma = 0$ to another one defined at σ. The relaxation strength Δ is then proportional to the concentra-

tion of defects that are relaxing and the relaxation time τ accounts for their mobility.

From a rheological point-of-view, the solid can be represented by the model shown in Figure 2.2.
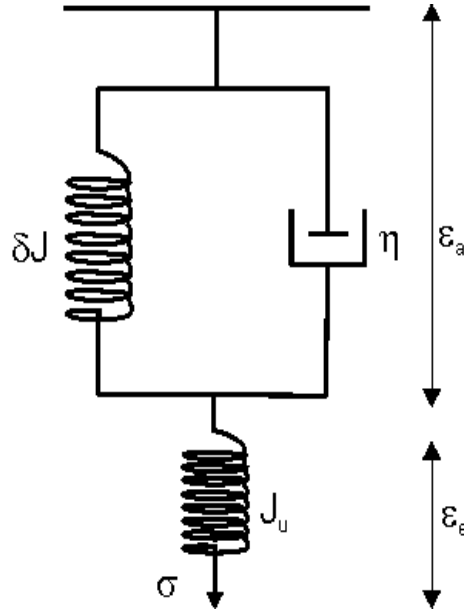

Figure 2.2: Rheological representation of the three-parameters standard anelastic solid. A dashpot is connected in parallel with a spring (Voigt-Kelvin model) having a constant of $\delta J = J_r - J_u$ and in parallel with another spring (Maxwell model) with a constant J_u.

The spring "$\delta J = J_r - J_u$" in parallel with the dashpot of viscosity $\eta = \tau/\delta J$ is essential for the recoverable nature of the anelastic strain. If the spring does not operate, the anelastic strain does not reach an equilibrium value and then is no longer completely recoverable.

The anelastic behavior in Figure 2.1 and Figure 2.2 is representative of the standard anelastic solid [113], the equation of motion which is:

$$J_r\sigma + J_u\tau\dot{\sigma} = \varepsilon + \tau\dot{\varepsilon} \qquad (2.3)$$

2.2.2 Mechanical spectroscopy

The measurements performed in the way described in §2.2.1 are very delicate and it is more convenient to use in practice dynamic methods for measuring the relaxation parameters. If an alternative stress of circular frequency ω (with $\omega = 2\pi f$, where f is the frequency) is applied to the system:

$$\sigma = \sigma_o exp(i\omega t) \tag{2.4}$$

the linearity of the stress-strain relationship ensures us that the strain ε is periodic with the same frequency:

$$\varepsilon = \varepsilon_o exp[i(\omega t - \Phi)] \tag{2.5}$$

with σ_o the stress amplitude, ε_o the strain amplitude and Φ the phase lag of strain behind stress (due to anelasticity) (Figure 2.3 and Figure 2.4).
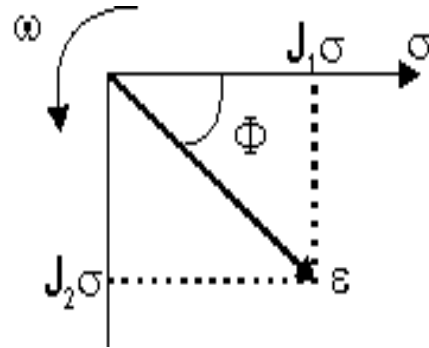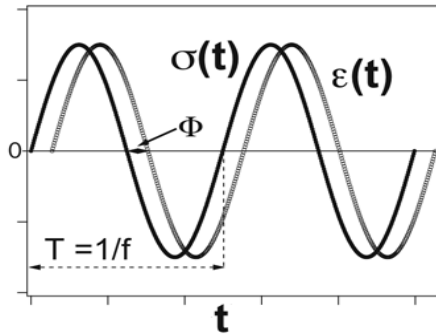

Figure 2.3: Schematic representation of an applied stress σ and a strain response ε as a function of time.

Figure 2.4: Vectorial representation of stress σ and strain ε. The diagram rotates around the origin with a circular frequency ω.

Introducing the equations (2.4) and (2.5) in equation (2.3) leads to the following relationship:

$$\varepsilon = \left[\left(J_u + \frac{J_r - J_u}{1 + \omega^2 \tau^2} - i\frac{(J_r - J_u)\omega\tau}{1 + \omega^2 \tau^2}\right)\right]\sigma = [J_1(\omega) - iJ_2(\omega)]\sigma = J^*(\omega)\sigma \tag{2.6}$$

where J_1 and J_2 are the real and imaginary parts of the complex compliance J^*, respectively.

In metals and ceramics, $J_r - J_u \ll J_u$ and the mechanical-loss angle is given by:

$$tan(\Phi) \cong \frac{J_2}{J_u} = \Delta \frac{\omega\tau}{1+\omega^2\tau^2} \tag{2.7}$$

and the variation of the dynamic compliance $\delta J/J_u$ (Figure 2.5) due to anelasticity by:

$$\frac{\delta J}{J_u} = \frac{J_1(\omega)-J_u}{J_u} = \Delta \frac{1}{1+\omega^2\tau^2} \tag{2.8}$$

The above equations (2.7) and (2.8) are called Debye's equations (first derived for dielectric relaxation phenomena) and describe the dynamic behavior of a solid. When the mechanical loss $tan(\Phi)$ is plotted as a function of $log(\omega\tau)$, a maximum of height $\Delta/2$ appears, centered at $\omega\tau = 1$ (Figure 2.5). This maximum (called Debye peak) gives us the relaxation strength $\Delta = \delta J/J_u$ (height of the peak) and the relaxation time τ (position of the peak on $\omega\tau$ axis).
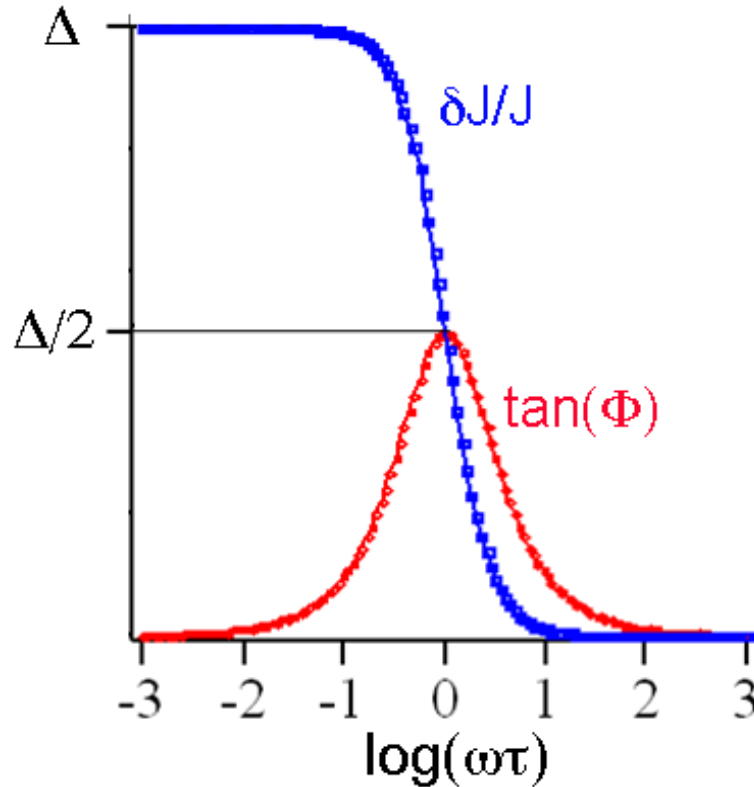

Figure 2.5: Mechanical loss $tan(\Phi)$ and modulus defect $\delta J/J_u$ as function of $log(\omega\tau)$. $tan(\Phi)$ has the form of a Debye peak with the maximum situated at $\omega\tau = 1$.

If several relaxation mechanisms are activated, the material exhibits a mechanical-loss spectrum composed of relaxation peaks, which inform us about the microstructure dynamics. In many cases, a distribution of the relaxation times has to be considered and then the mechanical loss is given by:

$$tan(\Phi) = \Delta \frac{(\omega\tau)^{\alpha}}{1+(\omega^2\tau^2)^{\alpha}} , \qquad 0 < \alpha \leq 1 \qquad (2.9)$$

where α is the broadening factor [116]. As most of the relaxation mechanisms are thermally activated, the relaxation time τ obeys an Arrhenius law:

$$\tau = \tau_o exp\left(\frac{\Delta H_{act}}{RT}\right) \qquad (2.10)$$

where τ_o is the limit relaxation time (inverse of the limit attempt frequency v_o), ΔH_{act} the activation enthalpy, characteristic of the energy barrier that the defects have to jump to reach the next equilibrium state, R the gas constant and T the absolute temperature. As a consequence, $tan(\Phi)$ can also be measured as a function of temperature with ω held constant and the curve $tan(\Phi) = \tan(\Phi)(T)$ is the mechanical-loss spectrum described as a function of temperature T.

By definition, the internal friction I.F. or internal damping is a measure of the energy which is dissipated in the solid and is expressed as:

$$I.F. = \frac{1}{2\pi} \frac{\Delta W_{diss}}{W_{el.max}} \qquad (2.11)$$

where ΔW_{diss} is the energy dissipated in a volume unit during one cycle of vibration:

$$\Delta W_{diss} = \oint \sigma d\varepsilon = \pi J_2 \sigma_0^2 \qquad (2.12)$$

and $W_{el.max}$ is the maximum stored elastic energy per unit volume:

$$W_{el.max} = \int_0^{\sigma_0} \sigma d\varepsilon = \frac{1}{2} J_1 \sigma_0^2 \qquad (2.13)$$

It follows immediately that:

$$I.F. = \frac{1}{2\pi} \frac{\pi J_2 \sigma_0^2}{\frac{1}{2} J_1 \sigma_0^2} = \frac{J_2}{J_1} = tan(\Phi) \qquad (2.14)$$

2.3 Examples of anelastic relaxations

2.3.1 Point defect relaxation

An elastic dipole is a point defect which produces a local distortion of the lattice. When an external stress is applied to the specimen, there will be a preferential reorientation of the elastic dipoles along the most favorable direction. This gives rise to anelastic strain [83, 113, 117].

Generally, it is accepted that ionic conductivity or diffusion in oxides of type MO_2 (ZrO_2, CeO_2, ThO_2) takes place by migration of oxygen vacancies on the anion sublattice. The oxygen vacancies are introduced by doping with lower valent cations, for example introducing Y_2O_3 in the above mentioned ceramics leads to the creation of one oxygen vacancies for every two yttrium cations. Yttrium cations associated with oxygen vacancy form elastic (and electric) dipoles. Under the application of a stress or electric field, these dipoles can reorientate giving rise to anelastic or dielectric relaxation peaks. An example of an elastic (and an electric) dipole in tetragonal-stabilized polycrystalline zirconia (i.e. Y_2O_3 - ZrO_2 system) is shown in Figure 2.6.
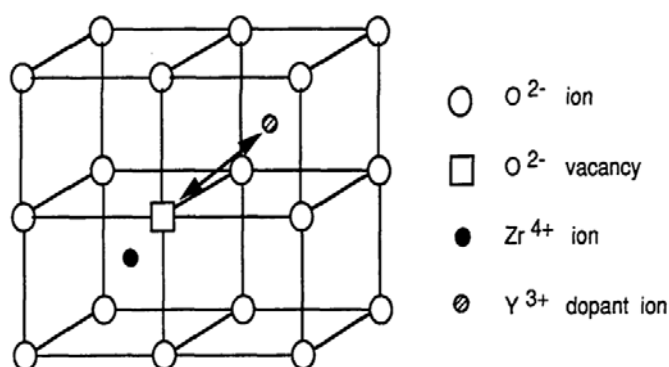

Figure 2.6: Diagram of one half unit cell of zirconia. Substitutional yttrium cation forming an elastic and electric dipole with an oxygen-ion vacancy (after Nowick and Berry [113] and Lakki [83, 118]).

Reorientation of the dipole occurs by jumping of oxygen vacancy around the immobile-yttrium cation causing an anelastic relaxation. Such a relaxation gives rise to a relaxation peak [83].

2.3.2 Dislocation relaxation

Dislocation string model

The dislocation string model accounts for dislocation relaxation, where a dislocation segment, which is fixed at two strong pinning points, bows under an applied stress (Figure 2.7). This model was first suggested by Koehler [119] and later developed by Granato and Lücke [120].
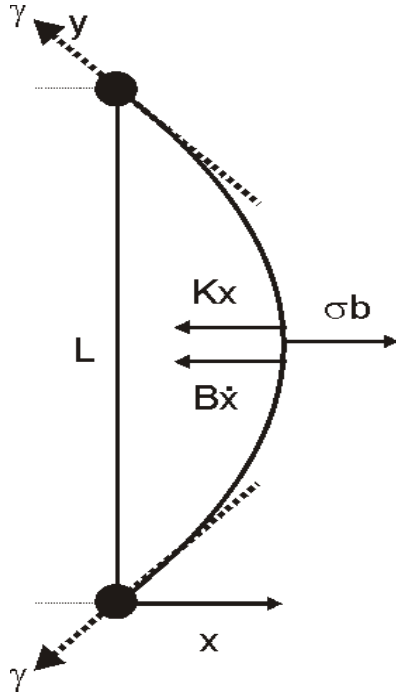

Figure 2.7: String model. A pinned dislocation segment of length L bowed under the applied stress. Two forces are acting against σb, the restoring force Kx due to line tension and dragging force $B\dot{x}$ (here expressed by unit of dislocation length) [113, 121].

Under an external applied stress σ, a dislocation loop of length L experiences a force $\sigma b L$ where b is the Burger's vector. Two main forces act in opposition to this applied force (Figure 2.7):

• The restoring force: KxL due to the dislocation line tension, $\gamma = KL^2/12$, where K is the restoring constant and x is the dislocation mean displacement.

• The dragging force: $B\dot{x}L$ due to viscous friction, caused by the interaction of dislocations with the lattice, point defect dragging, or other impurities. The dragging coefficient B depends on the mechanism which controls the dislocation motion (such as kink pair formation, dragging) and $\dot{x}$ is the dislocation velocity.

The equation of motion (expressed per unit dislocation length L and with negligible inertia) is given by:

$$\sigma b = Kx + B\dot{x} \qquad (2.15)$$

The total strain is:

$$\varepsilon = J_u \sigma + \Lambda bx \qquad (2.16)$$

where J_u is the unrelaxed compliance and Λ is the density of mobile dislocations. The relaxation strength Δ and the relaxation time τ can be calculated from equations (2.15) and (2.16) and by taking into account that $K = 12\gamma/L^2$ with $\gamma = b^2/2J_u$:

$$\Delta = \frac{\Lambda b^2}{J_u K} = \frac{\Lambda L^2}{6} \qquad \tau = \frac{B}{K} = \frac{BL^2}{12\gamma}$$

The mechanical-loss spectrum should present a relaxation peak of which height is proportional to the dislocation density and dislocation loop length. For instance, irradiation increases the point defect concentration creating additional pinning points with reduction of the free dislocation segment length. As a consequence, the peak height decreases.

Damping due to GB-dislocations (Lakki's model)

A model has been developed by Lakki et al. [83, 118] to describe the high-temperature mechanical loss behavior of alumina, where the grains are not wetted with any amorphous phase [122], and consequently high-temperature plasticity may be interpreted by the motion of GB-dislocations. The model is based on the dislocation string model described here above, where a pinned dislocation is able to vibrate around its position under an alternative applied stress (Figure 2.8).
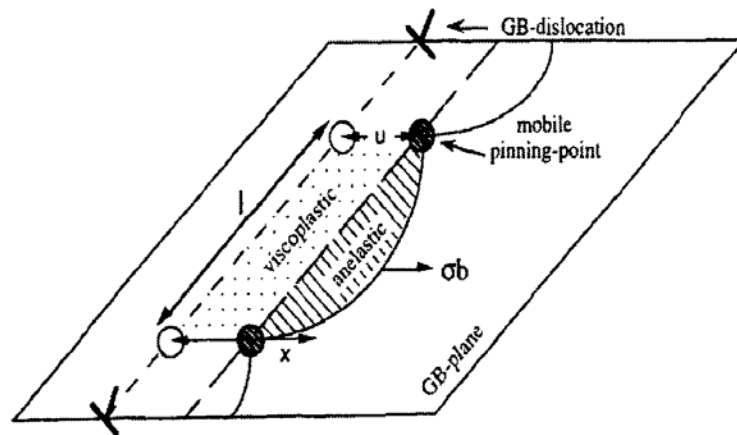

Figure 2.8: Modified dislocation string model where the pinning points are dragged by the GB-dislocation loop (after Lakki [83, 118]).

The equation of motion of a dislocation loop, which drags the pinning points may be written as [118]:

$$\sigma b = B_1 \dot{x} + K(x - u) \qquad B_2 \dot{u} = K(x - u) \qquad (2.17)$$

where σb is the applied stress (Peach-Koehler force per unit dislocation length), B_1 the viscous-friction coefficient accounting for the anelastic deformation, $K(x - u)$ the modified restoring force due to the fact that the pinning points can move over a distance u. B_2 accounts for the mobility of the pinning points. The motion of a dislocation segment is responsible for two types of strain:

- Anelastic strain represented by the hatched area in Figure 2.8.
- Viscoplastic strain represented by the dotted area in Figure 2.8.

Therefore, the total strain will be:

$$\varepsilon = \varepsilon_{el} + \varepsilon_{disl} = \frac{\sigma}{G} + \Lambda b x \qquad (2.18)$$

where Λ denotes the dislocation density (total dislocation length per unit volume). For GB-dislocations Λ should be expressed in terms of surface density (total dislocation length per unit GB-area). Taking into account the equations (2.17) and equation (2.18) the mechanical loss can be expressed by:

$$tan(\phi) = \frac{\frac{\Lambda b^2}{B_2}\left(1+\frac{B_1}{B_2}\right)+\frac{\Lambda b^2 B_2}{K^2}\omega^2}{\omega\left[\frac{1}{G}\left(1+\frac{B_1}{B_2}\right)^2+\frac{\Lambda b^2}{K}+\frac{B_1^2}{GK^2}\omega^2\right]} \qquad (2.19)$$

In a $log(tan(\Phi))$ vs. $log(\omega)$ plot the spectrum appears like a transition between two linear parts:

- Low-frequency region $(\omega \to 0)$:

$$tan\,(\phi) \to \Lambda b^2 \frac{1}{\omega\frac{B_1+B_2}{G}} \qquad (2.20)$$

- High-frequency region $(\omega \to \infty)$:

$$tan\,(\phi) \to \Lambda b^2 \frac{1}{\omega\frac{B_1}{G}} \qquad (2.21)$$

The mechanical-loss spectrum contains a relation peak, which turns into an exponential background for lower frequency.

2.3.3 Grain-boundary relaxation

Grain-boundary sliding according to Zener's model

Anelastic relaxation due to GB sliding with elastic accommodation for polycrystals has been first predicted by Zener [123] and investigated by Kê [124, 125]. Figure 2.9 illustrates a GB between two adjacent grains separated by a viscous interface, which cannot sustain the stress. When a shear stress σ is applied the grains deform elastically and then they slide over each other (for example, the grain 1 slides over the grain 2) to relieve the stress across the boundary, while building up opposing stresses (between the grains 3 and 4) at the triple junctions, due to elastic deformation of the neighboring grains. The sliding continues until the shear stresses are completely relaxed. This behavior corresponds well to that of the standard anelastic solid (2.3).
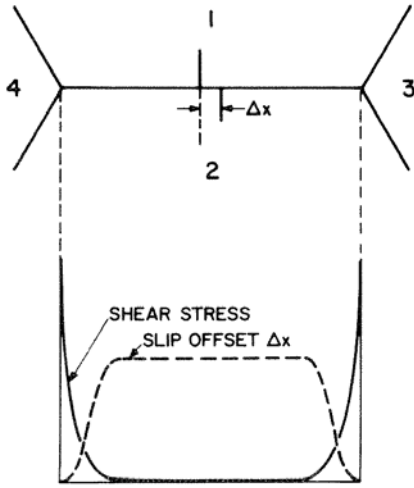

Figure 2.9: GB sliding relaxation with elastic restoration at the triple points (after Nowick and Berry [113]).

The corresponding relaxation equation for Δx is:

$$\frac{d[\Delta x(t)]}{dt} = -\frac{\Delta x(t) - \Delta x(\infty)}{\tau} \qquad (2.22)$$

where $\Delta x(t)$ and $\Delta x(\infty)$ are the GB slip deformation at time t, after equilibrium $t = \infty$, and τ is the relaxation time. The relaxation time predicted by such a model is given by [113]:

$$\tau = \frac{\eta}{\delta}\frac{d}{G_u} \qquad (2.23)$$

where η the is the viscosity and δ the thickness of the interface viscosity, d the grain size and G_u the unrelaxed shear modulus. Relaxed shear modulus $G_r = 0.4 G_u (7 + 5\nu)/(7 - 4\nu)$, where ν is Poisson's ratio. If $\nu = 0.3$, then $G_r/G_u = 0.6$. This model has been verified by different experiments [113].

Grain-boundary sliding according to Lakki's model

The theoretical model developed by Lakki [15, 83] accounts for relative sliding of equiaxed grains separated by a viscous layer of viscosity η and thickness δ (Figure 2.10) and constrained at the triple junctions.
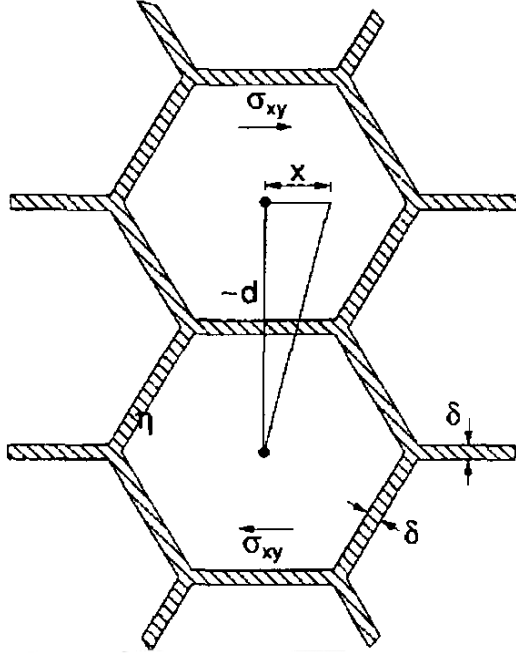

Figure 2.10: Simple schema representing the model of hexagonal grains separated by a viscous layer of viscosity η and thickness δ, which slide relative to each other with distance x under the effect of applied stress σ_{xy} (after Lakki [83]).

If x is the relative displacement of two grains, σ_{xy} the applied shear stress, and Kx the restoring force due to the limiting grains at triple junctions, the equation of motion is:

$$\sigma_{xy} = \frac{\eta}{\delta}\dot{x} + Kx \qquad (2.24)$$

The mechanical loss, $tan(\Phi)$ is obtained directly from the phase lag between stress σ_{xy} and strain ε:

$$\varepsilon = \frac{\sigma_{xy}}{G} + \frac{x}{d} = \varepsilon_0 cos(\omega\tau - \Phi) \qquad (2.25)$$

and the mechanical loss:

$$tan(\Phi) = \frac{G}{d}\frac{\omega\frac{\eta}{\delta}}{\left(\frac{KG}{d}+K^2\right)+\left(\omega\frac{\eta}{\delta}\right)^2} \qquad (2.26)$$

where G is the shear modulus and d the grain size.

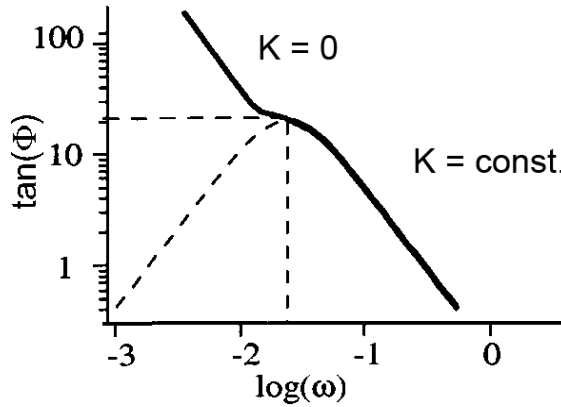If the restoring force is constant, $tan(\Phi)$ has the form of a peak (dotted line in Figure 2.11).

Figure 2.11: The peak position ω_p and the peak height $tan(\Phi)_{\omega=\omega_p}$ depend on grain size, viscosity and restoring force (cf. equation (2.26)).

The peak position ω_p and its maximum $tan(\Phi)_{\omega=\omega_p}$ are given by:

$$\omega_p = \frac{\delta}{\eta}\sqrt{\frac{KG}{d} + K^2} \tag{2.27}$$

$$tan(\Phi)_{|\omega=\omega_p} = \frac{G}{2d\sqrt{K^2 + \frac{KG}{d}}} \tag{2.28}$$

If the restoring force does not operate (K is zero in equation (2.24)), an exponential monotonic increase in damping with temperature is observed. Then, the mechanical loss background is given by:

$$tan(\Phi) = \frac{1}{\omega}\frac{G}{d}\frac{\delta}{\eta} \tag{2.29}$$

However, in most of the cases the restoring coefficient K is not zero, but decreases as a function of temperature (weakening of the pinning centers). Assuming that the restoring force is proportional to the shear modulus $G(t) = \tau/\varepsilon(t)$, which decreases strongly at high temperature, we get for K:

$$K(\omega) = \text{coeff}\frac{\sigma}{\varepsilon_{el}+\varepsilon_{pl}(t)} \approx c_1 \frac{\sigma}{\frac{\sigma}{G}+A\frac{\sigma^2}{2d}\exp\left(-\frac{E_a}{kT}\right)\frac{1}{\omega}} \tag{2.30}$$

Introducing equation 2.30 into equation 2.26, one obtains the theoretical spec-

trum of Figure 2.11, where the relaxation peak evolves into an exponential background at low frequency. This corresponds to most of the high-temperature mechanical-loss spectra observed in ceramics. Lakki et al. [15, 83] has interpreted the transition from the peak to the exponential background as the onset of creep in the material.

Grain-boundary relaxation according to Daraktchiev's model

Daraktchiev [126-128] suggested that the microstructure of zirconia is composed of two populations of grains with different amounts of intergranular-glassy phases giving rise to two peaks in the mechanical-loss spectra. Figure 2.12 shows a model of GBs, where the sample is composed of two regions of grains:

- The first region - small hexagonal grains with volume fraction f_1 and grain d_1 separated by an amorphous layer of viscosity η_1 and thickness δ_1.
- The second region - larger hexagonal grains with volume fraction f_2 and grain d_2 separated by an amorphous layer of viscosity η_2 and thickness δ_2.
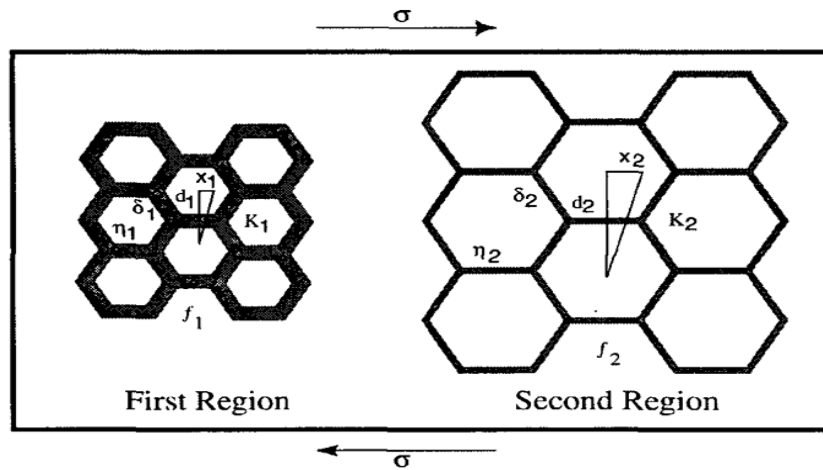

Figure 2.12: Two different regions of grains separated by an amorphous-intergranular phase. The volume fraction f of grains, viscosity η and the thickness δ are different in both regions of grains.

The mechanical loss is the sum of the contribution from the first and second region and can be expressed as:

$$tan(\Phi) = f_1 \frac{G}{d_1} \frac{\omega \frac{\eta_1}{\delta_1}}{K_1^2 + \frac{K_1 G}{d_1} + \omega^2 \frac{\eta_1^2}{\delta_1^2}} + f_2 \frac{G}{d_2} \frac{\omega \frac{\eta_2}{\delta_2}}{K_2^2 + \frac{K_2 G}{d_2} + \omega^2 \frac{\eta_2^2}{\delta_2^2}} \qquad (2.31)$$

where G is the shear modulus, K_1 and K_2 the restoring coefficients. When

K_1 and K_2 are strong and constants the equation (2.31) predicts two peaks of respective heights:

$$\frac{\Delta_i}{2} = f_i \frac{G}{d_1} \sqrt{\frac{1}{K_i^2 + \frac{f_i K_i G}{d_i}}} \tag{2.32}$$

When K_1 and K_2 vanish the mechanical loss becomes:

$$tan(\Phi) = f_1 \frac{G}{d_1} \frac{1}{\omega \frac{\eta_1}{\delta_1}} + f_2 \frac{G}{d_2} \frac{1}{\omega \frac{\eta_2}{\delta_2}} \tag{2.33}$$

In a real material, the restoring constants does not completely vanish, but decreases sharply at high temperature and the grains perform long range displacements: onset of creep. In fact, the grain motion is associated with local regions of several grains, where the accommodation processes control the micro-plastic deformation [129].

Assuming that K_1 and K_2 depend on the rigidity of the material through $\sigma/\dot{\varepsilon}$ we get:

$$K_i(\omega) = \frac{c_i \sigma}{\varepsilon_e + \varepsilon_{p,i}(t)} = \frac{c_i \sigma}{\frac{\sigma}{G} + \frac{1}{d_1} \frac{A\sigma^2}{4\omega} e^{\left(\frac{\Delta H_{act,i}}{RT}\right)}} \tag{2.34}$$

where i=1, 2, $\Delta H_{act,1}$ and $\Delta H_{act,2}$ are the activation enthalpies for the small and large grains, respectively, c_1 and c_2 are arbitrary constants, R the gas constant and T the absolute temperature.

2.4 Mechanical spectroscopy at high temperature

2.4.1 Creep and exponential background

The exponential increase in the mechanical loss and the decrease in the shear modulus at high temperature account for the appearance of ductility in ceramics, i.e. a kind of "brittle-to-ductile" transition. In fact, an exponential increase in $tan(\Phi)$ means an increase in the anelastic strain, which does not reach the equilibrium value: onset of the creep. Creep is described by a power law equation (see equation 1.1):

$$\dot{\varepsilon}(\sigma, T) = A \frac{\sigma^n}{d^p} exp\left(-\frac{\Delta H_{act}}{RT}\right) \qquad (2.35)$$

where A is a material constant, σ the applied stress, n the stress exponent, d the grain size, p the grain size parameter, ΔH_{act} the activation enthalpy, R and T have the usual meaning. Taking equations (2.11 to 2.13) and (2.35) into account we get for the mechanical loss:

$$tan(\Phi) = A' \frac{G\sigma^{n-1}}{\omega d^p} exp\left(-\frac{\Delta H_{act}}{RT}\right) \qquad (2.36)$$

were A' is a material constant, G the shear modulus and ω the circular frequency. Equation (2.36) has an exponential form, which reflects well the experimental results obtained in the high-temperature domain where creep is enhanced.

In real materials, because there is a certain distribution in the activation parameters, Schoeck et al. [130] proposed the following equation for the exponential background:

$$tan(\Phi) = \frac{C}{\omega^\alpha} exp\left(-\alpha \frac{\Delta H_{act}}{RT}\right) \qquad (2.37)$$

with $1/\alpha$ the broadening factor and C a material constant. The parameter α can be derived from the slope of $tan(\Phi)$ vs. $log(\omega)$ spectrum.

2.4.2 Activation parameters associated with the exponential background

Peak marker method

One way to estimate the activation enthalpy ΔH_{act} and the limit relaxation time τ_o is through an Arrhenius diagram. Reporting the logarithm of the peak frequency (without background) as a function of the inverse of peak temperature produces a straight line, the slope of which yields ΔH_{act}, and τ_o is obtained from the intersection of the line with the y-axis. In fact, background subtraction is not allowed when the same mechanisms are responsible for the entire mechanical spectrum (peak superposed on an exponential increase) as is the case of zirconia and alumina ceramics.

Master-curve methods

The estimation of the activation parameters can be done by a superposition of the mechanical-loss spectra to obtain a master-curve spectrum. This method is valid if the microstructure of the sample does not change during the measurement. Lakki et al [83, 118] proposed a procedure for determination of ΔH_{act} and τ_o from the temperature-frequency shift of the mechanical-loss spectra. The isothermal spectra corresponding to two different temperatures T_1 and T_2 are superposed by a shift along the frequency-axis. Reporting the frequency-shift as a function of the inverse of temperature $(\Delta(1/T) = 1/T_1 - 1/T_2)$, we get an Arrhenius plot, the slope of which gives ΔH_{act}. This procedure is valid if $tan(\Phi)$ is a function of $\omega\tau$ only, and τ_o is given by an Arrhenius law with constant activation parameters.

$$tan(\Phi) = tan(\phi[log(\omega\tau)]) = tan\left(\Phi\left[log(\omega) + \frac{\Delta H_{act}}{R \cdot ln(10)}\frac{1}{T} + log(\tau_0)\right]\right) \quad (2.38)$$

By bringing into coincidence the isothermal spectra corresponding to two different temperatures by a shift along the frequency-axis, which means a constant $tan(\Phi)$, the expression in the square brackets does not vary. Therefore, we get:

$$\Delta(log(\omega)) = -\frac{\Delta H_{act}}{R \cdot ln(10)}\Delta\left(\frac{1}{T}\right) - \Delta(log(\tau_0)) \quad (2.39)$$

Knowing ΔH_{act}, the limit attempt frequency ν_o can be determined by any point on the spectrum. From the superposition of all spectra together, the so-called "master-curve" spectrum is obtained. This spectrum together with the activation enthalpy contains the same information as all the spectra together.

Daraktchiev et al. [126, 131, 132] proposed another method to determine the activation parameters from isothermal-mechanical loss spectra in analogy with Dorn's algorithm largely used in creep measurements [133].

Creep strain measured at different temperatures and constant stress is given by:

$$\varepsilon = \varepsilon \left[t \cdot exp \left(-\frac{\Delta H_{act}}{RT} \right) \right] = \varepsilon(\theta) \tag{2.40}$$

where $\theta = t \cdot exp(-\Delta H_{act}/RT)$ is called temperature-compensated time. Similar to this assumption, a temperature-compensated frequency Ω may be defined for isothermal mechanical spectroscopy measurements:

$$\Omega = \omega \cdot exp \left(-\frac{\Delta H_{act}}{RT} \right) \tag{2.41}$$

Superposing two different isothermal spectra obtained at different temperatures by a shift along temperature-compensated frequency axis we get:

$$\omega_1 \cdot exp \left(-\frac{\Delta H_{act}}{RT_1} \right) = \omega_2 \cdot exp \left(-\frac{\Delta H_{act}}{RT_2} \right) \tag{2.42}$$

with ω_1, ω_2, T_1 and T_2 the frequencies and temperatures corresponding to the same $tan(\Phi)$. Therefore, the activation enthalpy can be obtained from the shift of isothermal spectra along the temperature-compensated frequency axis until a master curve is obtained. The position of the peak on temperature-compensated frequency axis gives the value of the limit attempt frequency.

2.4.3 Relevant results from literature

Polycrystalline zirconia - Y-TZP grades

Figure 2.13a shows typical mechanical loss and shear modulus spectra plotted as a function of temperature for two grades of zirconia: TS2/1, which contains a higher content of impurities and TS2/2. The TS2/1 shows a faster increase in the mechanical loss and a steeper decrease in the shear modulus with respect to TS2/2. During creep test at 1623 K, TS2/1 demonstrates in the low stress regime (10 MPa) a higher strain rate then TS2/2 (Figure 2.13b).

(a)	(b)
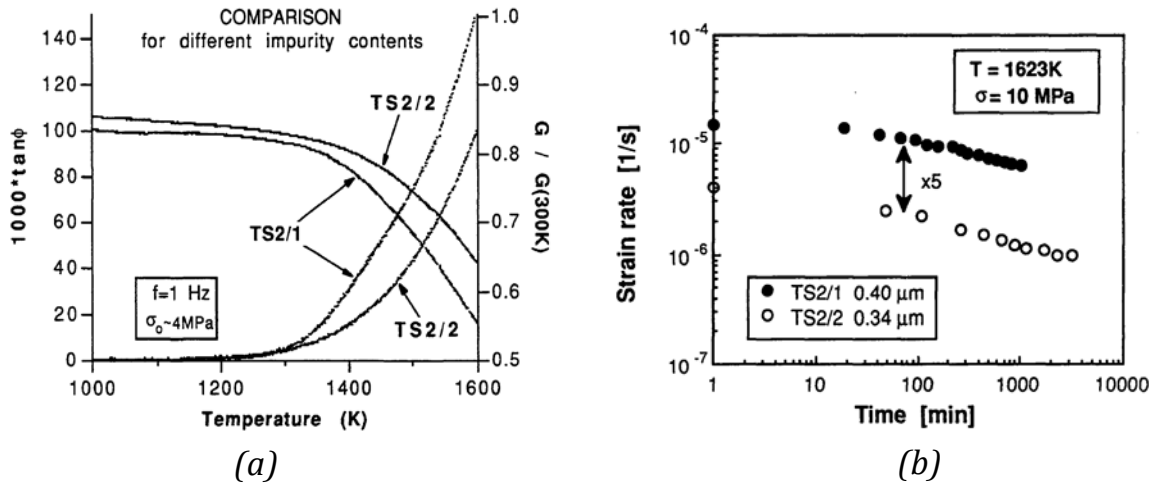
Figure 2.13: (a) Mechanical loss and shear modulus as a function of temperature for two zirconia samples TS2/1 (high content of impurity) and TS2/2. (b) Creep rate measured at 1623 K as a function of time (after Lakki [15, 83]).

In Figure 2.14a the mechanical-loss spectra of a single crystal is compared with the one of a polycrystalline sample.

(a)	(b)
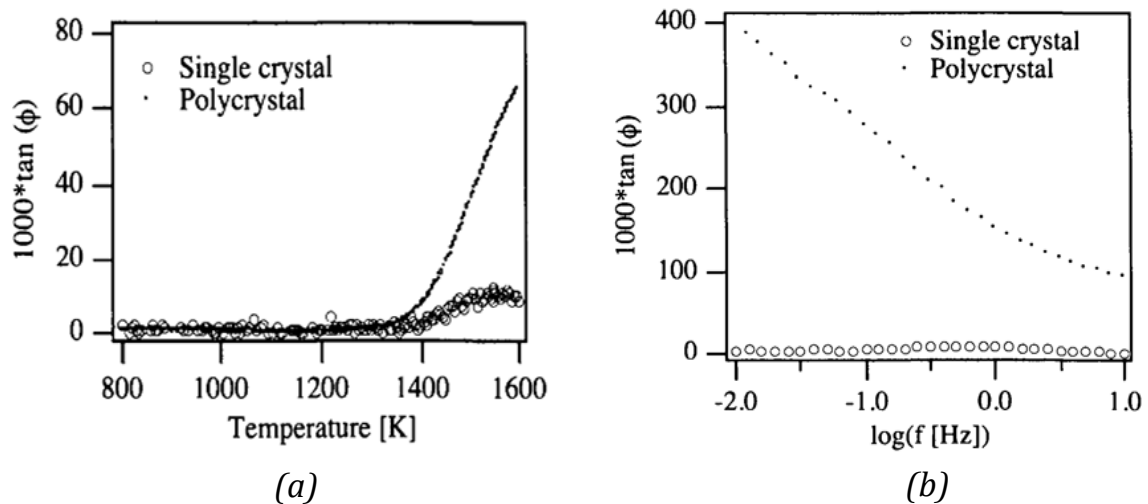
Figure 2.14: Mechanical losses as a function of a) temperature at 1 Hz and b) frequency at 1600 K are compared for a polycrystalline and single crystal zirconia (after Donzel [134]).

The damping in polycrystalline is much higher than in the single crystal. It is even more evident in the isothermal spectra (Figure 2.14b). As a consequence, the high-temperature damping is due to GBs, and it has been explained by a GB sliding model (§2.3.3), which was proposed by Lakki [15, 83]. The mechanical-loss spectrum of the single crystal exhibits just a dissipation peak. Donzel interpreted this peak as being due to the stress-induced reorientation of elastic dipoles (§2.3.1).

Figure 2.15a shows the influence of the grain size d on the mechanical-loss spectrum as a function of temperature. It can be seen that the mechanical loss increases exponentially with temperature and the higher the grain size the smaller the level of damping.
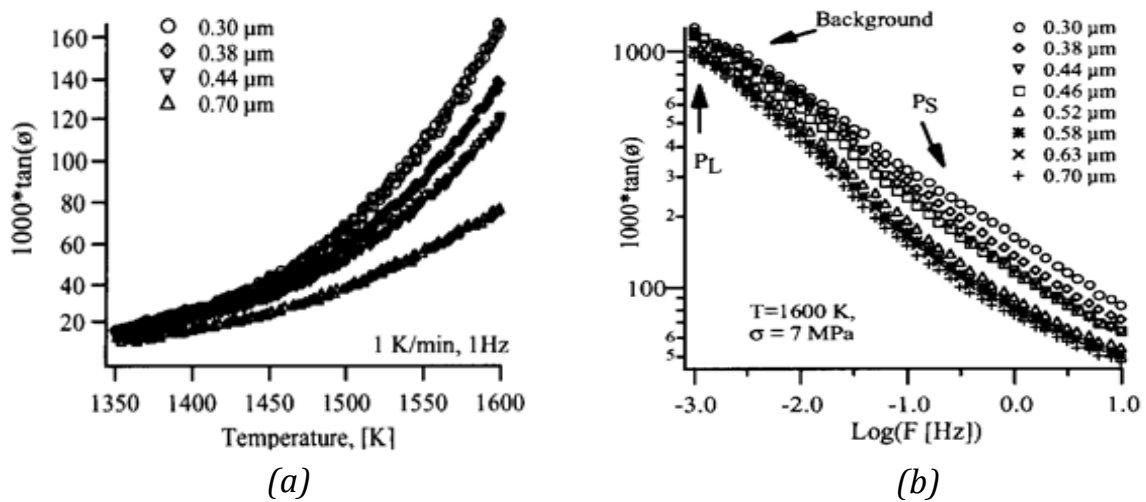
Figure 2.15: Mechanical loss plotted as a function of (a) temperature and (b) frequency for eight different grain sizes 0.30 µm - 0.70 µm (after Daraktchiev [126, 128]).

For the samples with a grain size $d < 0.7$ µm the mechanical-loss spectrum, obtained as a function of frequency (Figure 2.15b), is composed of a not well resolved peak (P$_S$) and an exponential increase at lower frequencies. This peak (P$_S$) has been observed in isothermal measurements made in 2Y-TZP grade [83, 134]). A new peak P$_L$ arises in the mechanical-loss spectrum at much lower frequencies. The existence of two peaks can be considered as a manifestation of two types of grains: small and large ones. The model described in §2.3.3 explains well this high-temperature behavior of polycrystalline zirconia (3Y-TZP grade). The peak height depends on $1/d$, while the background depends on $1/\sqrt{d}$ [126, 134].

The mechanical-loss spectra plotted as a function of frequency consists of a relaxation peak and an exponential background, which is represented by straight lines in Figure 2.16a. By using Daraktchiev's algorithm described in Figure 2.16b a value of 560 kJ/mol was obtained for the activation enthalpy. From the

peak position, the limit attempt frequency was found to be $\sim 10^{+19}$ s^{-1}.

All the above results concerning the high-temperature mechanical loss spectrum of zirconia were found to be in close relation with the creep behavior. Similar values have been obtained for the activation enthalpy and the grain size exponent.
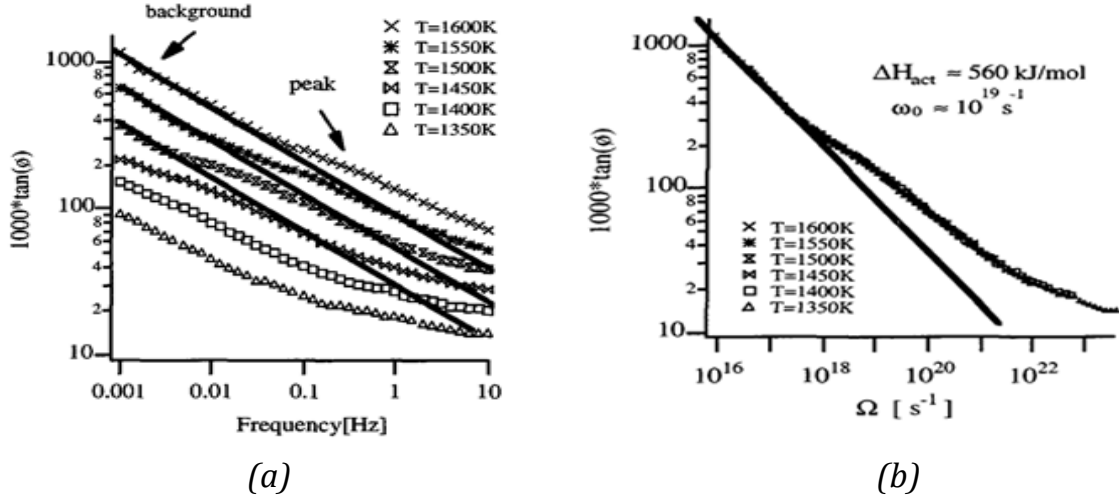

(a) *(b)*

Figure 2.16 (a) Mechanical loss plotted as a function of frequency (d = 0.30 μm). (b) The master-curve spectrum results from the shift of the isothermal spectra along the temperature-compensated frequency (after Daraktchiev [83, 126].

For instance, it was observed for stresses higher than 2 MPa that the mechanical loss increases linearly with the stress in the low frequency ($\sim$10 mHz) and high temperature (1600 K) regimes. This is in good agreement with equation (2.37) and the value of the stress exponent $n \sim 2.4$ obtained in creep tests when the stress is lower than 15 MPa [82].

Polycrystalline alumina

Typical high-temperature mechanical loss spectra of alumina are shown for three different grain sizes of MgO-doped alumina as a function of temperature (Figure 2.17a) and of frequency (Figure 2.17b).

Figure 2.17a shows that the mechanical loss increases monotonically with temperature. For small grain sizes the mechanical loss is roughly independent, while for larger ones, it decreases with $\sim 1/d$. Figure 2.17b shows that the isothermal-mechanical loss decreases when the grain size increases.

The high-temperature mechanical behavior in alumina has been interpreted by a GB-dislocation model proposed by Lakki [83, 118] and described in §2.3.2.

A value of 840 kJ/mol was obtained for the activation enthalpy from the frequency-shift method. As in most cases, this value of the activation enthalpy is

too high. It is an apparent value, which must be corrected. This point is worth for a more careful study.
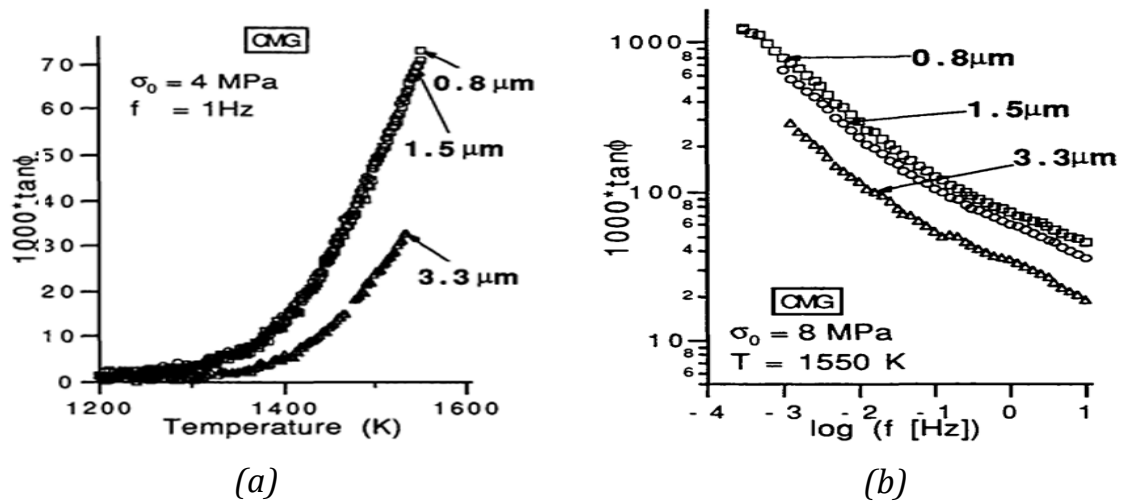

<center>(a)   (b)</center>

Figure 2.17: Mechanical loss plotted as a function of (a) temperature and (b) for three different grain sizes: 0.8 μm, 1.5 μm and 3.3 μm (after Lakki [83]).

Chapter 3

Materials and techniques

In this chapter, the material processing and microstructure characterizations are presented for polycrystalline zirconia: pure, impure and doped with multi-walled carbon nanotubes or silicon carbide whiskers or particles. Also, polycrystalline alumina: pure and doped with silicon carbide particles are presented. The experimental setup and the general principles are described here.

3.1   Polycrystalline zirconia

The materials used in this study are:
- two commercial 3 mol % yttria-stabilized zirconia polycrystals differing in the impurity content, called 3Y-TZP and 3Y-TZPE (supplied by Tosoh Corporation, Japan),
- multiwalled carbon nanotubes CNTs (prepared at IPMC, LNNME - chemistry laboratory, EPF Lausanne, by a CVD method [135, 136]),
- silicon carbide whiskers SiCw (SCW1-8 supplied by Tateho Chemicals Industry Co., Ltd., Japan) and
- β-silicon carbide nan-particles SiCp (supplied by MTI Corporation).

3.1.1   Powder morphology

Zirconia powders were tuned with binders to increase the mechanical pressing at ambient temperature. The nominal impurity content in wt. % in the starting batches of polycrystalline zirconia powders is reported in Table 3.1.

Impurity [wt. %] Powders	Y_2O_3	Al_2O_3	SiO_2	Fe_2O	Na_2O
3Y-TZP	< 5.350	0.005	0.006	0.002	0.021
3Y-TZP-E	5.260	0.254	0.005	0.004	0.023

Table 3.1: Impurity content in wt. % of polycrystalline zirconia grades.

The content of alumina is five times higher in 3Y-TZPE than in 3Y-TZP high purity.

The impurity content of the as-supplied SiCw and SiCp powders is given in Table 3.2.

Impurity [wt. %] Powders	O	C	Mg	Al	Ca	Fe* [ppm]
SiCw	-	-	0.15	0.10	0.15	130
SiCp	$1 \sim 1.5$	$1 \sim 2$	-	-	-	-

*Table 3.2: The impurity content of SiCw and SiCp. *HCl leaching.*

Transmission electron microscopy (TEM) was used to characterize the powders. The TEM sample preparation involved dispersion of the powders in iso-propyl alcohol by sonication (30 min) and a drop of suspension was placed on a copper grid covered with holey carbon. A Philips CM20 microscope operating at 200 kV was used for this study. In Figure 3.1a and Figure 3.1b are shown the TEM images of 3Y-TZP and 3Y-TZPE powders, respectively. Zirconia crystallites are agglomerated forming chains. The average particle size is 0.27 μm for 3Y-TZP and 0.28 μm for 3Y-TZPE.

(a)   *(b)*
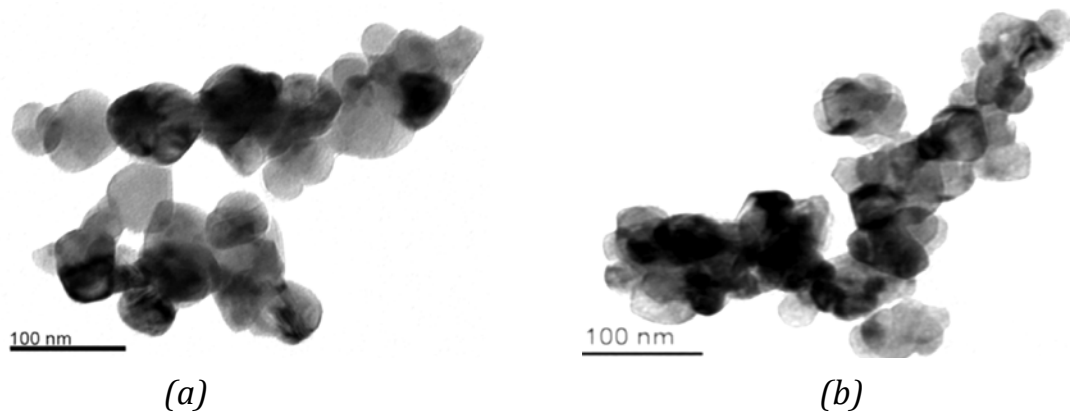
Figure 3.1: TEM images of the (a) 3Y-TZP and (b) 3Y-TZPE powders.

CNTs have a wavy form and differ in length and width from one another (Figure 3.2a). They are well separated, although at certain locations they seem to be bundled together. SiCw show large cross-section with undulating surfaces (Figure 3.2b). The length of whiskers ranges from 30 μm to 100 μm and the diameter from 0.8 μm to 1 μm. The TEM image (Figure 3.2c) of SiCp powder reveals nano-sized agglomerated particles. The particle size is about 30 nm. The particles seem to be surrounded by a silica layer with a thickness of about 1 nm (Figure 3.2c).

Carbon nanotubes are one of the strongest and stiffest materials known, in terms of tensile strength and elastic modulus, respectively. This strength results from the covalent sp^2 bonds formed between the individual carbon atoms. The strength can be lowered by 85 % in the presence of a high level of defects (i.e. vacancy) [137]. CNTs have very high elastic moduli, $E \sim 1$ TPa [138].

Usually the high value of E is taken as granted for all types of CNTs. The elastic modulus falls to 100 GPa due to the presence of the structural defects [139]. CNTs tend to undergo buckling when placed under compressive, torsional or bending stress [140].
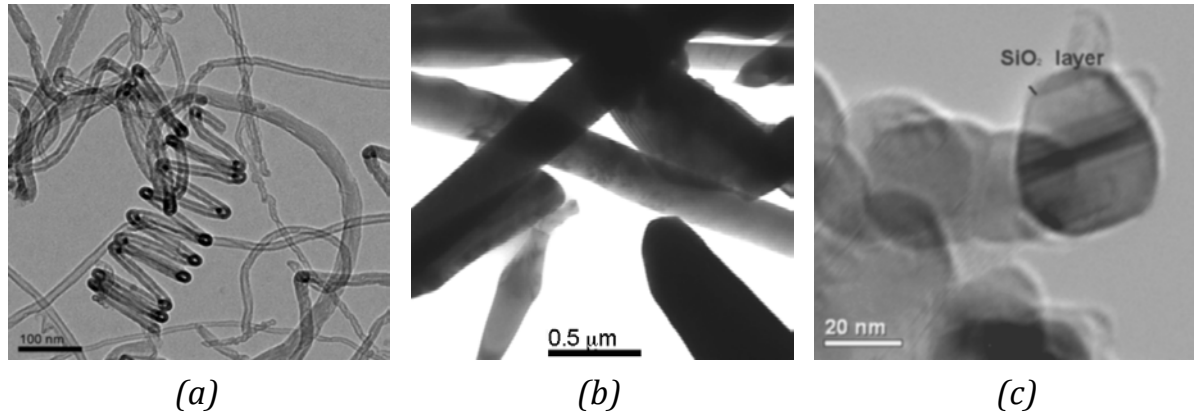

(a)   *(b)*   *(c)*

Figure 3.2: TEM images of (a) CNTs, (b) SiCw, (c) SiCp powders.

Whiskers with small diameters and without flaws or imperfections have very high strength and modulus values. For example, SiCw with a diameter between 0.1 – 0.6 μm have the Young's modulus between 400 - 700 GPa [141]. Addition of whiskers to alumina ceramics produces a significant increase in strength and suppress the grain growth in the matrix [142].

SiCp are composed of tetrahedra of carbon and silicon atoms with strong bonds in the crystal lattice. This produces a very hard and strong material (i.e. 410 GPa for the Young's modulus).

When CNTs or SiCw or SiCp are dispersed in ceramics (zirconia or alumina), the mechanical properties, such as elasticity, strength or hardness can be strongly improved [143-147].

3.1.2 Sample preparation

Dense samples were obtained by powder metallurgy. The polycrystalline zirconia powder was first mixed either with CNTs or SiCw or SiCp via attrition milling by using zirconia balls grinding media. The homogenized powders were passed through a sieve (150 μm). Pure, impure and doped zirconia powders were shaped in a floating matrix mould by cold uniaxial pressing (C.P.) at 100 MPa. The compact plates of dimensions (60 x 30 x 5) mm^3 were sintered in two stages in argon atmosphere. The heating stage consists in an increase of temperature by 10 K/min in two steps: up to 923 K and maintained for 4 h to burn out the chemical binder, followed by firing at temperatures between 1673 K - 1773 K during 3 h. The second one is cooling down to room temperature by 3 K/min. The cooling rate is a crucial parameter regarding the micro-

structure, especially in the repartition of the viscous phase at the GBs. The densities of the as-sintered samples were obtained by Archimedes's method in distilled water at room temperature. In Table 3.3 are presented the fabrication conditions and the relative densities ρ of the bulk samples.

Composition	Denotation	Mix [h]	C.P. [MPa]	T_{sint} [K]	ρ [%]
3Y-TZP	Z0	-	100	1673	99.4
		-	100	1723	99.5
		-	100	1773	99.6
3Y-TZPE	ZE	-	100	1673	99.6
3Y-TZP + 0.5 wt. % CNTs	Z0.5CNTs	12	100	1723	98.7
3Y-TZP + 1.5 wt. % CNTs	Z1.5CNTs	24	100	1773	96.7
3Y-TZP + 0.5 wt. % SiCw	Z0.5SiCw	12	100	1723	84.4
3Y-TZP + 1.5 wt. % SiCw	Z1.5SiCw	24	100	1773	80.3
3Y-TZP + 0.5 wt. % SiCp	Z0.5SiCp	12	100	1723	87.6
3Y-TZP + 1.5 wt. % SiCp	Z1.5SiCp	24	100	1773	85.4

Table 3.3: Fabrication conditions and relative densities of the as-sintered samples.

3.1.3 Microstructure

The microstructure studies were performed by high resolution scanning electron microscopy HRSEM (Philips XL30 FEG EBSP, CIME, EPFL), transmission electron microscopy TEM and high resolution transmission electron microscopy HRTEM (Philips CM20 and Philips CM300, CIME, EPFL equipped with EDS system.). The samples for HRSEM observations were mechanically polished (1 μm), thermally etched at 50 K less than the firing temperature for 30 min in Ar atmosphere and coated with a thin layer of carbon. TEM specimens were tripod polished down to 80 μm and then thinned by ion-milling (Ar+, 4 kV). Grain size and its distribution were analyzed from HRSEM micrograph by using an image analysis technique ("ImageJ", NIH).

A typical microstructure of polycrystalline zirconia sintered at 1673 K in Ar atmosphere is shown in Figure 3.3a. Zirconia exhibits a well-shaped microstructure of equiaxed grains. Neither cavities nor amorphous phase were observed in the as sintered zirconia. The grain size was obtained by considering that the grain diameter is the diameter of a circle. The obtained data were plot-

ted in a histogram (Figure 3.3b). From the maxima of frequency/weight in Figure 3.3b can be estimated the mean grain size $\bar{d}$. Thus, $\bar{d}$ = 0.30 μm for Z0 sintered at 1673 K in Ar atmosphere.
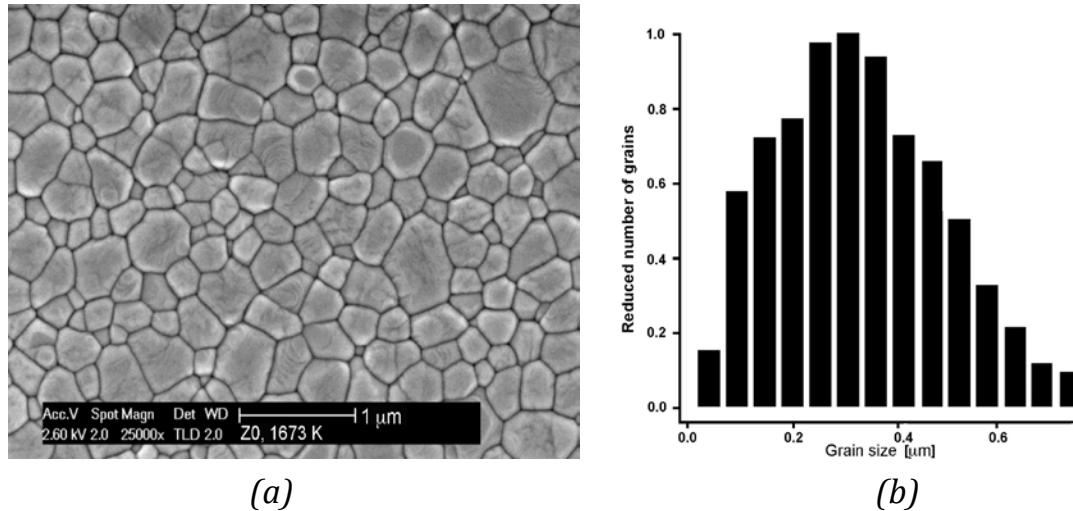

(a)   *(b)*

Figure 3.3 (a) HRSEM micrograph of a typical microstructure of Z0 sintered at 1673 K in Ar atmosphere. (b) Normalized grain size distribution. The mean grain size is 0.30 μm.

In order to achieve an increase in the grain size some zirconia samples were sintered at higher temperatures. The HRSEM image of Z0 sintered at 1723 K is shown in Figure 3.4a and for Z0 sintered at 1773 K in Figure 3.4b. The mean grains sizes were found for Z0 in Figure 3.4a and Figure 3.4b to be 0.50 μm and 0.70 μm, respectively.

(a)   *(b)*
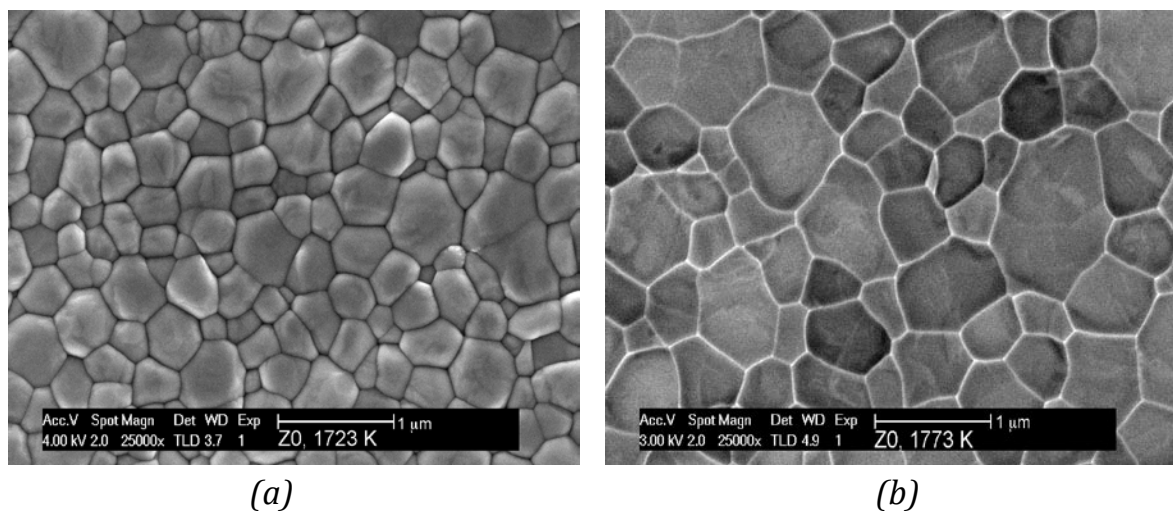
Figure 3.4: HRSEM images of Z0 sintered at: (a) 1723 K and (b) 1773 K in Ar atmosphere.

The HRSEM image of ZE sintered under the same conditions as pure zirconia is shown in Figure 3.5a. The mean grains size was found to be ~ 0.30 μm.

In Z1.5CNTs the grains seem to be sharper (Figure 3.5c) than in Z1.5SiCw (Figure 3.5c) and Z1.5SiCp (Figure 3.5d) were the grains are more rounded. Between zirconia grains (in grey) a second phase grains (dark spots) can be seen in Figure 3.5c and Figure 3.5d. On the surface of the second phase are present SiCp and small zirconia grains (Figure 3.5d). In all composites, the zirconia matrix exhibits equiaxed grains with $\bar{d} \sim 0.30$ µm.


(a)

(b)

(c)

(d)
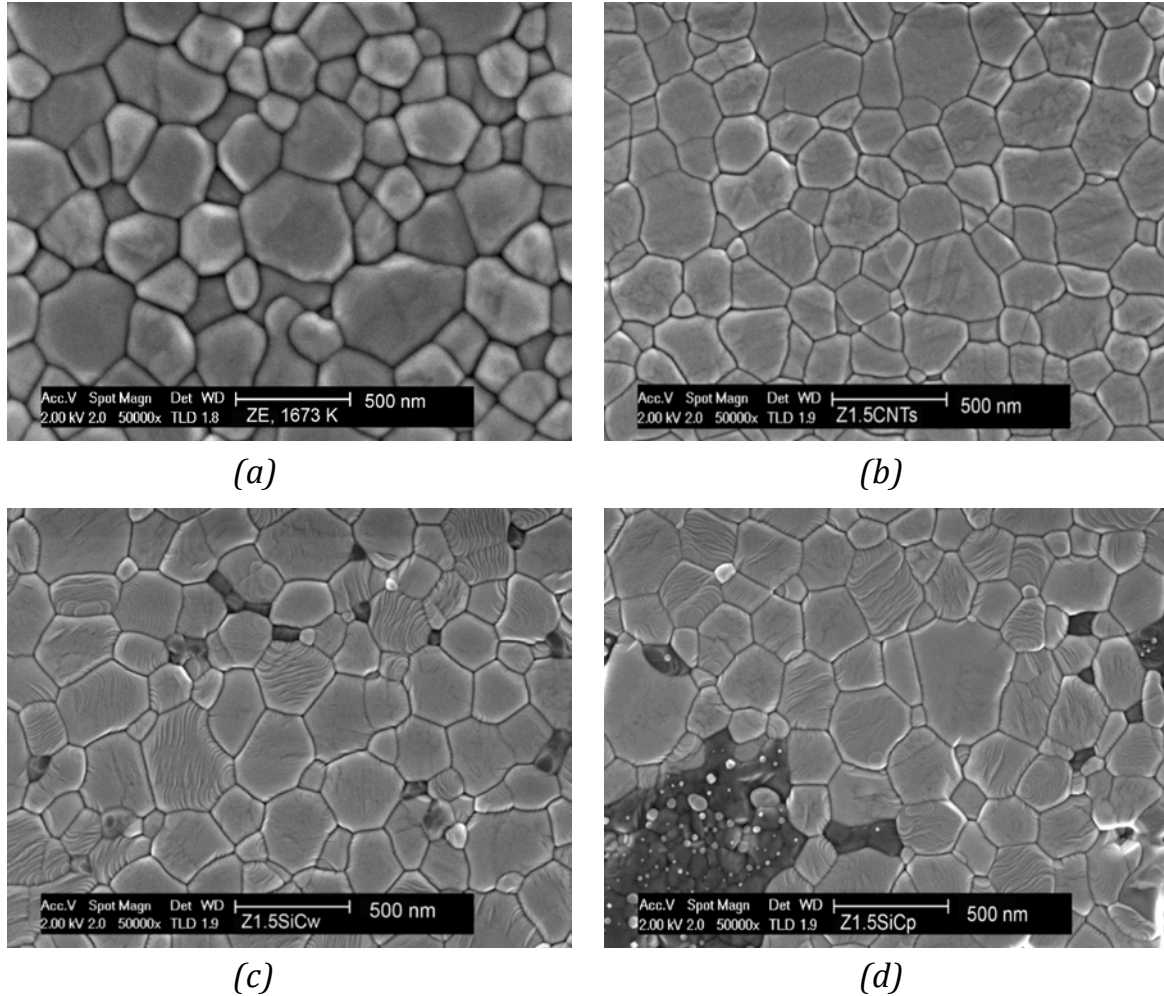
Figure 3.5: HRSEM micrographs of (a) ZE, (b) Z1.5CNTs, (c) Z1.5SiCw and (d) Z1.5SiCp.

HRTEM studies were performed on the microstructure of pure and impure zirconia. In pure zirconia the GBs were found to be both clean and wetted with an amorphous phase. Figure 3.6a shows an HRTEM image of a clean GB. The lattice fringes meet directly at the GBs. Neither intergranular precipitation nor dislocations are observable in Figure 3.6a. By using the bright field (BF) mode and Fresnel fringe method an amorphous film was detected between zirconia grains (Figure 3.6b). The thickness of the amorphous film is ~ 1 nm. The microstructure of impure zirconia presents clean GBs, wetted GBs and occasionally, small glassy pockets made of silicate glass at the multiple junctions.
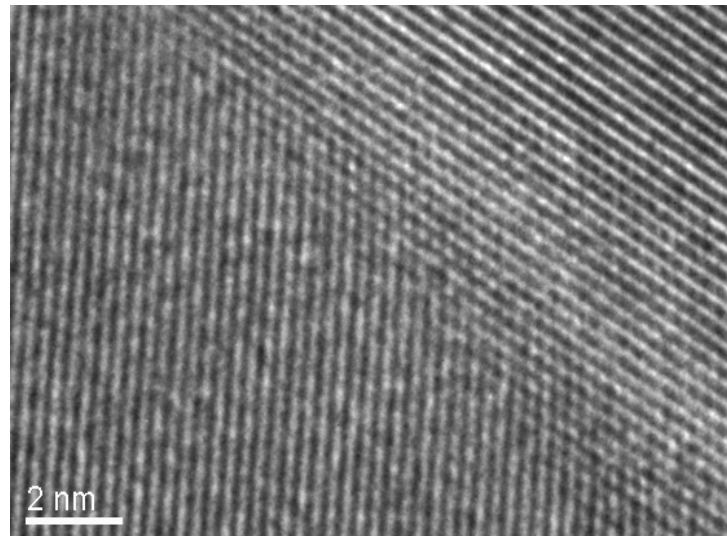
(a)
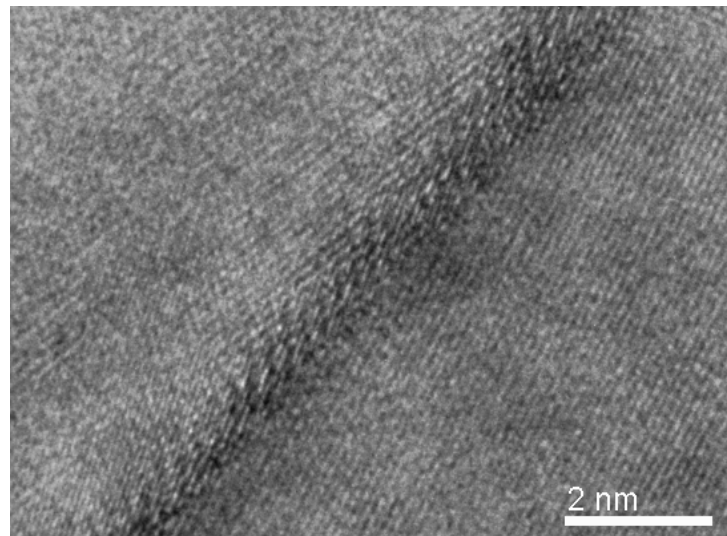
(b)

Figure 3.6: HRTEM images of pure zirconia (a) clean GBs and (b) two grains separated by an amorphous layer. The thickness of the layer is ~ 1 nm.

TEM observations in Z1.5CNTs sample reveal a microstructure similar to "traditional" zirconia (Figure 3.7). The high diffraction contrast along GBs is due to the large residual stresses, resulting from the incorporation of CNTs at the GBs.

The HRTEM image of such an area is shown in Figure 3.8a. Two zirconia grains (left and right in Figure 3.8a) are separated by a thick amorphous layer. The thickness of the layer, probably resulting from the original carbon, could reach 5 nm to 10 nm. This layer is not consistent with the intergranular-glassy phase thickness predicted or observed in polycrystalline zirconia (1 nm) [10, 11, 24]. In fact, the CNTs layer is strongly correlated to the cooling rate [26].
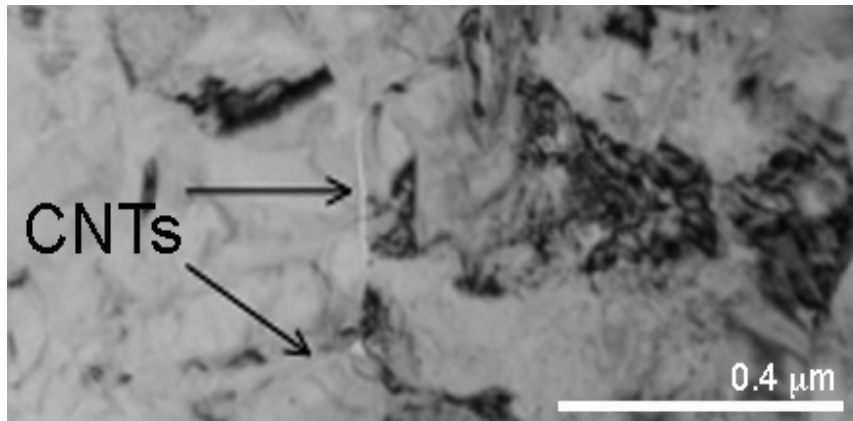
Figure 3.7: Bright field TEM image on a Z1.5CNTs. Arrows indicate a particular bright contrast along GBs (courtesy of B. Van de Moortèle).

Electronic energy loss spectroscopy (EELS) analysis of zirconia grains and CNTs layer are shown in Figure 3.8b. The amorphous area corresponds to amorphous carbon probably issued from the initial CNTs. In Figure 3.8b, the Zr_M_{45} and Zr_M_2 edges start at 180 eV and 344 eV, whereas O edge starts at 532 eV. The C edge starts at 280 eV indicating that the layer between zirconia grains corresponds to amorphous carbon.

(a) *(b)*
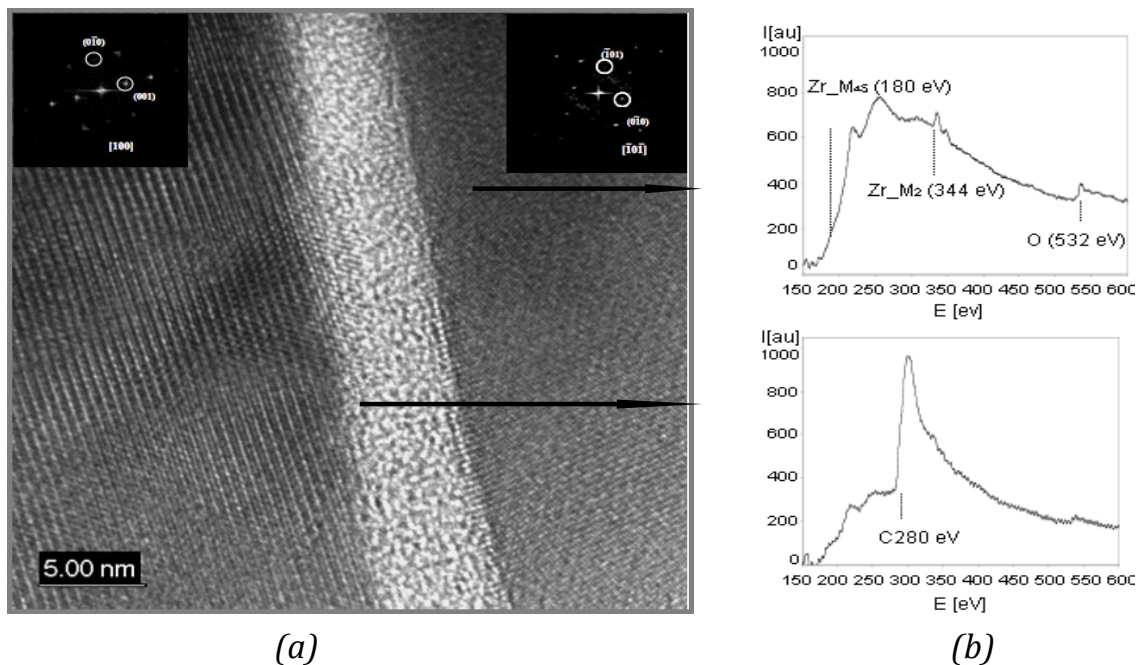
Figure 3.8: (a) HRTEM image (Fourier transform in insert) and (b) EELS analysis on GBs of Z1.5CNTs (courtesy of B. Van de Moortèle).

The TEM image of Z1.5SiCw is presented in Figure 3.9. Because of low volume fraction just a few of SiCw can be observed within or between zirconia grains (Figure 3.9). SiCw whiskers are oriented in various directions. At the triple junctions are present large pockets of amorphous phase (light grey regions).

EDS analysis performed inside the pockets reveals that they are composed of ZrO_2, Si, and O.
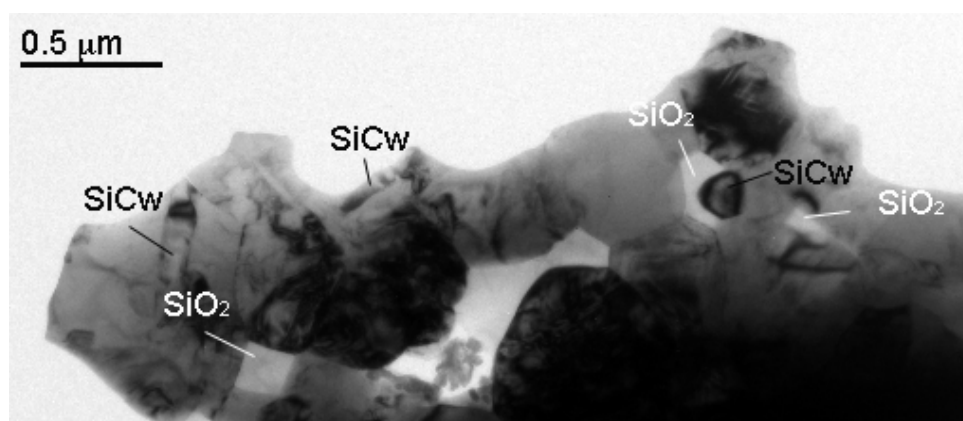

Figure 3.9: Bright field TEM micrograph showing the microstructure of Z1.5SiCw.

Figure 3.10 shows a TEM image of Z1.5SiCp. SiCp are mostly situated at the GBs. Pockets of glassy phase (light grey) associated with porosity are often observed at the triple junctions (Figure 3.10). EDS analysis was performed inside the pockets. It reveals a heterogeneous phase composed mainly of ZrO_2, Si and O.
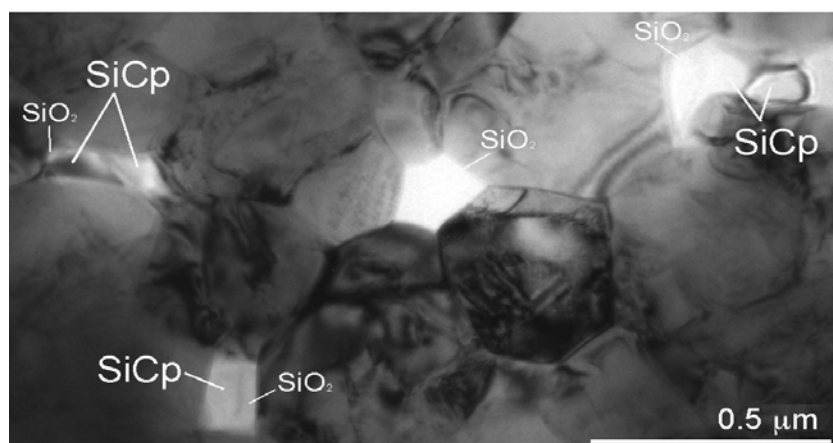

Figure 3.10: Bright field TEM image showing the microstructure of Z1.5SiCp.

3.2 Polycrystalline alumina

Alumina containing different amounts of ultrafine silicon carbide particles SiCp (0.5 vol. % or 5 vol. %) as well as undoped alumina were supplied by Dr. Sciti, CNR-IRTEC Faenza, Italy. The samples were prepared in the framework of an European project concerning the microstructure and mechanical properties of Al_2O_3/SiCp nano-composites. The characteristics of the powders, preparation of the sample and microstructure are presented below [147, 148].

3.2.1 Powder morphology

α-Al_2O_3 powder was provided by Baikalox (grade CR30F). β-silicon carbide particles (SiCp) were synthesized via a laser route by CEA-Saclay, Vitry Sour Seine, France. The main characteristics of the as received powders are reported in Table 3.4.

Sample	d_p [nm]	Purity (chemical analysis)	Chemical composition (TEM and EDS analysis)
α–Al_2O_3	60	99.9998	ppm K:22 Na:13 Si:16 Fe:3 Ca:2, Mg:<1
β-SiCp[o]	30	O:3.9, SiO_2:7.4 wt. %, S~0. 5 nm	at. % Si:48.3, C:48.4, O:3.3
β-SiCp[*]	30	O:4.7, SiO_2:8.9 wt. %, S~0.6 nm	at. % Si:50.3, C:43.6, O:5.9
β-SiCp[x]	30	O:6.2, SiO_2:11.6wt. %, S~0.7 nm	at. % Si:49.9, C:46.7, O:3.4

Table 3.4: Characteristics of the starting powders. The SiCp exponents (◦) is used for the as received powder, (∗) for thermally treated at 1573 K in Ar atmosphere for 12 h and (x) for the powder treated in aqueous environment at pH=6 for 12 h at room temperature. (d_p mean particle size, S surface area silica thickness).

In Figure 3.11 is shown the TEM image of a SiC powder. SiC particles are agglomerated forming long chains.
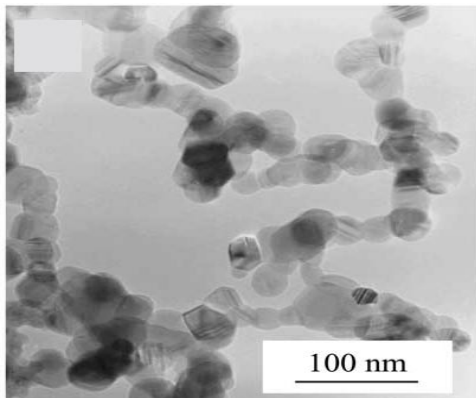

Figure 3.11: TEM micrograph of the SiCp from the as received powder. The average crystallite size is in the range of 200-300 nm (after Sciti [147]).

Chemical and TEM analyses were performed on SiCp powders to determine the amount of oxygen and the thickness of the silica layer. In order to evaluate the

surface reactivity of the particles during processing step, SiCp powder was treated in aqueous environment at pH = 6 for 12 h at room temperature. In addition, a powder sample of SiCp was thermal treated in a graphite furnace at 1573 K for 12 h in Ar atmosphere. After each treatment, the variation of the surface silica was evaluated through chemical analysis as reported in Table 3.4. In Figure 3.12a a SiC particle is shown in as received state. The silica layer has a thickness of ~1 nm on the surface. After the thermal treatment, at 1573 K for 12h in Ar atmosphere the thickness of silica layer has increased (Figure 3.12b). The thickness of silica layer has increased from 0.5 nm to 0.7 nm (Figure 3.12c). As well, there is an increase in the oxygen content and at the same time a loss in carbon.

(a)   *(b)*   *(c)*
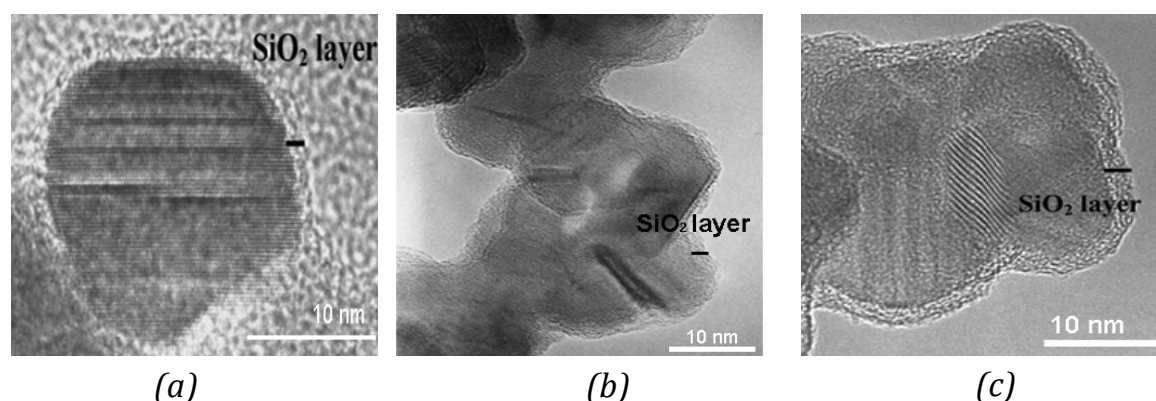
Figure 3.12: HRTEM images of the SiCp powders: (a) as received, (b) thermally treated for 12 h, at 1573 K, in Ar atmosphere and (c) treated in aqueous environment (pH=6) for 12 h at room temperature (after Sciti [147]).

After the treatment with water at room temperature for 12 h, the variation of the chemical composition of SiCp powder is revealed in the oxygen amount that is related to SiO_2 amount and the surface layer thickness Table 3.4. As a consequence, the mixture of the powders has to be done by water-free solvents to avoid the oxygen enrichment.

3.2.2   Sample preparation

Dense alumina doped with SiCp and pure alumina were obtained via hot pressing. The alumina and silicon carbide mixtures were prepared through separate dispersions of the starting powders in ethyl alcohol by ultrasonic pulses associated with magnetic stirring. The powders were further mixed and homogenized by ultrasonic pulses. Drying was performed in a rotary evaporator under an inert gas stream. The dried powders were passed through a plastic sieve (150 μm). Hot pressing was performed under vacuum (10^{-1} Pa) on the pure and SiCp-doped alumina powders at temperatures between 1723-1973 K for 10-25 minutes, under an applied pressure of 30 MPa. Sintering temperature was increased with increasing the amount of SiCp (Table 3.5). The density ρ of the as sintered materials was measured using the Archimedes method in distilled

water and the obtained values are listed in Table 3.5.

Sample	Composition	H.P. [K]	Time [min]	ρ [%]	$\overline{d}$ [μm]
A0	Al_2O_3	1723	25	100	~ 0.9
A05	Al_2O_3 + 0.5 vol.% SiC	1923	10	99	~ 0.6
A5	Al_2O_3 + 5 vol.% SiC	1973	20	100	0.3-0.4

Table 3.5: Characteristics of the hot-pressed samples.

3.2.3 Microstructure

The as-sintered samples were cut and polished to 1 micron for SEM observations. Thermal etching was carried out in a graphite furnace at 1623 K in Ar atmosphere to delineate the GBs. The SEM micrographs of as-sintered: A0, A05 and A5 samples are shown in Figure 3.13.
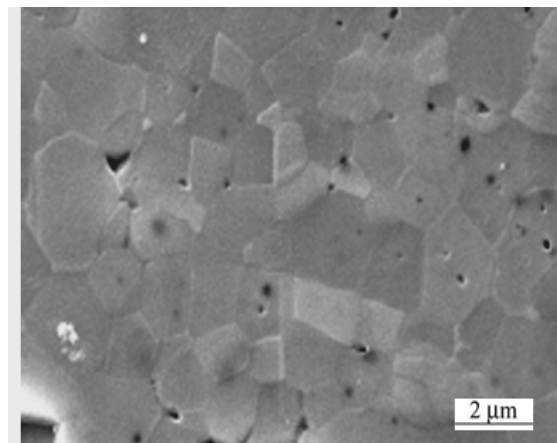
(a)
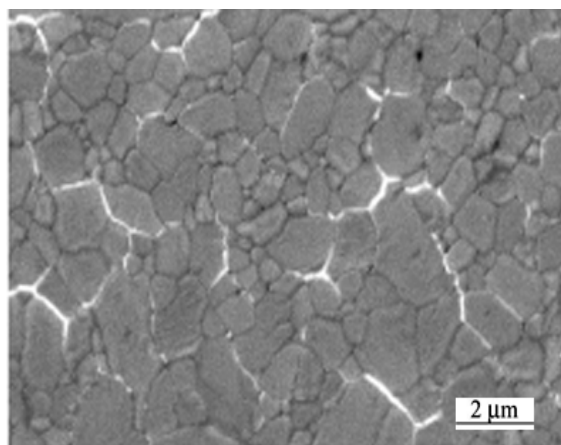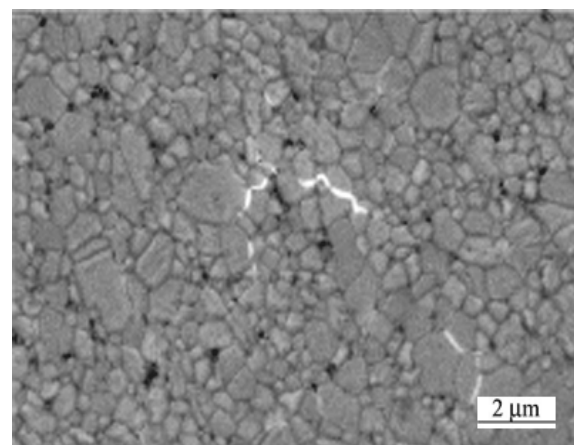
(b) *(c)*

Figure 3.13: SEM images of (a) A0, (b) A05 and (c) A5 sample after polishing and thermal etching. All samples exhibit an equiaxed microstructure. Microcracks are observed along GBs in both SiCp-doped Al_2O_3 (after Bellosi et al. [148])

All samples exhibit equiaxed grains. Some pores are present in the as sintered A0 and A5 (black dots in Figure 3.13a and Figure 3.13c). In SiCp/Al$_2$O$_3$ nano-composites, SiCp are predominantly located at the matrix GBs. Microcracks are observed along the GBs (Figure 3.13a and Figure 3.13b). SiCp that are linked together in the starting powder may form agglomerates in the final products. These clusters could be the origin of defects, like microcracks. The mean grain size $\bar{d}$ values were obtained by Hilliard's method: $\bar{d} = C/LM$, where C is the grain diameter, L the number of the GBs of C and M the magnification. The mean grain size values of the alumina matrix are given in the Table 3.5. The mean grain size values have the tendency to decrease with increasing SiCp vo-lume fraction, as reported by many authors [144, 149-153]. The grain size dis-tribution is not homogeneous due to the presence of SiCp.

Additional microstructural features were revealed by TEM and HRTEM analysis [147]. The samples were mechanically ground down to 80 μm in thickness, dimpled and thinned by ion-milling (Ar+, 6 kV). A Jeol 1020 microscope equipped with a Link analyzer EDS system was used for TEM. HRTEM was per-formed with a Topcon EM 002B (200 kV). TEM images revealed that the SiCp are mainly (>96 %) located along the GBs of the alumina matrix, while a small fraction of fine SiCp (20 nm) are entrapped within the bulk (Figure 3.14a). SiCp agglomerates often surround a pore that can be open or act as a sink for the accumulation of excess amorphous phase. Normally, SiCp grains are packed to-gether along the GBs forming polycrystals of about 500 nm. The mean grain size of SiCp is about 50 nm. Strain contrast is observed around intergranular SiCp in Figure 3.14b. SiC grains exhibit several stacking faults and seem to be embedded inside a glassy phase (Figure 3.14c). Large pockets of SiC grains as-sociated with porosity are often observed at the triple junctions (Figure 3.14c). EDS analysis was performed inside SiCp pockets. It reveals a heterogeneous phase composed mainly of Al, Si and O. Figure 3.14d shows a HRTEM image of SiCp/Al$_2$O$_3$ interface. The phase boundary is free from amorphous phase. The presence of an amorphous thin layer (2 nm) cannot be excluded even the liquid phase accumulates preferentially in large pockets and pores in the open space between SiCp agglomerates.

The mechanical properties of the undoped and SiCp-doped alumina nanocom-posites are given in Table 3.6 [147].

Sample	E [GPa]	Hardness [GPA]	K$_{IC}$ [MPa m$^{0.5}$]	Flexural strength [MPa]
A0	380±4	18.3±0.5	3.5±0.2	575±14
A05	368±4	20.1±0.4	2.9±0.1	403±29
A5	379±4	19.1±0.4	2.9±0.2	423±75

Table 3.6: Mechanical properties of alumina pure and doped with SiCp [147].

In both composites the hardness slightly increases over pure alumina. The Young's modulus value is lower than the one, which would be expected from the rule of mixtures. There may be two reasons to explain this behavior: the existence of SiO_2 at the GBs and the presence of microcracks due to residual stresses between alumina grains and SiCp agglomerates. Moreover, it has been found that toughness is smaller in the composites than in pure alumina [147]. Concerning flexural strength no beneficial effect has been observed [147]. In contrast with the results reported in the literature, strength decreases with increasing the amount of SiCp.
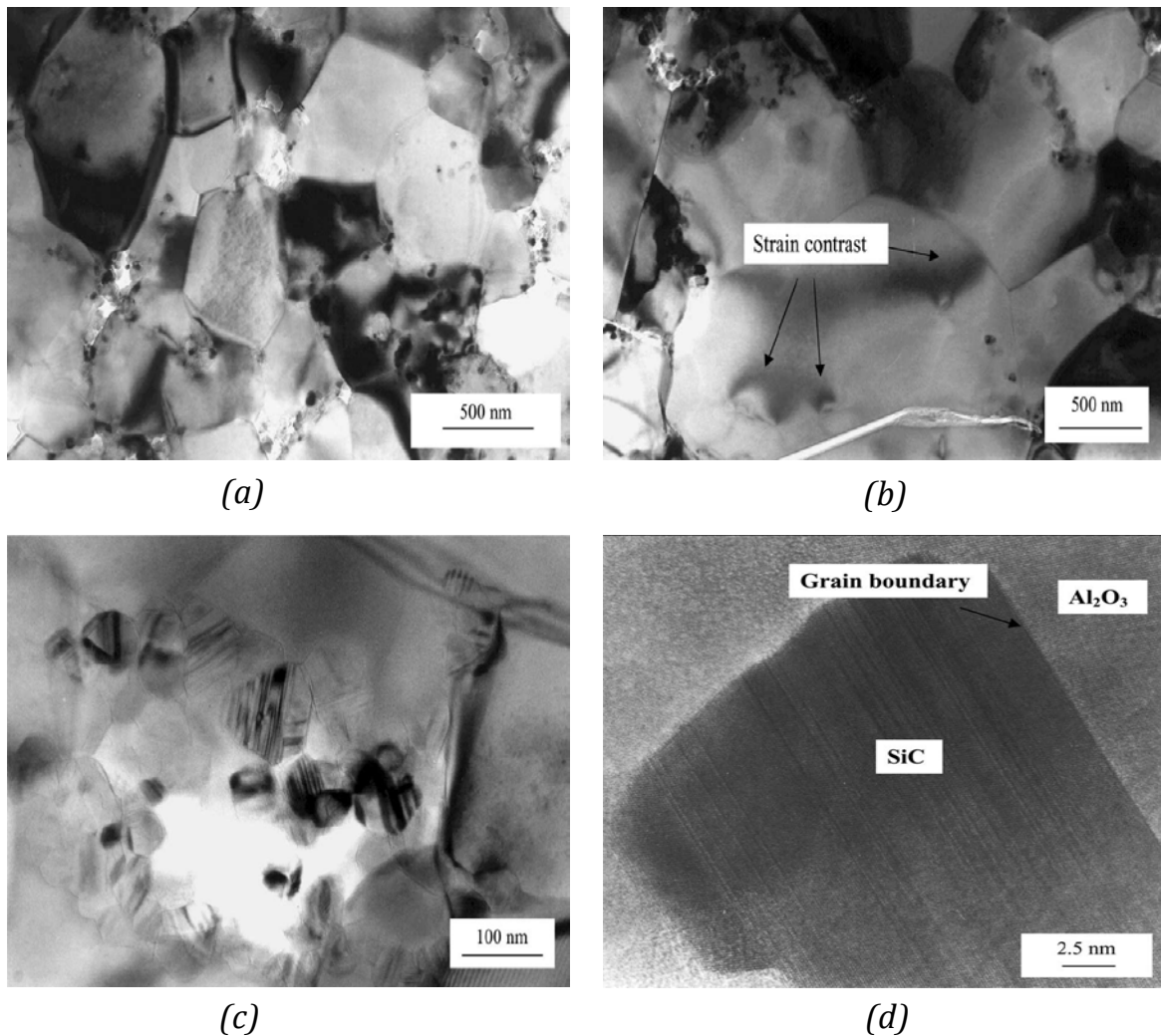
Figure 3.14: TEM images of A5. (a) SiCp are mainly located along alumina GBs. (b) Strain contrast around intergranular SiCp due to thermal expansion coefficient mismatch between Al_2O_3 and SiCp. (c) SiC grains exhibit numerous stacking faults and are embedded inside a glassy phase. (d) HRTEM image of a SiCp/Al_2O_3 interface. The GB is free of any amorphous phase (after Sciti et al. [147]).

3.3   Experimental installations

For low-frequency mechanical spectroscopy the most commonly used apparatus is the inverted torsion pendulum. In this work two types of pendulum have been used and they are presented below.

3.3.1 Differential Inverted Torsion Pendulum

The differential inverted torsion-pendulum works at sub-resonant frequencies (the system is set into forced vibration at a frequency below its resonant frequency). The pendulum is called differential because the data are obtained by comparing the strain of the sample with the one of an elastic reference. This method cancels the influence of the pendulum resonance on the mechanical-loss spectra, so that there is no need to subtract the background due to resonance artifacts. Such a pendulum permits one to perform measurements of the mechanical loss and dynamic shear modulus as a function of temperature (at a constant frequency and applied stress amplitude) or frequency (at a constant temperature and applied stress amplitude) or stress-amplitude (at a constant temperature and frequency).

The pendulum characteristics are:
- Temperature range: 300 -1600 K.
- Frequency range: 10^{-4} - 10 Hz.
- Stress amplitude range: 10^{-1} - 8 MPa.

A basic description of this apparatus was given by Gadaud et al. [154]. A sketch of the general experimental setup is given in Figure 3.15 and a general picture of the system is shown in Figure 3.16.

Mechanical part

In this apparatus two flat bar specimens are mounted in series, one being measured (1) and the other one acting as an elastic reference (2). The samples size 36 x 4 x 1 mm³ are clamped in the grips with a system of tantalum blocks and niobium pins. These elements have been chosen because of their thermal expansion coefficients, so that during increasing temperature they will insure a good grip. The two specimens are gripped at 90° to suppress parasitic transverse vibrations. The elastic reference is made of WC-Co. The bottom rod is fixed, while the upper one is free to oscillate around the pendulum axis. To favor only one degree of freedom, i.e. torsion of the specimen, the suspension of the upper rod is composed of two stretched tungsten wires (thin enough to have a negligible rigidity in torsion), which are held in place by two balance beams (6). The balance beams (6) allow for the thermal expansion of the elements in the heating zone.
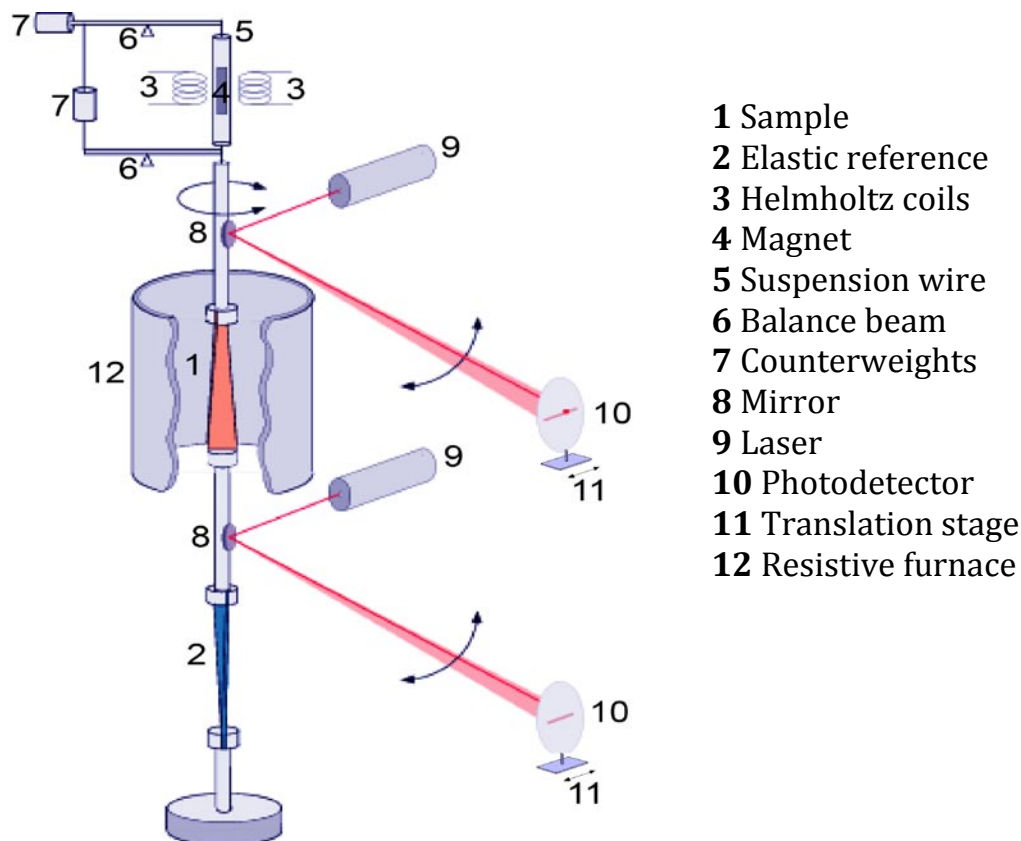
Figure 3.15: Sketch of the differential inverted torsion-pendulum. The sample (1) is mounted in series with an elastic reference (2). The sample (1) is surrounded by a resistive furnace (12). The torsional vibrations are given by the Helmholtz coils (3) and a magnet (4). The deflection is measured optically by a system of laser – mirror – photodetector (9, 8, 10).

The rods in the heating area are made of titanium to limit the thermal conductibility. All the other mechanical components are of molybdenum alloy (TZM). The pendulum is equilibrated by counterweights (7) to suppress the axial compression on the specimens. The torsion excitation is applied to the pendulum axis by means of two Helmholtz coils (3) acting on a permanent magnet (4) fixed on the upper rod. The strains of the sample and of the elastic reference are measured by the deflections of two laser beams (9) reflected onto two circular linear photodetectors (10) by the mirrors (8) fixed above the sample and the reference. Each photodetector is placed on a translation stage (11), which enables one to correct the static drift of the laser spot due to plastic deformation of the specimens. The studied sample is placed in a non-inductive tubular resistance furnace (12) cooled by refractory screening and water circulation. The whole apparatus (Figure 3.15), except the lasers and photodetectors, is maintained under secondary vacuum (10^{-5} mbars) by diffusion (14) and a primary rotary (15) pumps. In order to avoid external mechanical vibrations the pendulum is mounted on a damping frame (16).

Figure 3.16: General view of the experimental installation.

Electronic part

The control and the acquisition electronics are presented in Figure 3.17. A Schlumberger-Solatron 1250 frequency response analyzer is used as a generator and two-channel analyzer. The generated sinusoidal signal is applied, after amplification, to the Helmholtz coils (3). The two photodetector signals are processed by the Solatron, which returns the phase lag and amplitude ratio of two signals. A computer (PC) converts these two values into the sample mechanical-loss angle and the sample normalized shear modulus (sample modulus/elastic reference modulus). The temperature measurement and regulation is made by Eurotherm 818P, which controls a Delta SM 120-25D power supply. The temperature is measured by a Pt/PtRh10% thermocouple (type S) placed on the furnace inner wall. To get the real temperature around the sample, high temperature calibration of the thermocouple has been performed. It was established that the thermal gradient in the sample is less than few degrees and the temperature is corrected automatically by the computer. A HP acquisition unit is used for the static drift compensation of the laser spots. The compensation is executed between each two measurements of the mechanical loss. The photo-detector positioning is done by computer-control translation stage movement. The PC controls both the measurements and the data storage.
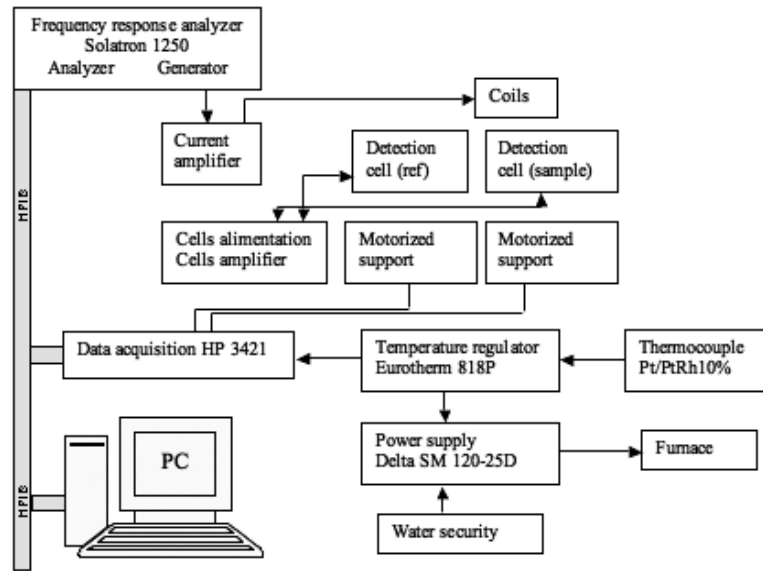
Figure 3.17: Schematic representation of the control and acquisition electronics.

Calculation of the mechanical-loss angle and dynamic shear modulus

With the described differential inverted torsion pendulum the phase lag and the amplitude ratio between the sample and elastic reference are measured. The mechanical loss *tan(Φ)* can be calculated from the phase difference $\Phi = \Phi_1 - \Phi_2$ of the signals detected above the sample and reference, and the normalized shear modulus $G_{sample}/G_{reference}$ is obtained from the ratio of their amplitudes *A*. Analytical expressions of these quantities can be obtained from the rheological model in Figure 3.18, which describes two specimens in series.
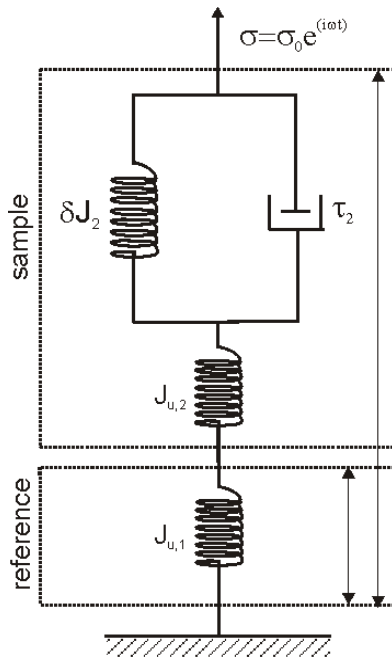
Figure 3.18: Rheological model that describes two specimens in series.

The deformation above the sample is expressed as:

$$\alpha_2 = \alpha_{2,0}exp[i(\omega t - \phi_2)] = \beta\frac{l_2}{c}\left[J_{u,2}\left(1 + \frac{\delta J_2}{J_{u,2}}\frac{1-i\omega\tau}{1+\omega^2\tau^2}\right)\right]\sigma + \beta\frac{l_1}{c}J_{u,1}\sigma)\ (3.1)$$

The deformation above the reference is expressed as:

$$\alpha_1 = \alpha_{1,0}exp(i\omega t) = \alpha_{1,0}exp(i\omega t) = \beta\frac{l_1}{c}J_{u,1}\sigma \qquad (3.2)$$

According to the rheological model (Figure 3.18), one can see that the angle α_2 is composed of the deformation of the sample and the reference, while α_1 depends only on the deformation of the elastic reference. In the above expressions, l_1 and l_2 are the lengths of the reference and sample, respectively. The thickness c and the coefficient β depend on the specimen dimensions. As both specimens have a width of 4 mm and thickness of 1 mm and because the ratio $width/thickness = 4$, thus $\beta = 1$ [155]. By definition $A = \alpha_{1,0}/\alpha_{2,0}$ we obtain for the mechanical loss and shear modulus the following expressions:

$$tan(\Phi)_{sample} \approx \frac{1}{1-A}tan(\Delta\phi) \qquad \frac{G_{sample}}{G_{reference}} \equiv \frac{G_s}{G_r} \approx \frac{l_2}{l_1}\frac{A}{1-A} \qquad (3.3)$$

The damping of the elastic reference during temperature measurements is small enough and can be neglected.

3.3.2 Simple Inverted Torsion Pendulum

Another experimental apparatus used in the present study is a simple inverted torsion-pendulum (developed by Feusier [156]) for measuring the mechanical loss in a large range of temperatures from 300 K up to 1800 K and frequencies from 10 mHz to 10 Hz. This installation is working in a sub-resonant regime. The internal friction measurements can be performed either in isochronal conditions (as a function of temperature at a constant frequency) or in isothermal conditions (as a function of frequency at a constant temperature). A sketch of the general experimental setup is given in Figure 3.19 and a general picture of the system is shown in Figure 3.20. In this pendulum a sample (1), which has a rectangular cross-section of 4 x 1 mm² and a variable length, is clamped on the pendulum rod. The lower part of the rod is fixed to the bottom of the pendulum, while it is suspended on its top with thin tungsten wires (4). The tungsten wires (4) are connected to a double balance system (6) to accommodate the thermal expansion.
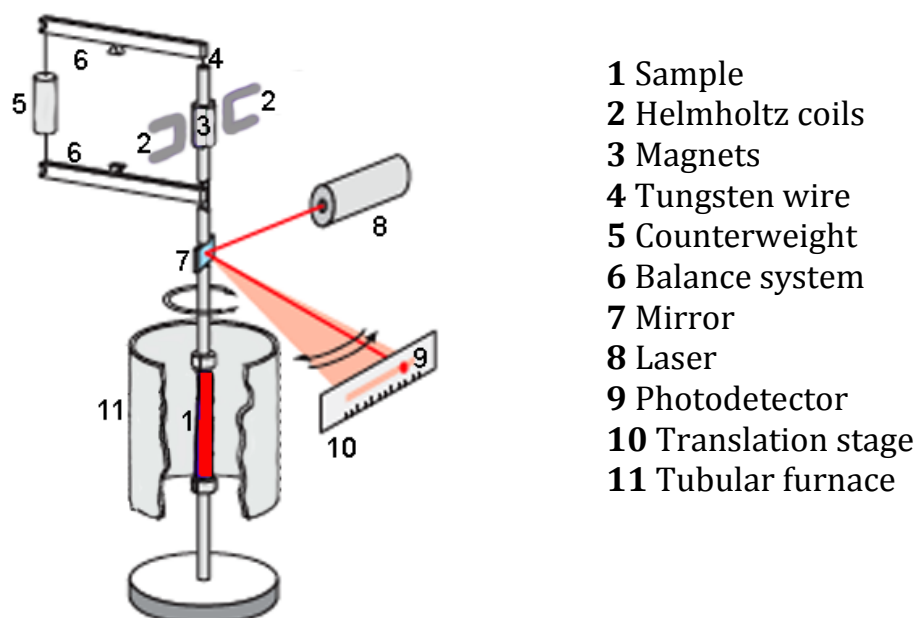
Figure 3.19: Sketch of the simple inverted torsion-pendulum. The sample (1) is fixed at both ends to the pendulum rod which is suspended at its top with tungsten wires (4). The sample is surrounded by a resistive furnace (11). The torsional vibrations are driven by Helmholtz coils (2) and a magnet (3). The deflection is measured optically by a system of laser-mirror-photodetector (7, 8, 9).

The weight of the rod and sample are equilibrated by counterweights (5). The torsional vibrations are induced through two Helmholtz coils (2) and a permanent magnet (3) that is fixed on the upper part of the rod. The oscillations are detected by a laser (8) beam pointed on a mirror (7) fixed on the rod above the sample and so reflected to a linear photodetector (9). The photodetector is fixed on a translation stage (10), which corrects the static drift of the laser spot due to plastic deformation of the studied specimen. A tubular resistive furnace (11) surrounds the studied sample (1) and the rod extremities. The whole installation, except for the laser and the photodetector, is set under vacuum of 10^{-5} mbar using a primary rotary pump and a secondary oil diffusion pump. The pendulum is mounted on a damping frame (10) to prevent the external parasite vibrations. The excitation signal is obtained by means of a frequency response analyzer - Schlumberger-Solatron 1250 - that is used as a signal generator and two-channel analyzer (measuring the phase lag and the ratio between the excitation signal and the strain signal). The generated sinusoidal signal is applied, after amplification (by a bipolar amplifier) to the Helmholtz coils. The response is detected by a photodetector, amplified, and returned to Schlumberger-Solatron, which also analyzes the phase lag and the ratio of the amplitudes between the excitation and response signals. An oscilloscope is used to visualize the excitation and strain signals during experiment.

The heating system consists of a Eurotherm 903 P (PID), which controls a

power supply Hewllet Packard 6030 A and a thermocouple Pt/RhPt (type S) placed on the furnace inner wall to read the temperature close to the specimen. The length of the tubular furnace insures a low thermal gradient along the specimen. All components are connected to a Dell Dimension DV051 Intel(R) personal computer (PC) with a HPVee software, which controls the measurements and experimental data acquisition.

With this pendulum the following parameters can be measured:
- The phase lag Φ between the excitation and strain signals.
- The ratio of amplitudes (excitation and response), which corresponds to the shear modulus G.
- The temperature T.
- The excitation frequency ω.
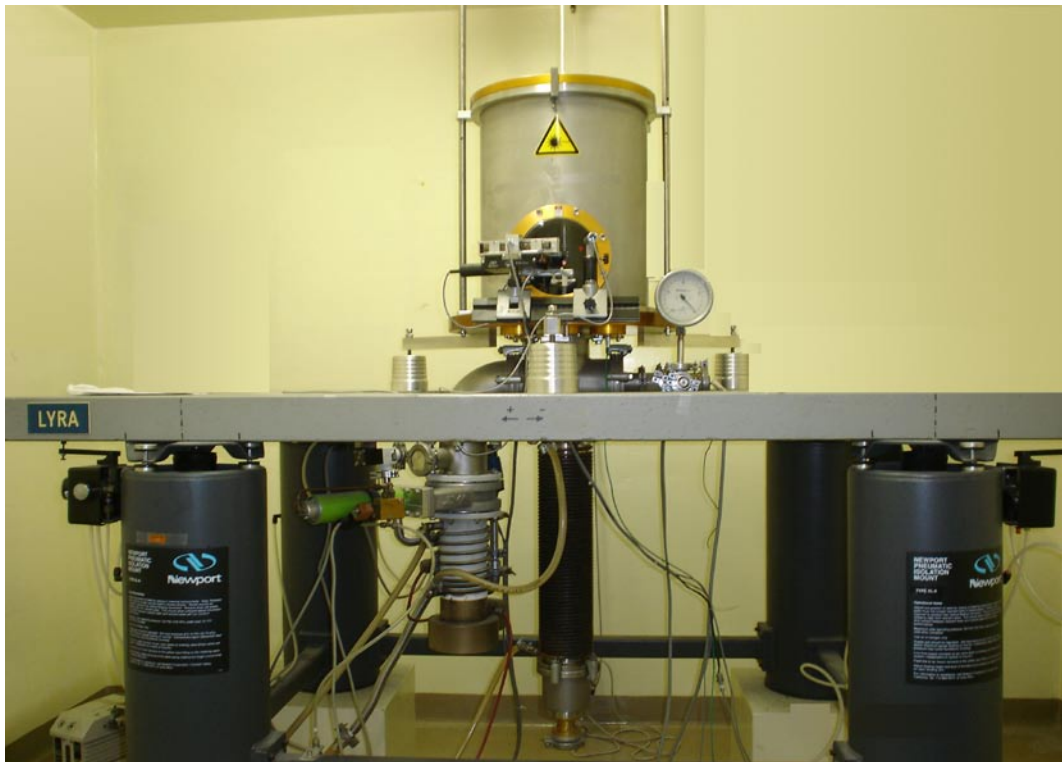
Figure 3.20: General view of the experimental installation.

Chapter 4

Results and analysis

In this chapter are presented the mechanical spectroscopy results obtained in zirconia pure, impure and doped with multiwalled carbon nanotubes or silicon carbide whiskers or silicon carbide particles, as well as alumina pure and doped with silicon carbide particles.

4.1 Polycrystalline zirconia

4.1.1 Typical spectrum of zirconia 3Y-TZP grade

Figure 4.1 displays a characteristic spectrum: mechanical loss $tan(\Phi)$ and dynamic shear modulus G_s/G_r as a function of temperature in zirconia 3Y-TZP grade, denoted here Z0 for simplicity. The measurements were performed at: a frequency of 1 Hz, a heating rate of 1 K/min and the amplitude of the applied stress of 7 MPa.
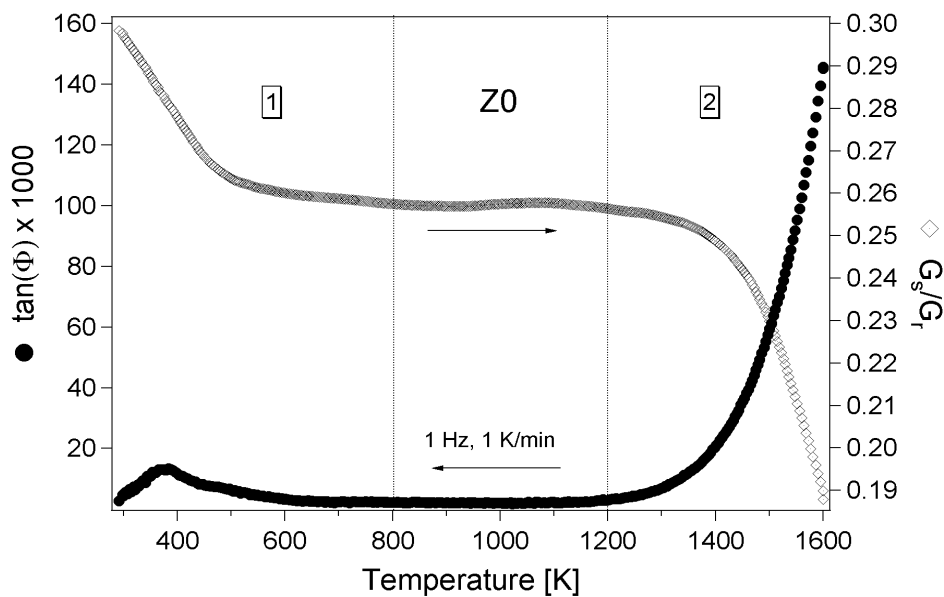
Figure 4.1: Characteristic spectrum of zirconia 3Y-TZP (Z0): mechanical loss tan(Φ) and dynamic shear modulus G_s/G_r as a function of temperature.

In Figure 4.1, two regions present a special interest:

- Low temperature part (300 - 500 K). A mechanical-loss maximum is observed at about 375 K accompanied with a modulus defect. Similar spectrum components have been observed and studied by other authors [15, 83, 157]. The activation enthalpy was found to be 89 kJ/mol and the limit relaxation time $\sim10^{-14}$ s [83]. These values are characteristic of a point defect relaxation process. The maximum was found to be larger than a Debye peak by a factor of two [83]. The relaxation mechanism was interpreted as being due to the reorientation of "oxygen vacancy - yttrium cation" pairs, under the influence of the applied stress [157]. However, the complex elastic dipoles are dissociated above 800 K [158].

- High-temperature part (>1200 K). The mechanical loss increases monotonically accompanied by a decrease in the dynamic shear modulus. The high-temperature part of the mechanical loss will be analyzed more in depth below.

4.1.2 Analysis of the high-temperature exponential background

In Figure 4.2 are shown the results of mechanical-loss measurements performed at three different frequencies (0.1 Hz, 1 Hz and 10 Hz) as a function of temperature. The applied stress and the heating rate during measurement were fixed at 7 MPa and 1 K/min, respectively.
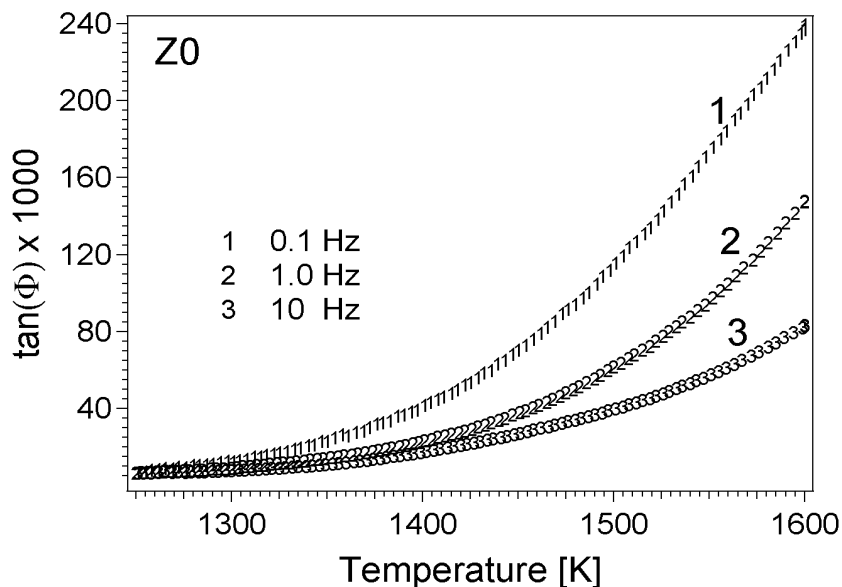

Figure 4.2: Mechanical loss as a function of temperature for three different frequencies: 0.1 Hz, 1 Hz and 10 Hz in Z0. The isochronal curves are shifted towards lower temperatures, when the frequency is decreased.

Starting from 1350 K the mechanical loss increases exponentially with temperature. This means that anelastic strain is not restricted in this temperature

range. The curves are displaced towards higher temperatures when the frequency is higher. The exponential form of the curves in this temperature ranges (Figure 4.2) may be the lower temperature part of a peak (or perhaps more peaks) situated at higher temperature than 1600 K.

Actually, a peak appears in the isothermal spectra performed between 1400 K - 1600 K with frequency sweeps between 1 mHz and 10 Hz under an applied stress of 7MPa. The isothermal curves are displayed in Figure 4.3. The relaxation peak transforms into an exponential background at lower frequencies. The spectra are shifted towards lower frequencies for lower temperatures.
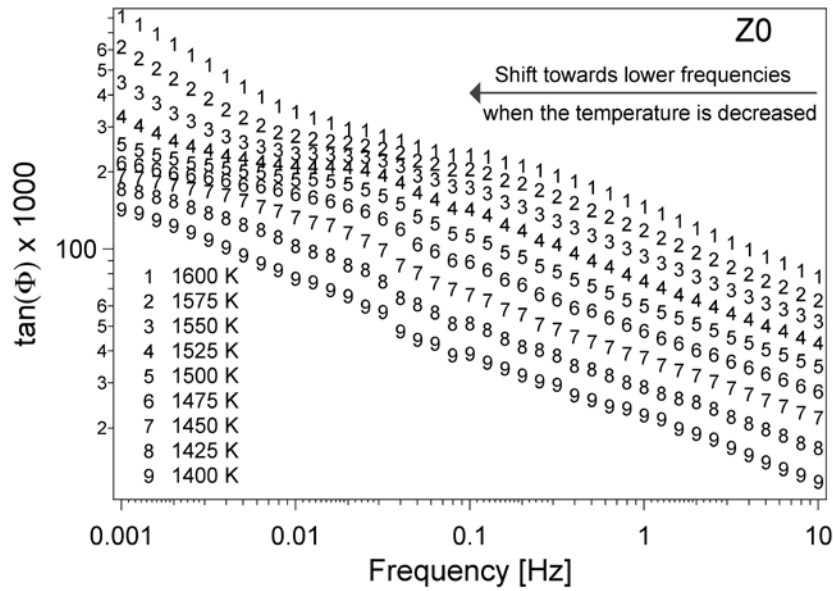
Figure 4.3: Frequency scans between 1 mHz – 10Hz for nine different temperatures (1400 K – 1600 K). The mechanical-loss spectra are composed of a peak that turns into an exponential background at lower frequency.

Then, temperature-frequency shifts of the isochronal (Figure 4.2) and isothermal curves (Figure 4.3) indicate that the involved relaxation mechanisms are thermally activated. The activation parameters, activation enthalpy ΔH_{act} and limit attempt frequency ν_o can be estimated from isochronal and isothermal curves.

Activation parameters

The evaluation of the activation enthalpy ΔH_{bck} from the isochronal spectra plotted in Figure 4.2 can be done in the following way:
- Taking in a first approximation the equation (2.36) we can use the definition:

$$\Delta H_{bck} = -\frac{1}{R}\frac{\partial(Ln(tan(\Phi)))}{\partial\left(\frac{1}{T}\right)} \tag{4.1}$$

73

- Therefore, plotting the isochronal curves from Figure 4.2 as *Ln(tan(Φ)) vs 1/Temperature*, we obtain a straight line if the equation (2.36) is obeyed. For instance, the slope of the 1 Hz curve yields ΔH_{bck} = 183 kJ/mol.
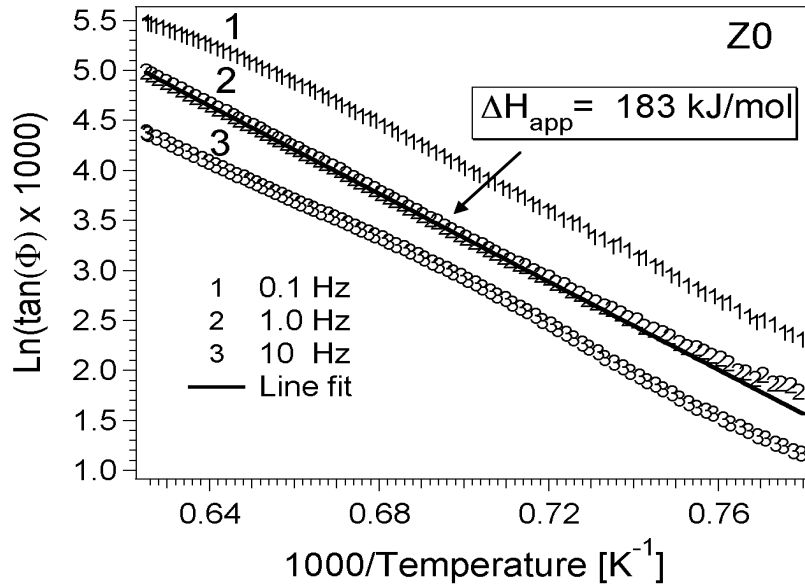

Figure 4.4: The logarithm of the mechanical loss as a function of the inverse temperature. ΔH_{bck} = 183 kJ/mol deduced from the slope of the spectrum at 1 Hz.

However, this value is much smaller than the one reported in literature for creep test in the low stress regime (ΔH_{act} = 500 - 700 kJ/mol [15, 24, 56, 57, 80-82]). This means that the method is simplistic and leads to an apparent quantitative value. The dissimilarity between ΔH_{bck} obtained from the slope of the mechanical-loss curves and the values reported in literature can be eliminated if we take into account a distribution in the relaxation time. For a constant relaxation strength Δ and a narrow distribution of the relaxation time τ, the high-temperature increase should be expressed not by equation (2.36), but by the equation (2.37) proposed by Schoeck [130]. In equation (2.37), the broadening factor $1/\alpha$ can be estimated from *log(tan(Φ)) vs. log(Frequency)* plots. When the relaxation mechanism deviates from a Debye one, $1/\alpha$ should be different from *1*. From the slope of the curve plotted in Figure 4.3, we get $\alpha = 0.28$, and then the broadening factor $1/\alpha$ = 3.57. These values are similar to the one obtained in polycrystalline tetragonal zirconia by Lakki [15]. Therefore, the activation enthalpy can be obtained from:

$$\Delta H_{act} = (1/\alpha) \cdot \Delta H_{bck} \qquad (4.2)$$

It follows immediately that ΔH_{act} = 653 kJ/mol, value which is in good agreement with the ones obtained by others in creep tests in zirconia [82].

Another method is to build a master-curve spectrum from a set of isothermal spectra. For instance in Figure 4.3 we can shift the isothermal spectra along the frequency-axis until all of them are superimposed on the curve obtained at 1600 K (Figure 4.5). This generic curve confirms that the high temperature spectrum in Figure 4.3 is composed of a relaxation peak (denoted here Pz) that appears at the middle-frequency part and a background which dominates the low-frequency range. The exponential background could be a part of another peak located at much lower frequencies.
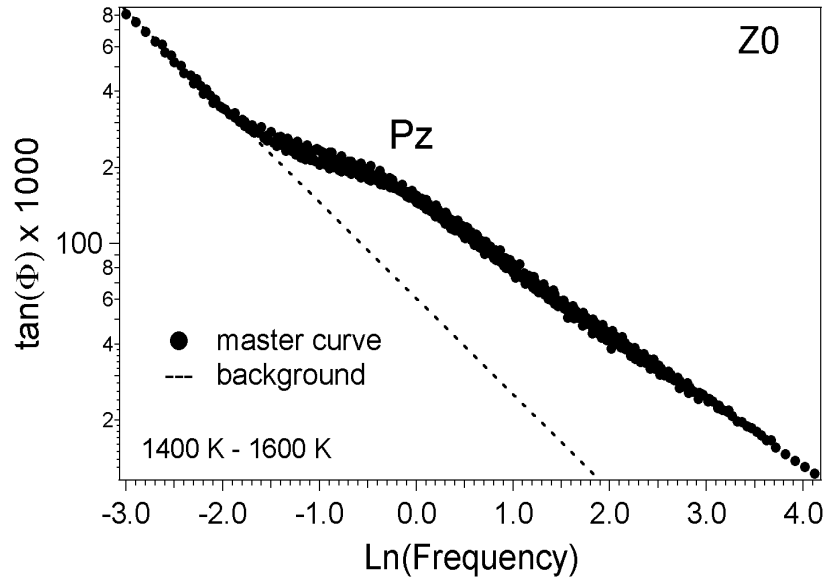
Figure 4.5: Master curve: from the shift along frequency axis. The spectra are superposed over 1600 K curve. The master-curve spectrum is composed of a peak and a low-frequency exponential background.

Reporting the frequency-shifts $\delta(Ln(Frequency))$ as a function of inverse of temperature $\delta(1/Temperature)$ we get an Arrhenius plot (Figure 4.6), the slope of which yields the activation enthalpy. In the present case, the activation enthalpy ΔH_{act} and the limit attempt frequency ν_o were found to be 679 kJ/mol and $2 \cdot 10^{+22}$ s^{-1}, respectively. Though the value of the activation enthalpy is in good agreement with the values obtained in creep tests, one can detect that there is problem with the limit attempt frequency, which is much higher than the Debye frequency (10^{+13} s^{-1}). A particular attention has then to be paid for the interpretation of the apparent values of the relaxation parameters. Because the isothermal spectrum was found from the shift as a whole, the activation enthalpy of the peak and the background is the same.

The master-curve spectrum (Figure 4.5) together with the activation enthalpy gives the same information as all spectra together in Figure 4.3. These facts indicate that one and the same structural defect is responsible for the entire high-temperature mechanical loss spectrum of zirconia.
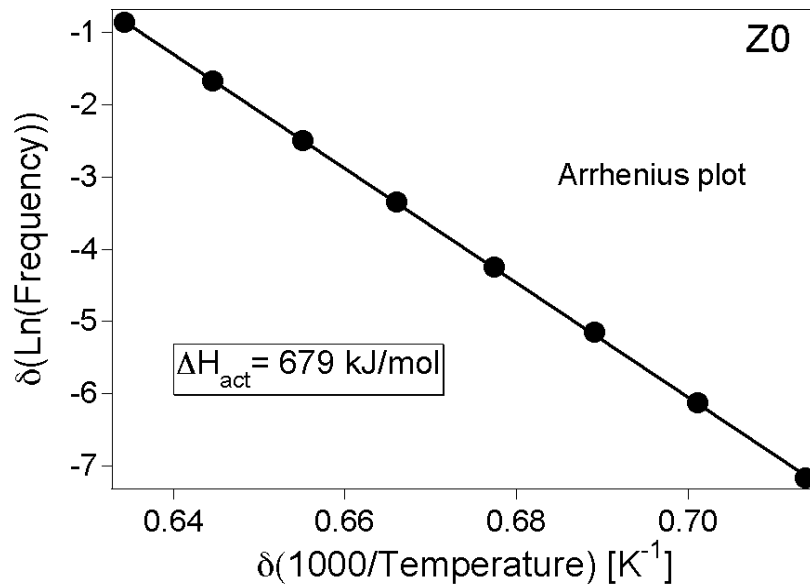
Figure 4.6: Arrhenius plot obtained from the frequency-temperature shift method. The activation enthalpy is 679 kJ/mol and the limit attempt frequency $2 \cdot 10^{+22}$ s^{-1}.

4.1.3 Effect of the stress amplitude

The influence of the applied stress amplitude on the isothermal spectrum measured at 1600 K is shown in Figure 4.7.
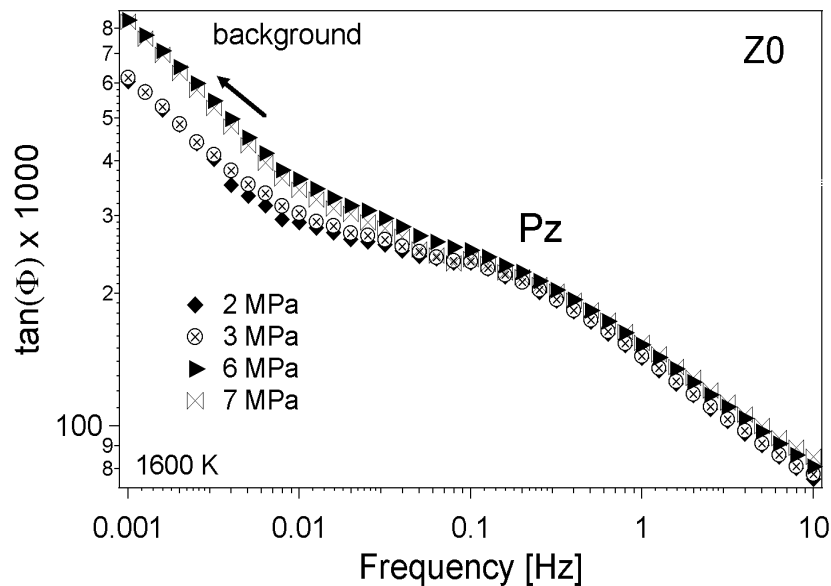

Figure 4.7: Effect of the vibration amplitude on the mechanical-loss spectrum.

Effectively, the mechanical-loss spectrum is composed of a peak and a background at much lower frequencies. The peak is not affected by the applied

stress and it is positioned at about 0.19 Hz. On the contrary, the low-frequency background increases with increasing the stress amplitude, for values higher than 3 MPa. A threshold stress is associated to the mechanism at the transition between local sliding (peak) and extensive sliding at the appearance of creep (exponential background).

4.1.4 Effect of the grain size

The influence of the grain size on the mechanical-loss spectra in zirconia is shown in Figure 4.8 and Figure 4.9. Three samples differing in grain sizes (0.30 μm, 0.50 μm and 0.70 μm) were measured between 1100 K – 1600 K at a frequency of 1 Hz. The amplitude of the applied stress and the heating rate were fixed at 7 MPa and 1 K/min, respectively. In Figure 4.8 the curves exhibit the typical behavior of zirconia: exponential increase of the mechanical loss with temperature. The mechanical loss is extremely sensitive to the grain size. The level of the damping increases when the grain size is decreased. It was found that the damping is inversely proportional to d = 0.83. Similar value was found by Lakki [83].
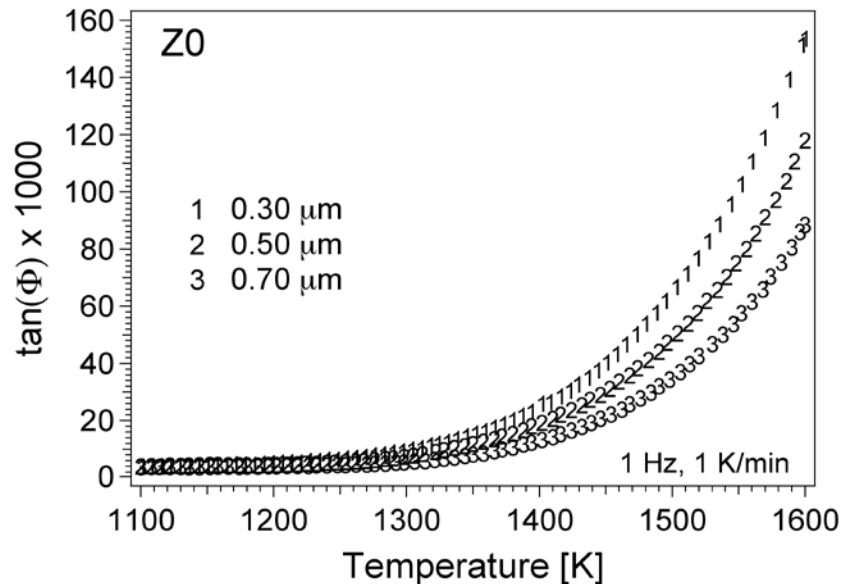

Figure 4.8: Mechanical-loss spectra obtained as a function of temperature for zirconia samples differing in the grain sizes: 0.30 μm, 0.50 μm and 0.70 μm.

Frequency scan were performed between 1 mHz - 10 Hz at 1600 K is shown in Figure 4.9. For all frequencies the mechanical loss is the highest in the sample with the smallest grain size. The spectrum is composed of a peak followed by an exponential background at lower frequency. It appears that the peak and the exponential background depend differently on the grain size.
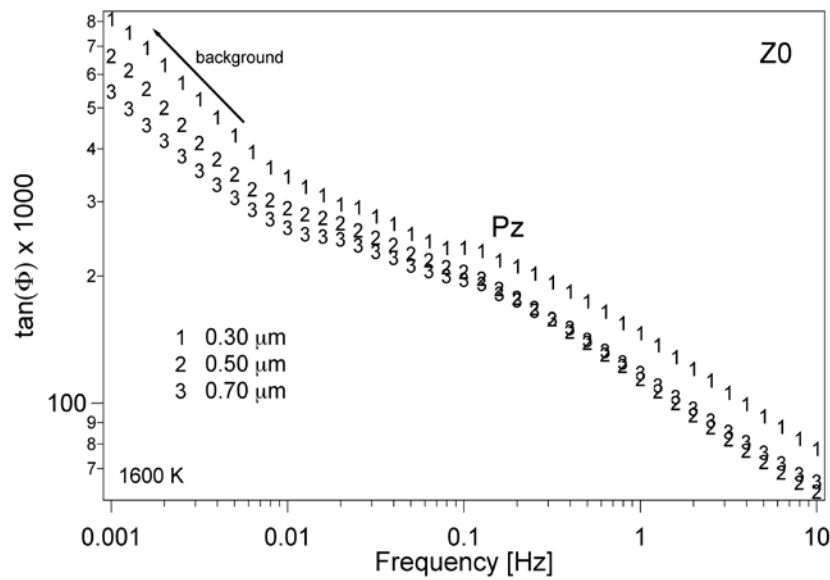
Figure 4.9: Mechanical-loss spectra obtained as a function of frequency at 1600 K for zirconia samples differing in the grain sizes: 0.30 μm, 0.50 μm and 0.70 μm.

4.1.5   Effect of the impurity

In Figure 4.10 and Figure 4.11 are compared the mechanical loss and the dynamic shear modulus spectra of two grades of ziconia: impure ZE and high purity Z0. In the starting powder of ZE the alumina content was five times higher than in Z0. The experimental curves were carried out under the same experimental conditions: 7 MPa, 1 Hz and 1 K/min. The mean grain size is 0.30 μm.
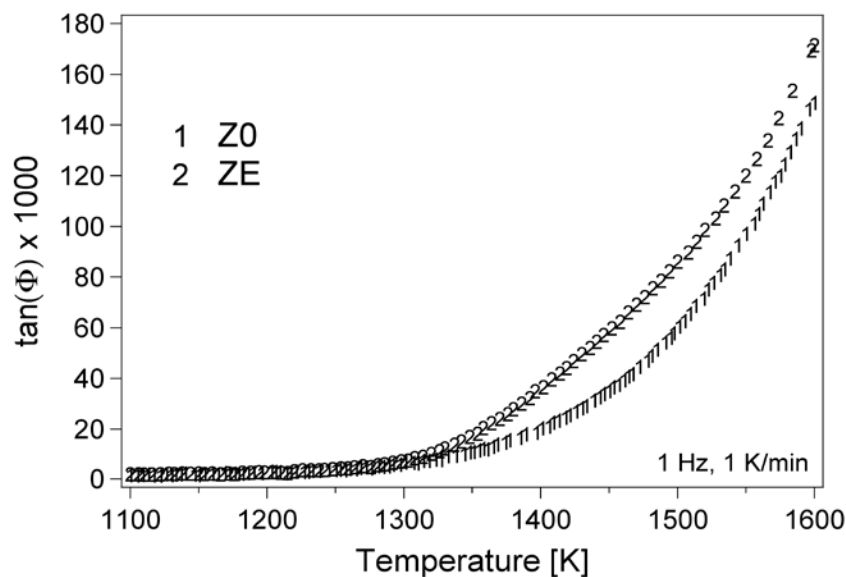

Figure 4.10: Comparison of the high-temperature mechanical loss tan(Φ) spectra of: impure ZE and high purity Z0.

In zirconia grades, the mechanical loss and the dynamic shear modulus spectra exhibit similar high-temperature behavior (Figure 4.10 and Figure 4.11). However, the mechanical loss increases faster with temperature in ZE than in Z0 (Figure 4.10). Moreover, an oblate peak denoted Pze is observable in the impure grade ZE. The peak is followed by an exponential background. The dynamic shear modulus decreases with temperature for both Z0 and ZE (Figure 4.11). The decrease of the dynamic shear modulus is steeper in ZE.
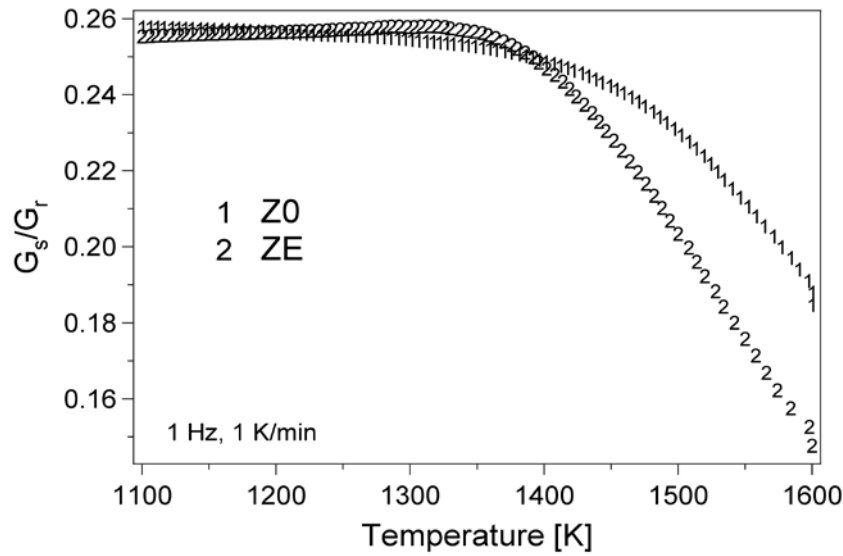

Figure 4.11: Comparison of the high-temperature dynamic shear modulus spectra of: impure ZE and high purity Z0. The mean grain size is 0.30 μm.

In Figure 4.12 are presented the results obtained in the frequency scan at nine different temperatures for the ZE sample. The applied stress was 7 MPa.
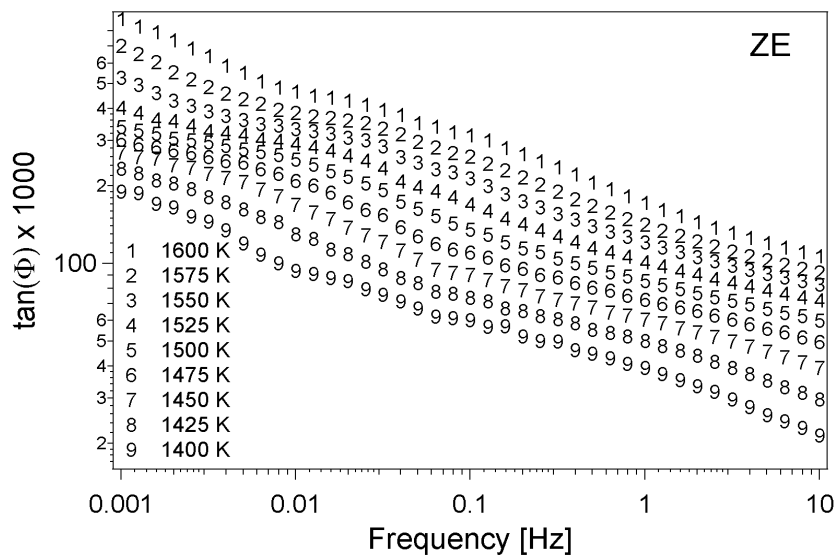

Figure 4.12: High-temperature isothermal-mechanical loss spectra of ZE: peak and low-frequency background.

The spectrum contains a peak superposed on a low frequencies background (Figure 4.12). The peak is not well resolved from the background. The isothermal curves are shifted towards lower frequencies for lower temperatures. The relaxation phenomenon is thermally activated.

The master-curve spectrum of ZE obtained from the shift of the entire isothermal curves over the spectrum at 1600 K is shown in Figure 4.13a. Similar to Z0 (Figure 4.5), the low-frequencies background and the peak Pz appear on the master-curve spectrum of ZE. At much higher frequencies is present another peak Pze. Actually, the peak Pze is not prominently distinct with respect to Pz.

The relaxation parameters were deduced from an Arrhenius plot (Figure 4.13b). Values of 617 kJ/mol and $4 \cdot 10^{+20}$ s^{-1} were obtained for ΔH_{act} and ν_o, respectively.
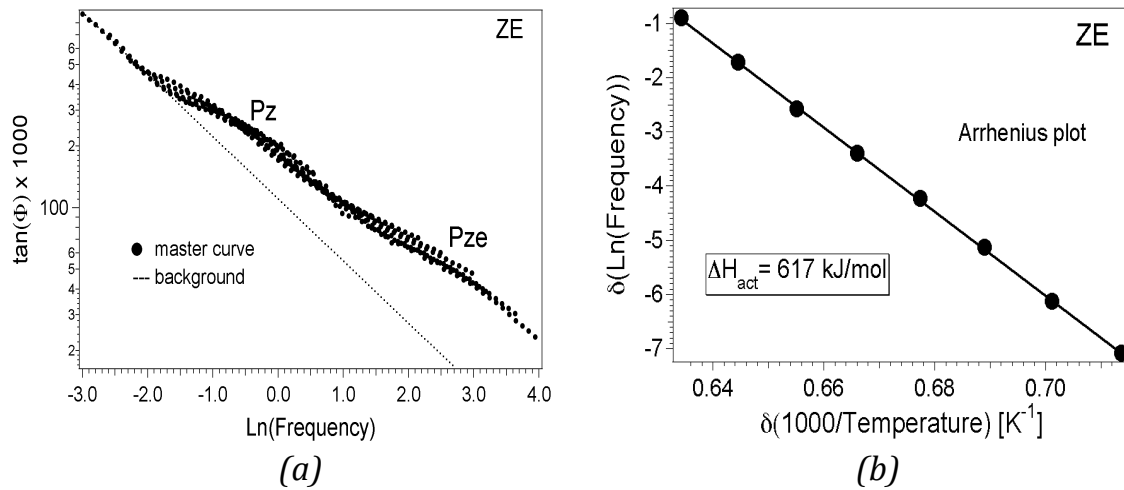

(a)   *(b)*

Figure 4.13: (a) Master curve: a high-frequency peak Pze, followed by a second peak Pz that transforms into an exponential background. (b) Arrhenius plot from the shift of the entire isothermal spectra.

4.1.6   Addition of multiwalled carbon nanotubes

Figure 4.14 and Figure 4.15 present the mechanical loss and the dynamic shear modulus spectra of undoped and doped zirconia with multiwalled carbon nanotubes: 0.5 wt. % (Z0.5CNTs) and 1.5 wt. % (Z1.5CNTs). The curves were obtained under the same experimental conditions of frequency, applied stress and temperature. The frequency and the heating rate were fixed during measurements at 1 Hz and 1 K/min, respectively. The amplitude of the applied stress was 7 MPa. The damping level decreases at 1600 K by about 30 % in Z0.5CNTs and by 50 % in Z1.5CNTs (Figure 4.14). A small peak Pc is observed in the composite spectrum with a higher amount of CNTs. The peak is situated at about Tp ~ 1500 K and has a magnitude of $46.75 \cdot 10^{-3}$. The peak is not present in Z0.5CNTs and in Z0 samples, where is observed just an exponential increase
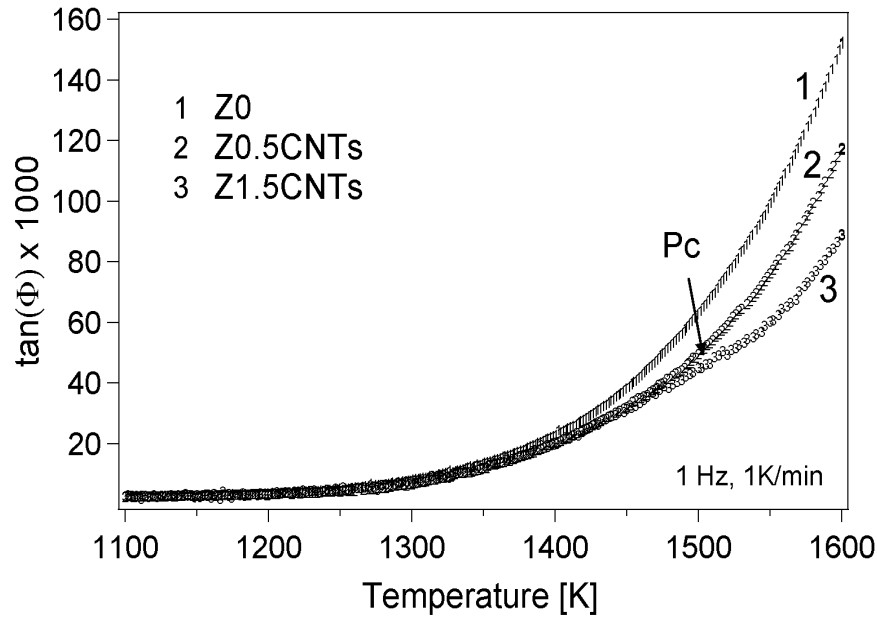
of the mechanical loss with temperature.

Figure 4.14: Mechanical-loss spectra for three different grades of zirconia. The exponential background is smaller in zirconia composites. A relaxation peak appears in Z1.5CNTs.

In Figure 4.15 for all grades of zirconia the modulus exhibits a typical behavior in this temperature range. The shear modulus is higher in composites, but decreases with the addition of CNTs. This may be due to an increase in porosity, by addition of the CNTs.
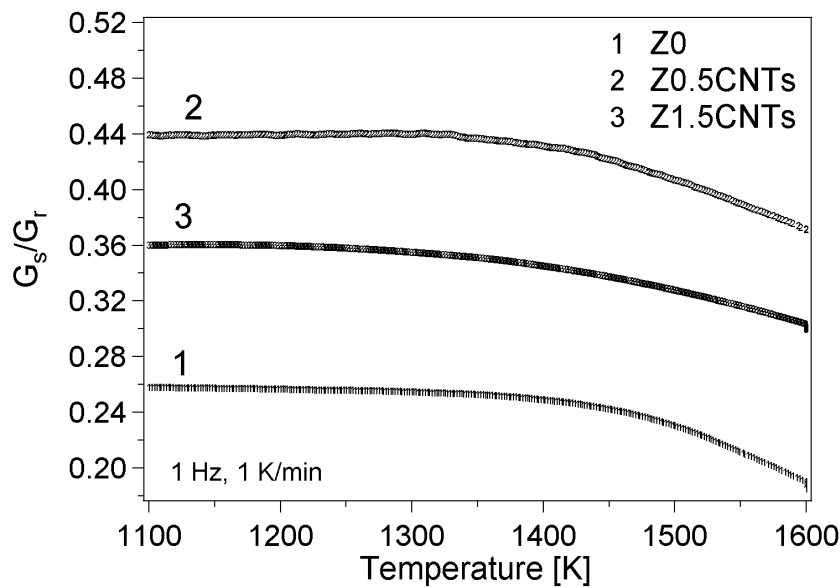

Figure 4.15: Dynamic shear modulus spectra for three different grades of zirconia. The moduli are higher in CNTs-zirconia composites.

Isothermal-mechanical loss spectra of composites Z0.5CNTs and Z1.5CNTs are reported in Figure 4.16a and Figure 4.16b. Again one observes a shift of the curves towards low frequency when temperature is decreased. The relaxation mechanisms are thus thermally activated.
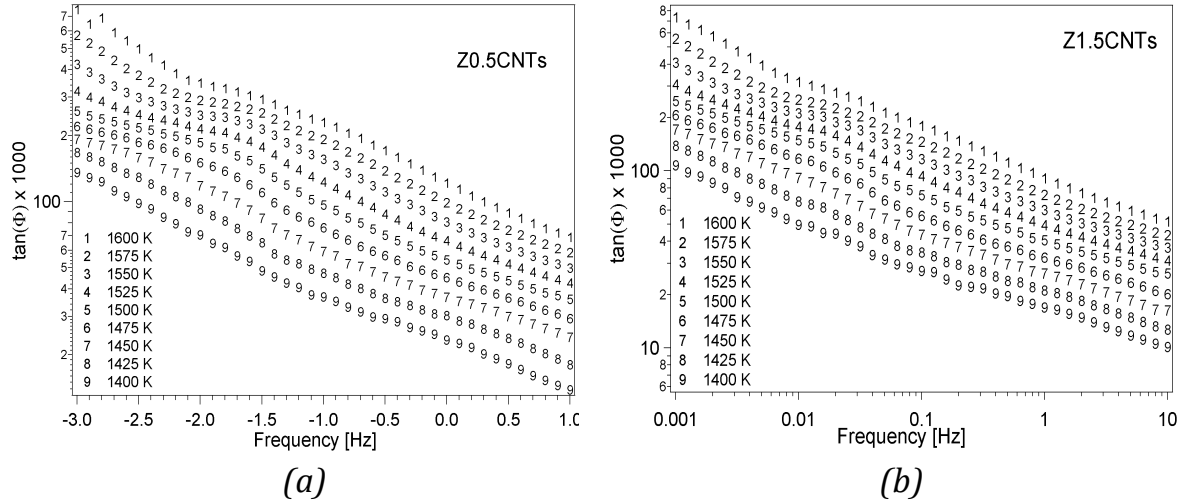

Figure 4.16: Mechanical loss of (a) Z0.5CNTs and (b) Z1.5CNTs as a function of frequency.

By shifting the isothermal spectra of Z0.5CNTs and Z1.5CNTs along frequency-axis until they superimpose over the spectrum at 1600 K we obtain a master-curve spectrum (Figure 4.17a and Figure 4.17b).
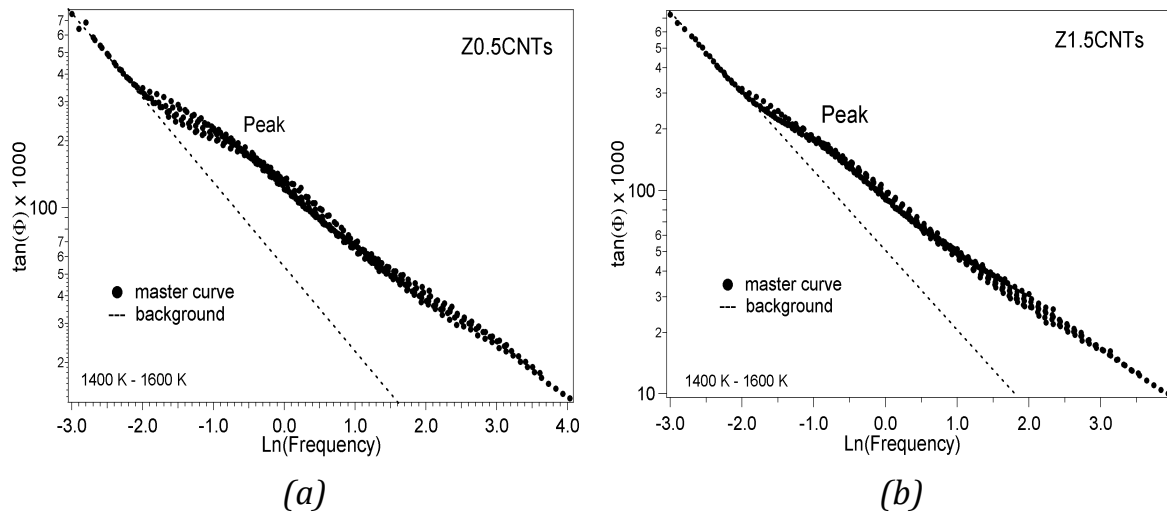
Figure 4.17: Master curves: (a) Z0.5CNTs and (b) Z1.5CNTs. The spectra are composed of a peak, which turns into a background at lower frequencies.

Similar to Z0 (Figure 4.5), the master spectra are composed of a peak and a background at lower frequencies in both Z0.5CNTs and Z1.5CNTs composites (Figure 4.17). From the temperature-frequency shifts of these spectra, ΔH_{act} and ν_o are obtained through Arrhenius plots (Figure 4.18a and Figure 4.18b).

The obtained values were 643 kJ/mol and $1 \cdot 10^{+21}$ s^{-1} for Z0.5CNTs, and 636 kJ/mol and $5 \cdot 10^{+20}$ s^{-1} for Z1.5CNTs , respectively.

(a)   *(b)*
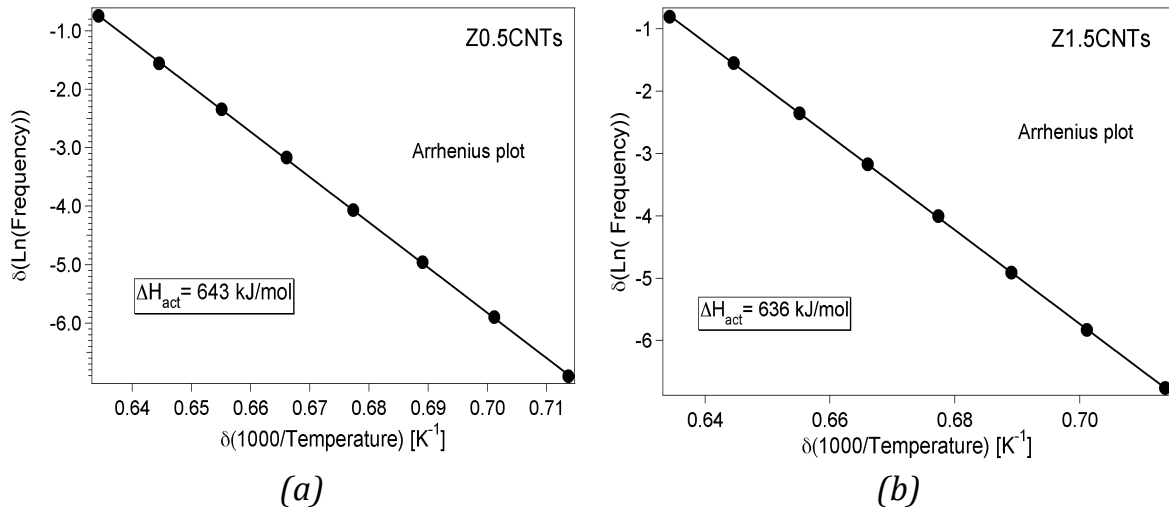
Figure 4.18: Arrhenius plots: (a) Z0.5CNTs and (b) Z1.5CNTs from the shift of the entire isothermal spectra as a function of inverse of temperature.

Effect of thermal cycling

Figure 4.19 shows the mechanical-loss spectra obtained during successive heating and cooling at a heating rate of 1 K/min and for a frequency of 1 Hz.

Figure 4.19 Effect of thermal treatments: a peak and an exponential increase in as received state spectrum, peak disappearance during cooling.

In the as received state the mechanical-loss spectrum measured upon first heating exhibits a "peak" at about 1500 K followed an exponential increase up to 160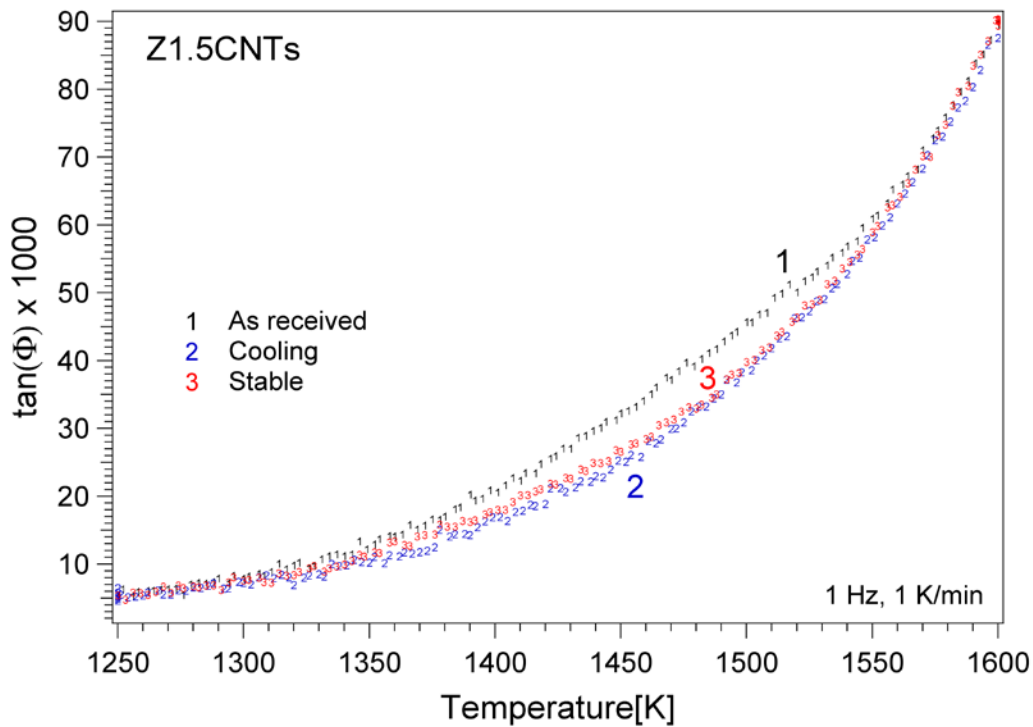0 K. This peak has disappeared on the curve obtained upon subsequent cooling. A stable spectrum is then obtained, which exhibits only monotonous increase of damping with temperature.

Creep test

Creep tests (in compression) were performed at 1550 K and under an applied stress of 6 MPa for undoped and 1.5 wt. % CNTs-doped zirconia. Figure 4.20 shows the creep strain as measured during these tests in Z0 and Z1.5 CNTs. Strain in composite is much smaller than in undoped zirconia. This is in agreement with the mechanical spectroscopy results, which indicate a lower level of the damping in the case of reinforced zirconia composites. A lower level of the exponential background in the mechanical-loss spectrum would mean a better resistance to creep.
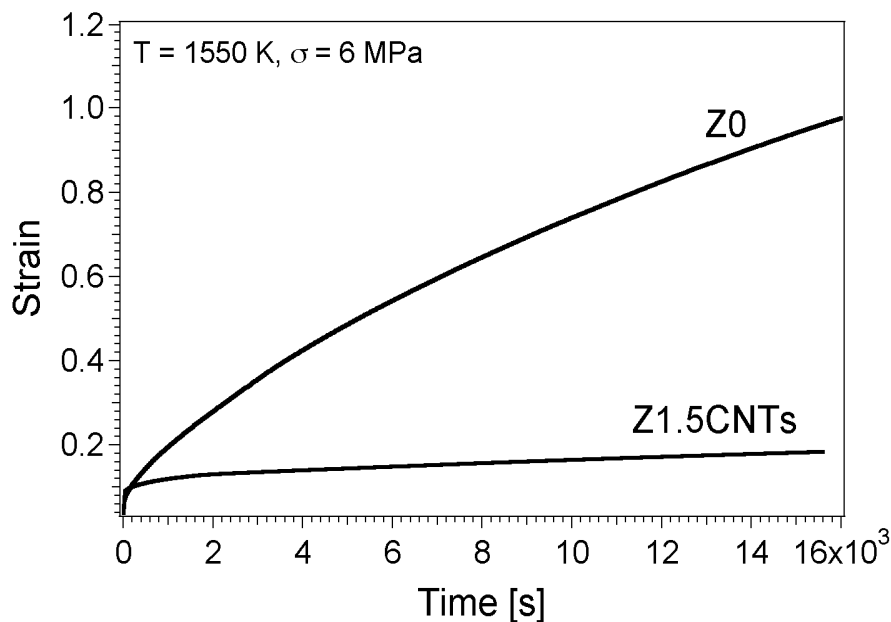
Figure 4.20: Strain-time curves obtained during creep in compression of Z0 and Z1.5CNTs at 1550 K under a stress of 6 MPa. The Z1.5CNTs creeps slower than Z0.

4.1.7 Addition of silicon carbide whiskers

Mechanical loss and dynamic shear modulus spectra of 0.5 wt. % (Z0.5SiCw) and 1.5 wt. % (Z1.5SiCw) silicon carbide whiskers doped zirconia are compared with the one of high purity Z0 in Figure 4.21 and Figure 4.22. The spectra were measured under the same experimental conditions: 1 Hz, 1 K/min and 7 MPa. The average grain size is about 0.30 μm for all samples. In Figure 4.21, at 1600 K, the level of *tan(Φ)* in Z1.5SiCw is reduced by 30 %, while in Z0.5SiCw

by 7 % with respect to Z0. SiCw addition to polycrystalline zirconia leads to the formation of a dissipation peak denoted here Pw. In both composites Pw is situated at ~ 1500 K.

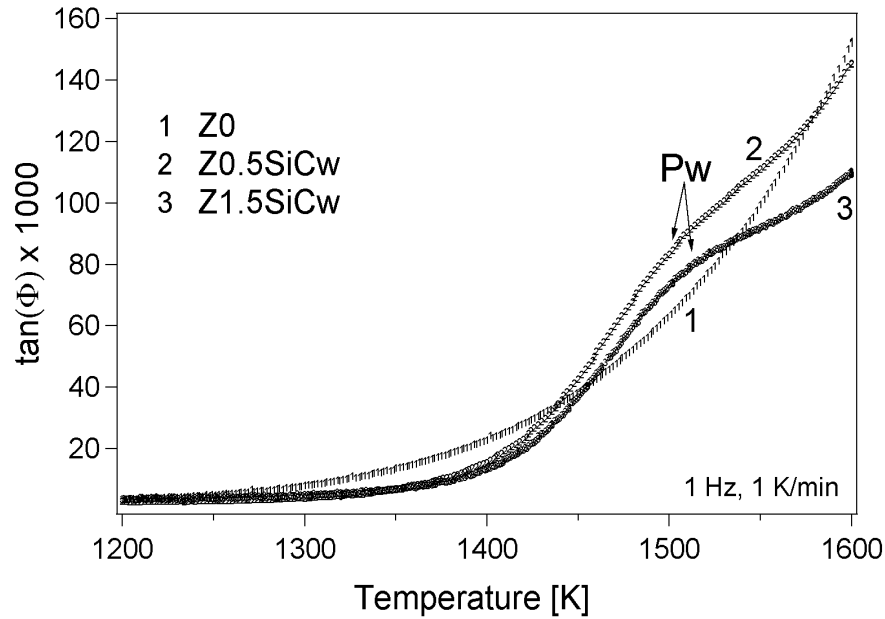*Figure 4.21: Comparison of the high-temperature mechanical loss spectra obtained as a function of temperature in two different grades of zirconia.*

The dynamic shear modulus is higher in both SiCw composites with respect to Z0 over all the temperature range investigated (Figure 4.22).
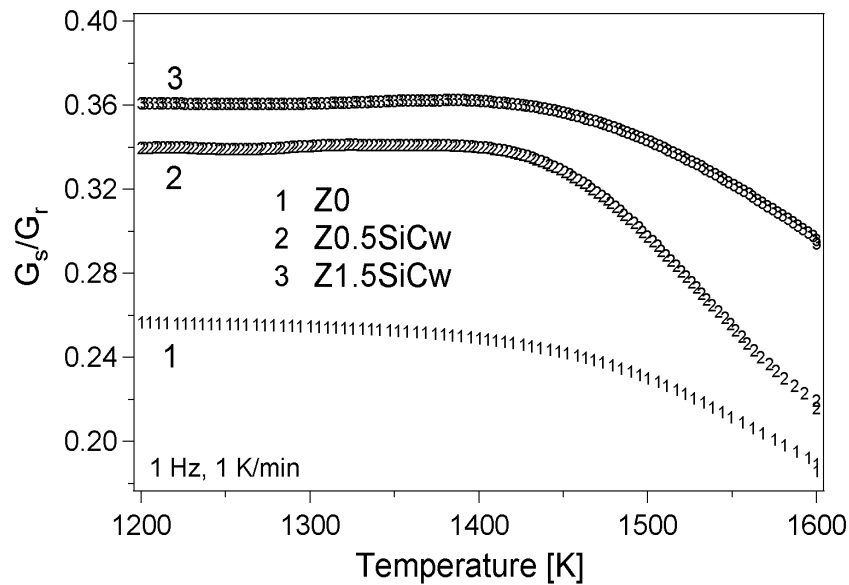

Figure 4.22: Comparison of the high-temperature shear modulus spectra obtained as a function of temperature in pure and SiCw-doped zirconia.

The decrease of the rigidity (shear modulus) when temperature is increased starts at 1300 K in Z0, while in the composites at about 1400 K. The shape of the modulus behavior depends of the SiCw addition.

Isothermal measurements performed in Z0.5SiCw and Z1.5SiCw are shown in (Figure 4.23a and Figure 4.23b). The spectra are displaced towards lower frequency at lower temperatures, which means a thermally activated process.

(a)   *(b)*
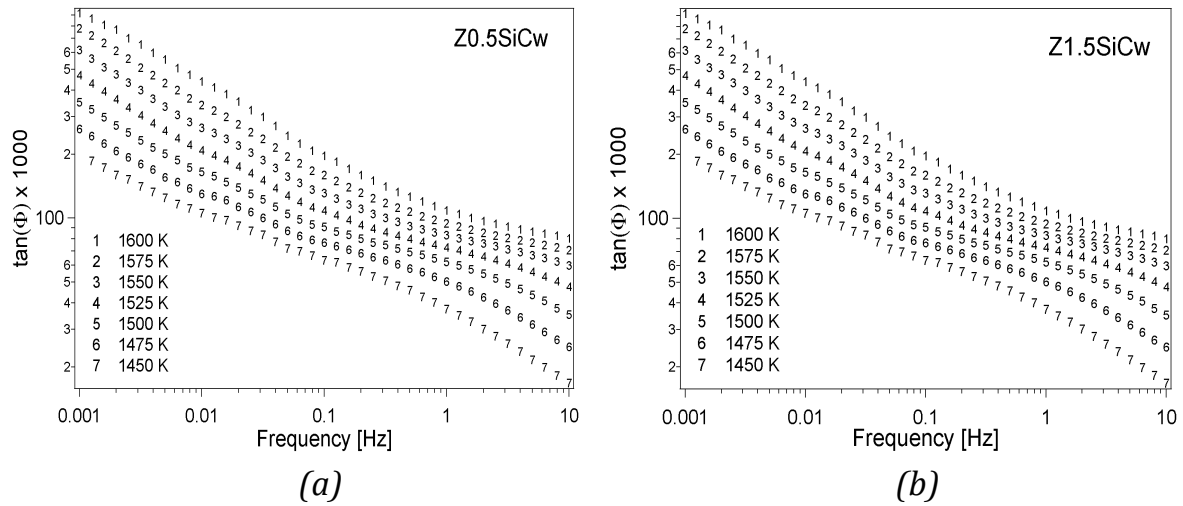
Figure 4.23: Mechanical-loss spectra vs. frequency: (a) Z0.5SiCw and (b) Z1.5SiCw.

Similar to Z0 (Figure 4.5), the master-curve spectrum in Figure 4.24a and Figure 4.24b is composed of a well resolved peak and an exponential increase. The Pw peak is situated at higher frequencies than Pz (Figure 4.5).

(a)   *(b)*
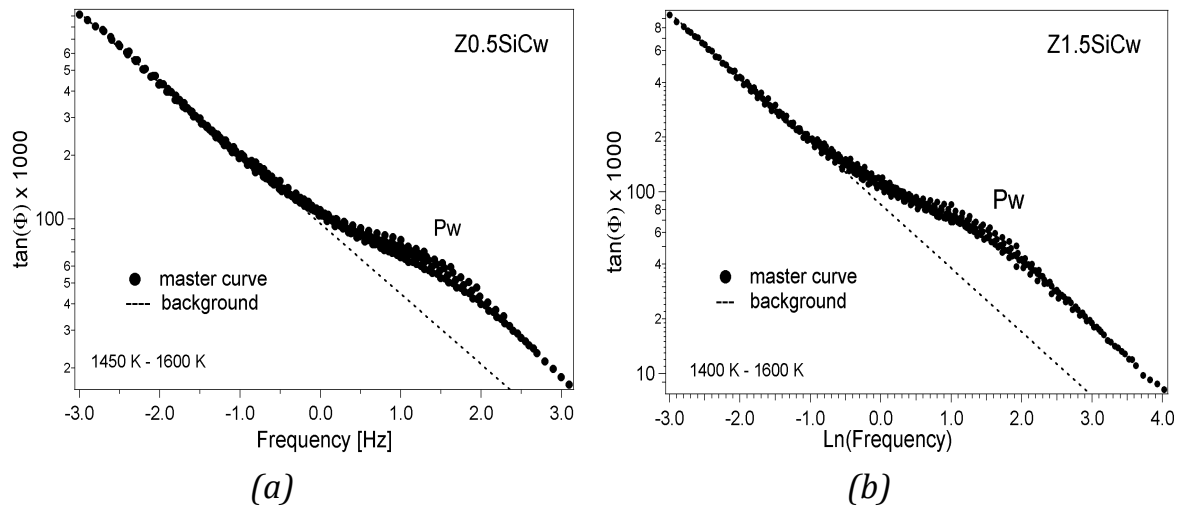
Figure 4.24: Master curves: (a) Z0.5SiCw and (b) Z1.5SiCw. The master curve contains a high-frequency peak that turns into an exponential background.

The activation enthalpy ΔH_{act} and the limit attempt frequency ν_o associated with the underlying mechanism were calculated from the Arrhenius plots by reporting the frequency-shift of the entire spectra as a function of inverse of temperature (Figure 4.25a and Figure 4.25b). The activation enthalpy ΔH_{act} was

found to be 630 kJ/mol for Z0.5 SiCw and 626 kJ/mol for Z1.5SiCw. The limit attempt frequency is $v_o \sim 10^{+20}$ s^{-1} for both SiCw-doped zirconia.
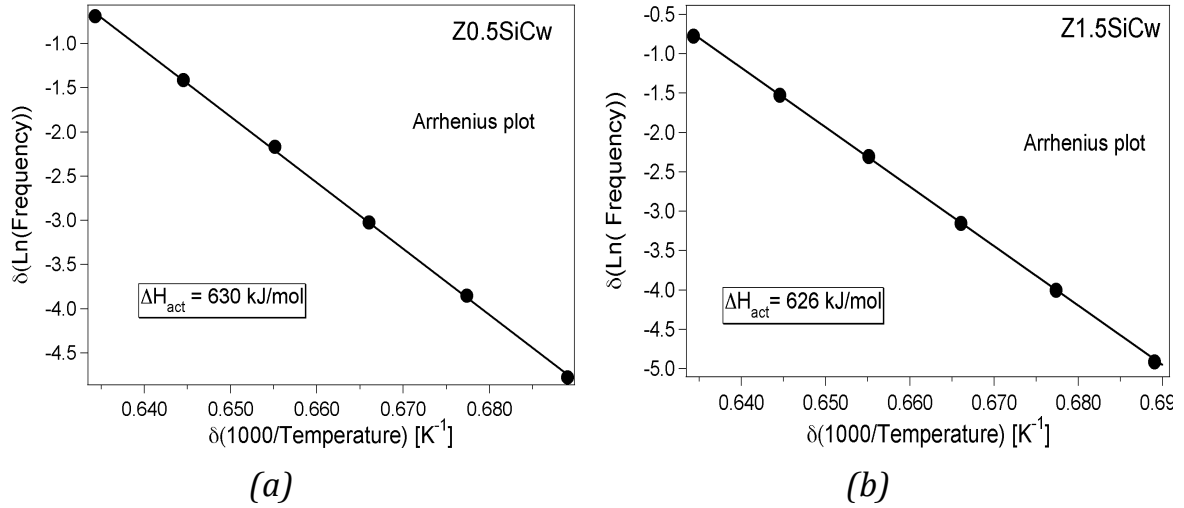
Figure 4.25: Arrhenius plots: (a) Z0.5SiCw and (b) Z1.5SiCw

Creep test

Creep tests (in compression) were performed at 1550 K and under an applied stress of 6 MPa for Z0 and Z1.5SiCw. Figure 4.26 shows the creep strain as measured during creep tests in Z0 and Z1.5 SiCw. Strain in Z1.5SiCw is much smaller than in Z0. This is in agreement with the mechanical spectroscopy results, which indicate a lower level of the damping in the case of SiCw reinforced zirconia composites. A lower level of the exponential background in the damping would mean a better creep resistance.
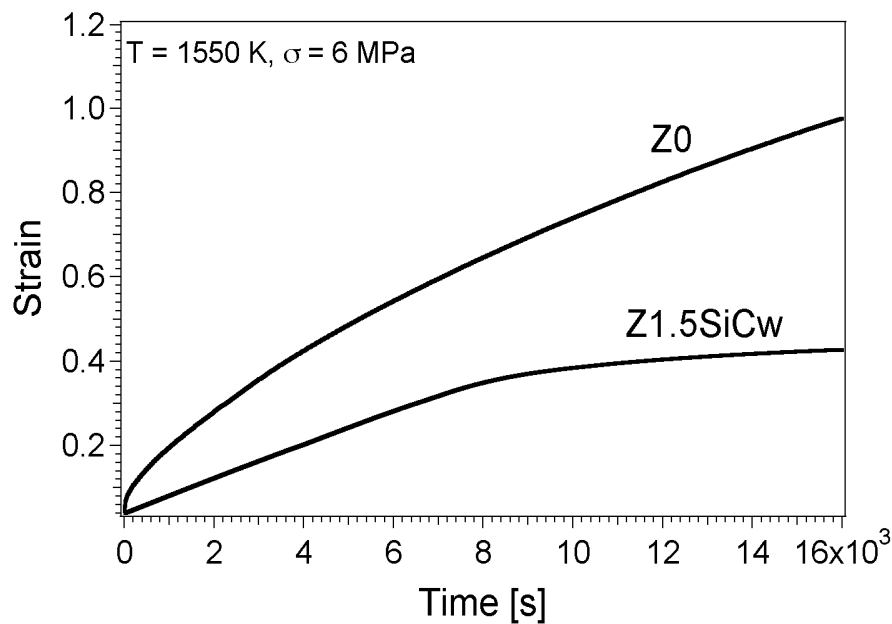
Figure 4.26: Strain-time curves obtained during creep of Z0 and Z1.5SiCw at 1550 K under a compression stress of 6 MPa. Z1.5SiCw creeps slower than Z0.

4.1.8   Addition of silicon carbide particles

Mechanical-loss and dynamic shear modulus spectra of zirconia undoped and doped with silicon carbide particles: 0.5 wt. % (Z0.5SiCp) and 1.5 wt. % (Z1.5SiCp) are shown in Figure 4.27 and Figure 4.28. The samples were investigated under the same experimental conditions: 1 Hz and 1 K/min and 7 MPa. The average grain size is about 0.30 μm for all samples.

The isochronal-mechanical loss spectrum of Z1.5SiCp (Figure 4.27) is composed of an small peak P1 between 1300 K - 1450 K and a second peak P2 situtuated at higher temperatue (Tp = 1515 K). In Z0.5SiCp, P1 is present on the mechanical loss curve between 1330 K - 1500 K. Above 1500 K, P1 transforms into an exponential background that lays over Z0 one. Neither the peak P2 nor the inflection P1 appear on Z0 curve.
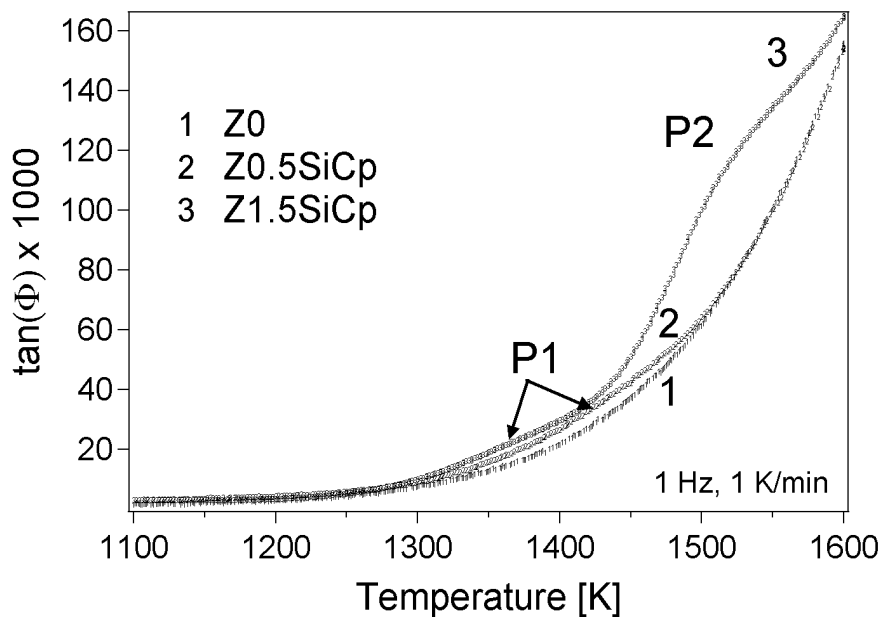
Figure 4.27: Mechanical-loss measurements performed as a function of temperature in Z0, Z0.5SiCp and Z1.5SiCp samples.

The dynamic shear modulus is higher in both SiCp composites with respect to Z0 over all investigated temperature range (Figure 4.22). The decrease of the shear modulus when temperature is increased starts at 1300 K in Z0, while in the Z0.5SiCp at about 1450 K and in the Z1.5SiCp at about 1500 K.
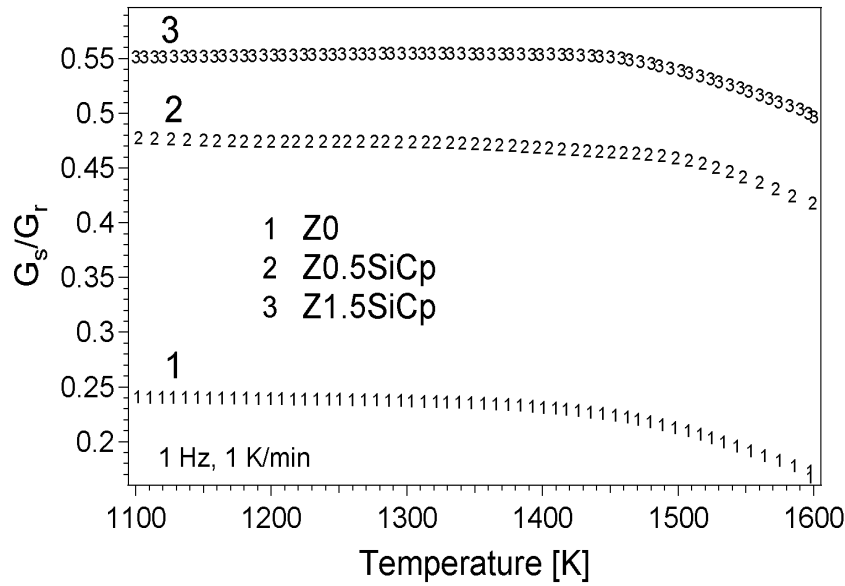
Figure 4.28: Dynamic shear modulus measurements performed as a function of temperature in Z0, Z0.5SiCp and Z1.5SiCp samples.

The isothermal-mechanical loss spectra performed in Z0.5SiCp and in Z1.5SiCp samples are shown in Figure 4.29a and in Figure 4.29b, respectively. The curves are displaced towards higher frequencies with an increase of temperature.

(a)

(b)
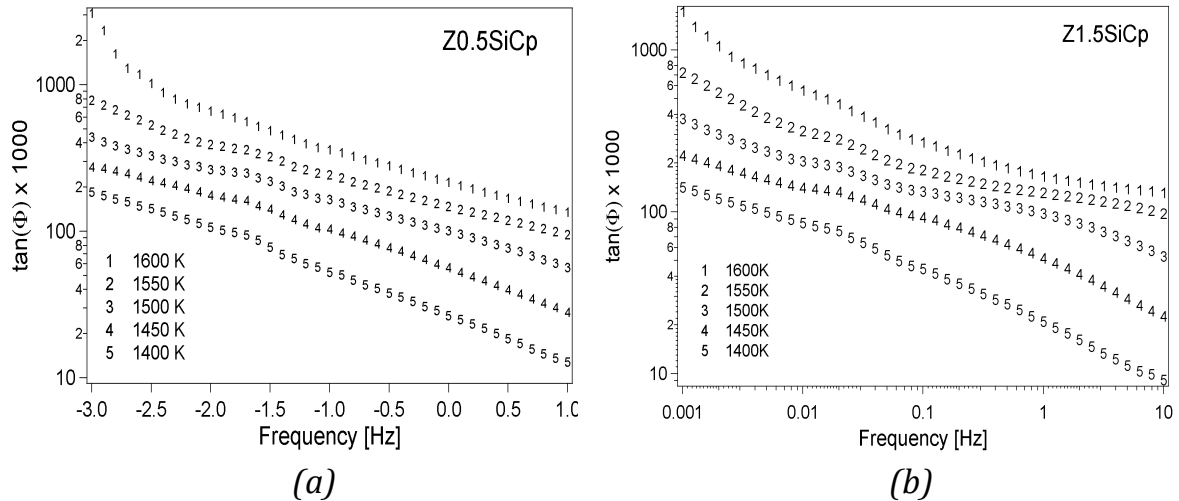
Figure 4.29: Isothermal spectra of Z0.5SiCp and Z1.5SiCp sample. The curves are displaced towards lower frequencies, when the temperature is decreased.

The master-curve spectrum presented in Figure 4.30a and Figure 4.30b contains a dissipation peak denoted Pp. The Pp peak is not preeminently distinct in the Z0.5SiCp sample (Figure 4.30a). The peak Pp is well resolved in the Z1.5SiCp and it is shifted towards higher frequency in Z1.5SiCp (Figure 4.30b).
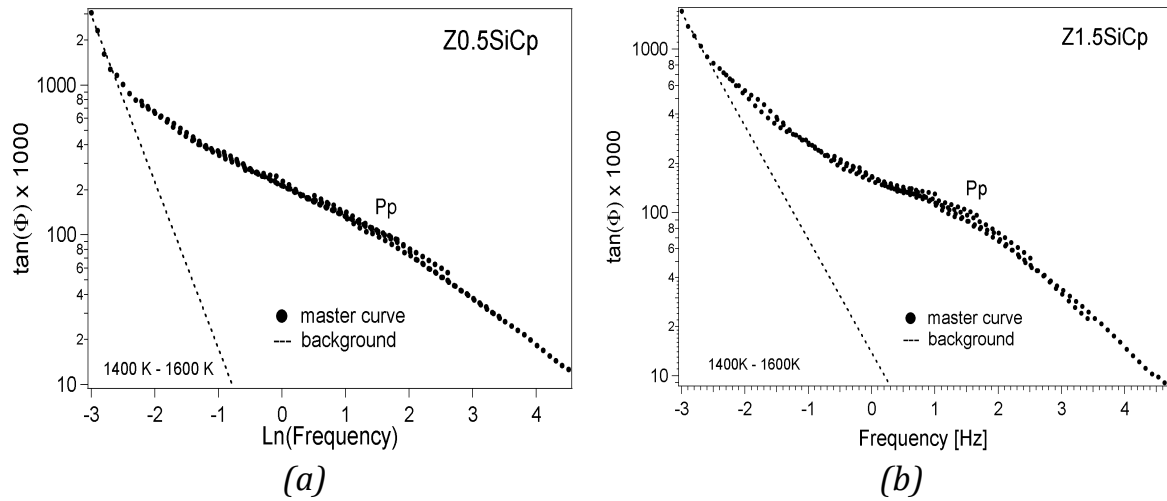
Figure 4.30: Master curves: (a) Z0.5SiCp and (b) Z1.5SiCp. A high-frequency peak followed by an exponential background in both composites.

The activation enthalpy ΔH_{act} and the limit attempt frequency ν_o were obtained through an Arrhenius plot (Figure 4.31). The activation parameters of Z0.5SiCp were found to be ΔH_{act} = 754 kJ/mol and ν_o = $4 \cdot 10^{+26}$ s^{-1} (Figure 4.31a). For Z1.5SiCp, ΔH_{act} = 828 kJ/mol and ν_o = $3 \cdot 10^{+27}$ s^{-1} (Figure 4.31b).
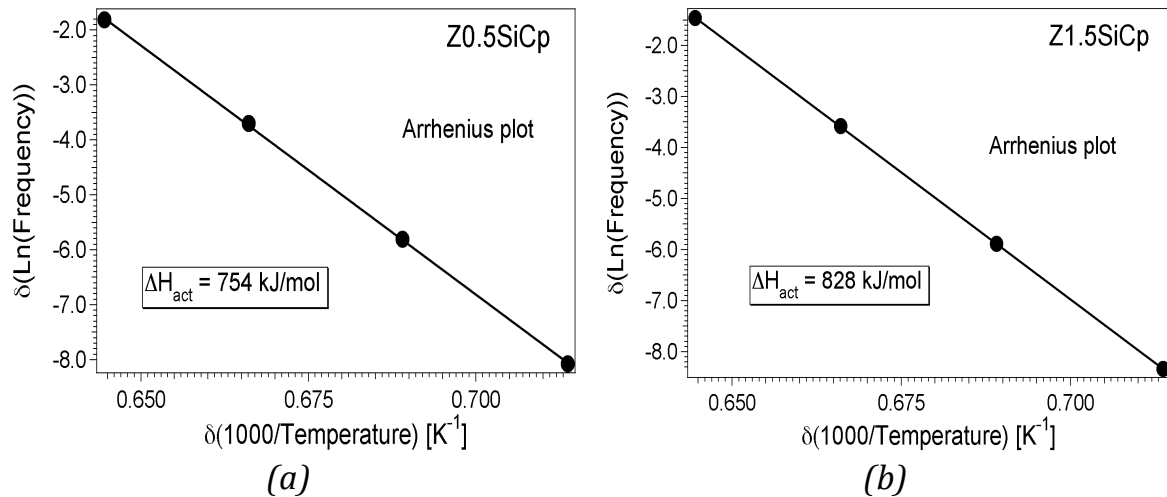
Figure 4.31: Arrhenius plots (a) Z0.5SiCp and (b) Z1.5SiCp after reporting the frequency-shift as inverse of temperature.

4.2 Polycrystalline alumina

4.2.1 Typical spectrum of alumina

Mechanical loss $tan(\Phi)$ and normalized dynamic shear modulus G/G_{600K} spectra measured in pure alumina A0 as a function of temperature for a frequency of 1 Hz, a heating rate of 1 K/min and an applied stress of 7 MPa are presented in Figure 4.32. At low temperatures, the mechanical-loss spectrum exhibits just a plateau of low level, while above 1200 K it increases monotonically. The shear modulus decreases slightly when temperature increases at lower temperature, whereas above 1200 K, the decrease rate is much more important.
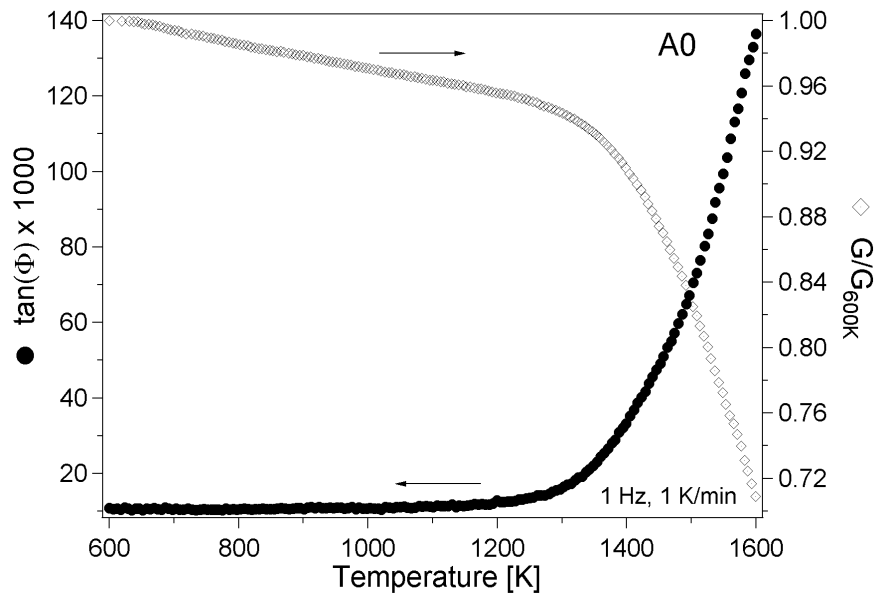
Figure 4.32: Mechanical loss tan(Φ) and normalized shear modulus Gₛ/Gᵣ spectra as a function of temperature. Above 1200 K, tan(Φ) increases exponentially, while Gₛ/Gᵣ decreases.

4.2.2 Analysis of the high-temperature exponential background

High-temperature isothermal measurements were also performed as a function of frequency (10 mHz- 10 Hz) for five different temperatures ranging from 1400 K to 1600 K (Figure 4.33a and Figure 4.33b). The amplitude of the applied stress is 7 MPa.

At first sight, the isothermal-mechanical loss spectra consist mainly in an exponential increase for low frequencies (Figure 4.33a). The curves also exhibit some slope variations, which can be interpreted by one or more peaks supe-

rimposed on the exponential background. Having a look on Figure 4.33 one observes a shift of the curves towards higher frequencies for an increase in temperature. This means that the relaxation phenomena are thermally activated.
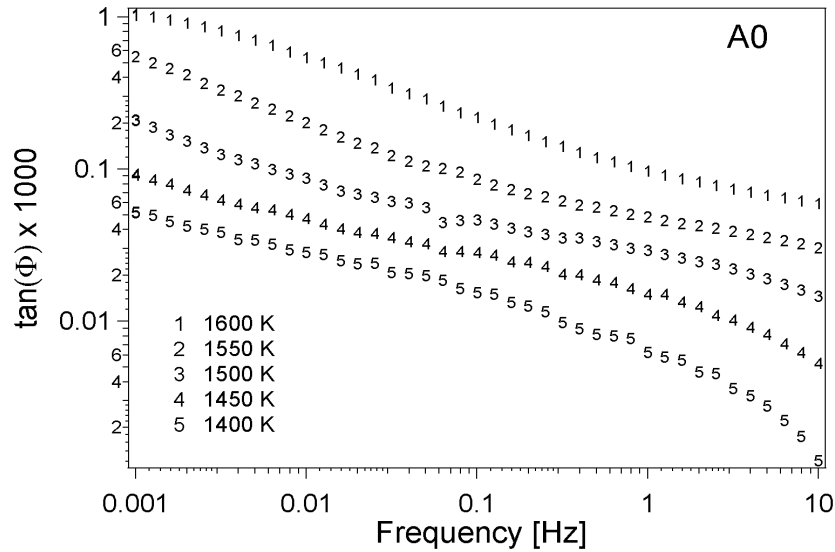
Figure 4.33: Mechanical-loss spectra plotted as a function of frequency.

The master-curve spectrum (Figure 4.34a) appears to be composed of a high-frequency peak, followed by an exponential increase and a second peak at very low frequencies. This generic curve, which contains the same information as all the spectra of Figure 4.33a together, is another indication that the mechanical-loss spectrum of alumina is enriched by more than one peak. From the Arrhenius plot (Figure 4.34b) were deduced the values of the relaxation parameters ΔH_{act} = 840 kJ/mol and τ_0 = 10^{-28} s, respectively. From the Arrhenius plot (Figure 4.34b) were deduced the relaxation parameters ΔH_{act} = 840 kJ/mol and τ_0 = 10^{-28} s, respectively.

(a)   *(b)*
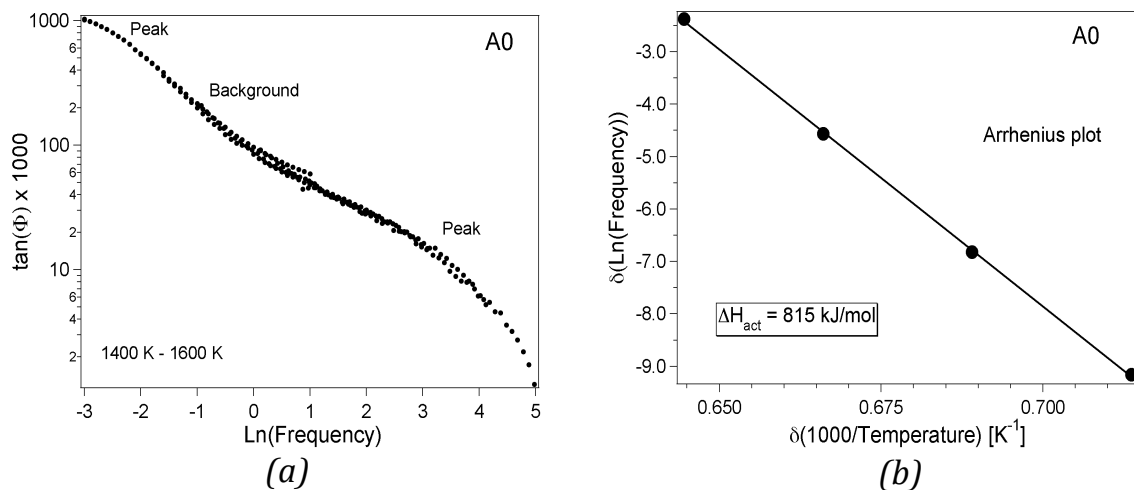
Figure 4.34: (a) Master curve obtained from the frequency-shift method. (b) Arrhenius plot obtained from the shift of the isothermal-mechanical loss spectra.

4.2.3 Annealing effects

The alumina samples was annealed in the pendulum at 1600 K for 1 h and measured in the same experimental conditions as above. In Figure 4.35 are compared the mechanical-loss spectra of annealed and as-sintered samples. The damping level is lower by about 60 % in the annealed specimen.
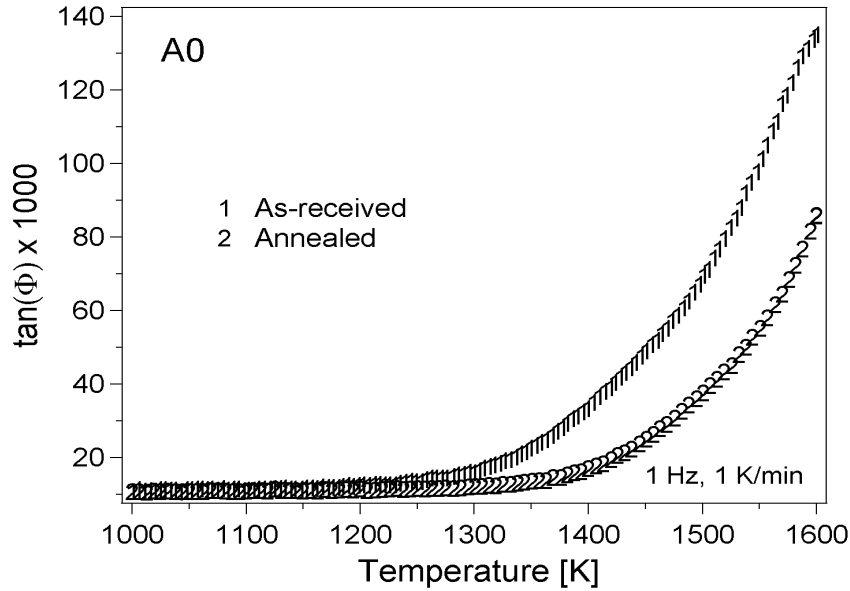
Figure 4.35: Mechanical-loss spectra of A0: annealed (at 1600 K for 1 h) and as-received state. The damping level is lower by 60 % in the annealed specimen.

High-temperature isothermal spectrum of the annealed sample (Figure 4.36a) resemble with Z0 in Figure 4.33a. Similar values of the activation parameters were deduced through an Arrhenius plot, ΔH_{act} = 810 kJ/mol and $\tau_o \approx 10^{-28}$ s (Figure 4.36b).
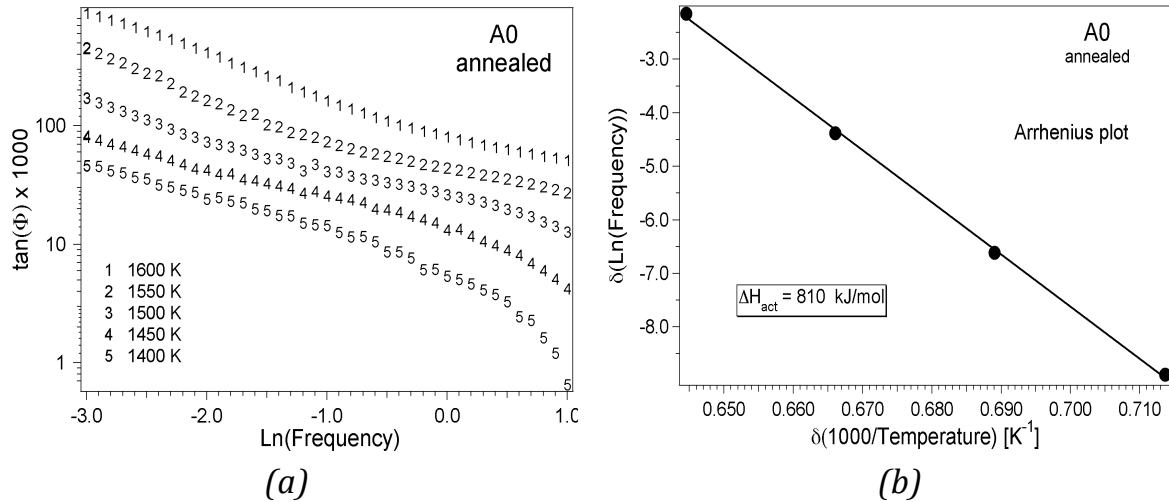
Figure 4.36: (a) Isothermal spectra of A0 sample annealed for 1 h at 1600 K. (b) Arrhenius plot obtained from the shift of the isothermal spectra.

In Figure 4.37 are compared the master-curve spectra of the annealed and as-sintered alumina. The annealed specimen, the mechanical loss is lower in the whole frequency range. As a consequence, the low-frequency peak is less visible on the spectrum of annealed specimen. This behavior could be associated with grain coarsening during annealing [159].
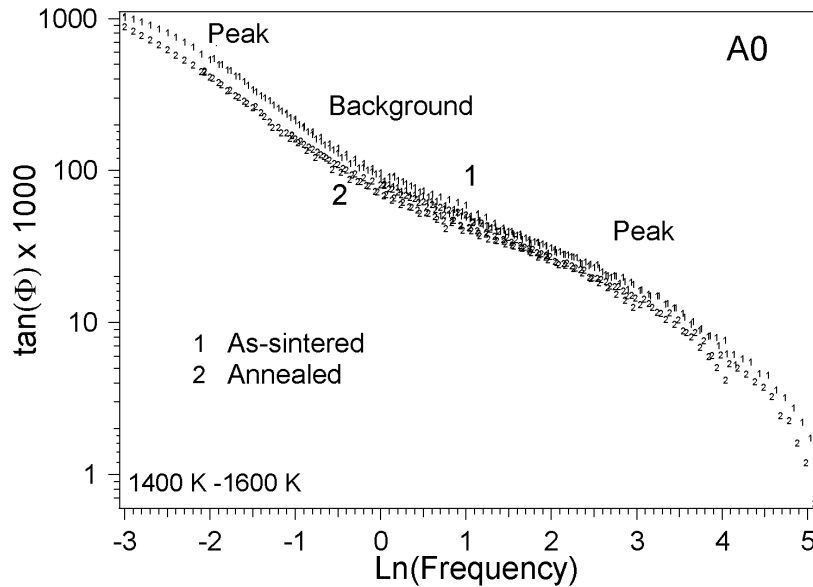
Figure 4.37 Master-curve spectra of the as-received and annealed alumina. Low-frequency peak, background and a high-frequency peak.

4.2.4 Addition of silicon carbide particles

High-temperature isochronal mechanical loss and shear modulus spectra of alumina undoped A0 and doped with silicon carbide particles: 0.5 vol. % SiCp (A05) and 5 vol. % (A5) are reported in Figure 4.38 and Figure 4.39.

The mechanical loss spectra of A0, A05 and A0 presented in Figure 4.38 show just an exponential increase with temperature above 1250 K. The mechanical loss of A0 creeps faster than the one obtained in A05 and A5 composites (Figure 4.38).

At 1600 K, the mechanical loss level is lower by 20 % for A05 and by 40 % for A5 than in A0 (Figure 4.38).
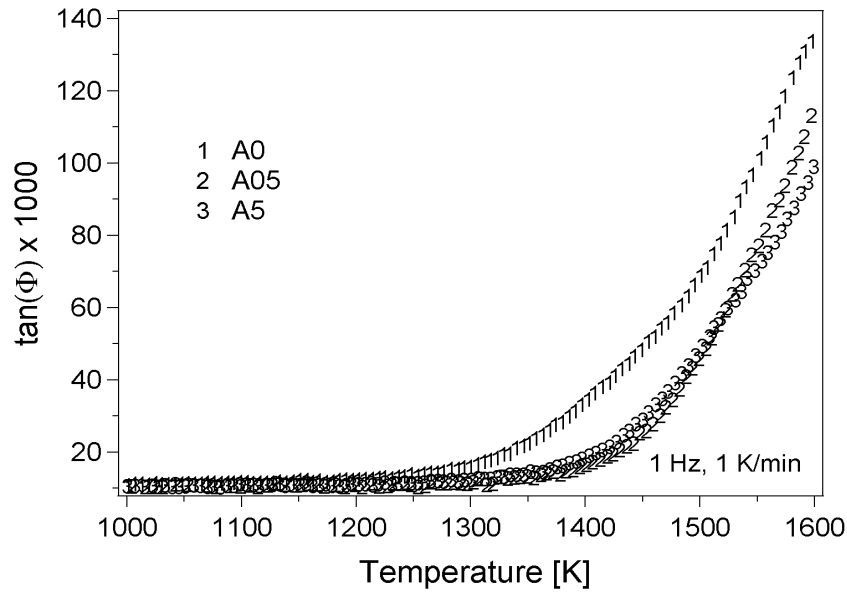
Figure 4.38: Mechanical loss as a function temperature for: A0, A05 and A5.

The anomalous decrease in the shear modulus also appears at higher temperature, but with a decrease rate stronger than in grade A0 (Figure 4.39).
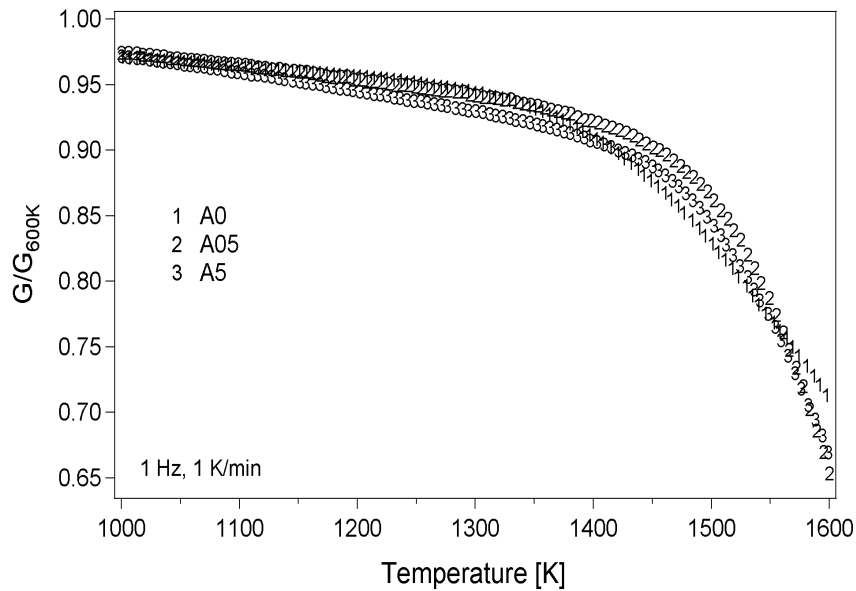
Figure 4.39: Shear modulus as a function temperature for: A0, A05 and A5

By comparison with the pinning effect of nano-sized reinforcements in zirconia, one could conclude that reinforced alumina grades exhibits a better resistance to creep than unreinforced grades.

95

Isothermal measurements were performed between 1400 K and 1600 K in SiC-doped alumina. The isothermal spectra are shifted towards lower frequencies for lower temperatures. So, we are again dealing with thermally activated phenomena.
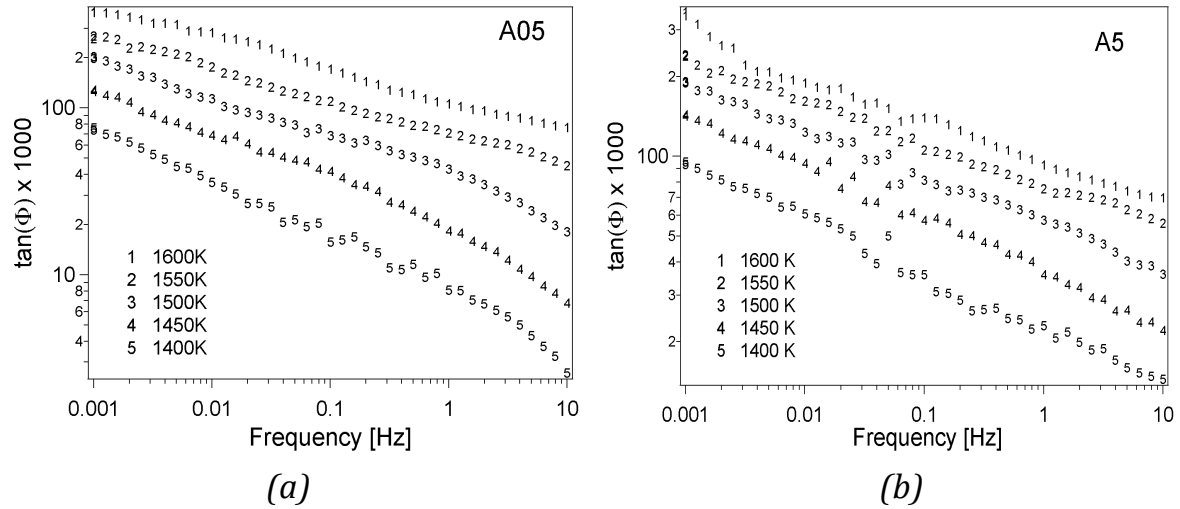
Figure 4.40: Isothermal spectra of: (a) A05 and (b) A5.

Apparent values of the activation parameters, ΔH_{act} and τ_o were calculated through an Arrhenius plot and by reporting the logarithm of the frequency shift as a function of the inverse temperature (Figure 4.40). In the case of A05, one obtains $\Delta H_{act} = 755$ kJ/mol and $\tau_o = 10^{-25}$ s, while for A5, $\Delta H_{act} = 674$ kJ/mol and $\tau_o = 10^{-23}$ s.
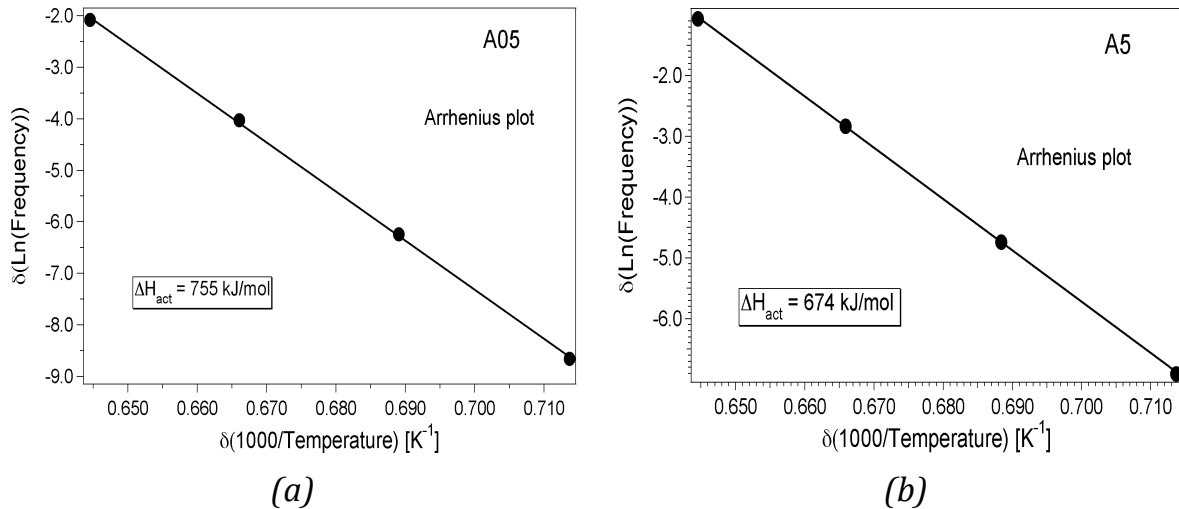
Figure 4.41: Arrhenius plots from the shift of the entire mechanical loss spectra: (a) A05 and (b) A5.

The master curves which were obtained by frequency-shit method are shown in Figure 4.42a and Figure 4.42b. These master curves exhibit a well marked dispersion, which may be due to an evolution of the microstructure with temperature. If the microstructure is not constant, construction of the master curve

is not allowed. In the case where the observed dispersion in Figure 4.42a is not due to microstructure changes, we can admit that the master curve of A05 is composed of a peak, which turns into a background, followed by a low-frequency peak. In the case of A5, the peak is not well resolved from the exponential background (Figure 4.42b).
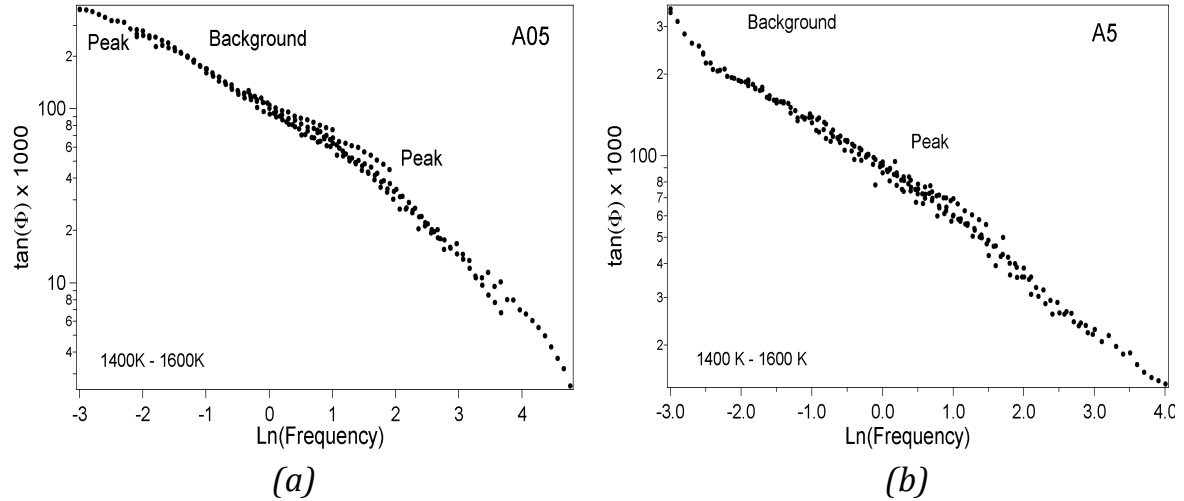
Figure 4.42: Master curves: (a) A05 and (b) A5.

4.3   Summary

The high-temperature mechanical loss spectra of fine-grained ceramics, such as zirconia and alumina, exhibit similar comportments: an exponential increase of the mechanical loss with temperature or when frequency is decreased. Construction of the master spectrum from the isothermal spectra, proves that indeed the mechanical-loss spectrum is composed of one (sometimes two) relaxation peaks, which transforms into an exponential background at low frequency (or high temperature). Transformation from the peak to the exponential background may account for the onset of the creep in the material.

As a matter of fact, by reinforcing the fined-grained ceramics with nano-sized fibers or particles result in a decrease of the high-temperature exponential background. Creep tests in compression have confirmed that this decrease in the exponential background can be associated with a better resistance to creep: creep strain is strongly reduced in the reinforced grades. As the reinforcements were found to be mainly located on the GBs, it is not "a bad idea" to imagine that the reinforcing effect is associated with a GB pinning effect.

A simple theoretical model of GB sliding in the next chapter will have to demonstrate the effect of pinning centers on the mechanical-loss spectrum associated with GB sliding.

Chapter 5

Interpretation and discussion

The high-temperature superplastic deformation of fine-grained ceramics, such as polycrystalline zirconia and alumina, is associated with GB sliding [83, 126, 134, 160]. GB sliding is considered as the fastest step for deformation and it is controlled by diffusion or interface reaction processes (at low stresses) [57, 58, 61, 82, 92, 93].

During mechanical spectroscopy measurements at 1 Hz the conditions are close to primary (transient) creep. Only local motion can take place, the easiest one being the relative sliding of two neighboring grains along their common plane.

5.1   Model of grain boundary sliding

5.1.1   Grain boundary sliding in zirconia

From the point of view of mechanical spectroscopy the high-temperature mechanical loss spectra of polycrystalline ceramics can be interpreted by a theoretical model of GB sliding [15]. In this model neighboring hexagonal grains, which are separated by an intergranular-viscous interface, suffer relative sliding under the applied stress (cf. §2.3.3). In the case of "clean" GBs, sliding would be achieved by GB-dislocation motion (cf. §2.3.2). GB sliding takes place until the applied stress is completely sustained by the triple grain junctions (Figure 5.1) or other asperities.

Coming back to the Lakki's model (§2.3.3), the motion equation of a grain of diameter d submitted to a shear stress σ, which acts on the grain surface of d^2 (Figure 5.1), is given by the Newton's equation with negligible inertia ($\sum \vec{F} = 0$):

$$\sigma\, d^2 = \frac{\eta}{\delta} d^2 \dot{x} + kx \qquad\qquad (5.1)$$

By dividing all the terms by d² one gets equation (2.24):

$$\sigma = \frac{\eta}{\delta}\,\dot{x} + Kx \tag{5.1'}$$

where η is the viscosity of the intergranular layer, δ its thickness and Kx the restoring force per unit area ($K = k/d^2$) due to triple junctions. Hence, in this sliding process two forces are opposed to the applied shear stress: the dragging force (first term in equation (5.1')) originating from the viscosity of the amorphous layer and the restoring force (second term in equation (5.1')) corresponding to the elasticity of the adjacent grains, which limit the sliding at the triple junctions.
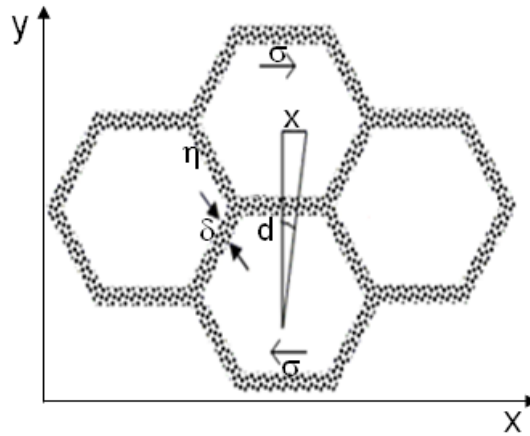
Figure 5.1: Lakki's model for relative sliding of two hexagonal grains separated by a viscous film under an applied stress σ [15].

The solution of equation (5.1') for an applied cyclic stress $\sigma = \sigma_o cos(\omega t)$ gives the displacement x occurring during mechanical-loss measurements.

$$x = \frac{\sigma}{K} \cdot \frac{1}{1+i\omega\tau}$$

with $\tau = \eta/\delta\,K$ gives the relaxation time.

The total strain is composed of the elastic strain and the anelastic strain and it is given by the following equation:

$$\varepsilon = \varepsilon_{el} + \varepsilon_{an} = \frac{\sigma}{G} + \frac{x}{d} = \frac{\sigma}{G} + \frac{\sigma}{d\,K}\frac{1}{1+i\omega\tau} \tag{5.2}$$

where G is the shear modulus.

The mechanical loss $tan(\Phi)$ is given by the phase lag between stress and strain, i.e. also given by the ratio of the imaginary part over the real part of strain.

$$tan(\Phi) = \frac{G}{Kd}\left(\frac{\omega\tau}{1+\omega^2\tau^2}\right) \qquad (5.3)$$

The mechanical loss in equation (5.3) has the form of a Debye peak (peak 1 in Figure 5.2), the maximum of which is given by $\omega\tau = 1$ or also:

$$\omega\frac{1}{K}\frac{\eta_o}{\delta}\,exp\left(\frac{H}{RT_p}\right) = 1 \qquad (5.4)$$

where ω is the frequency, H the activation enthalpy, T_p the temperature of the peak, R the gas constant.

For this plot the following values have been used:

G = 80 MPa
d = 0.30 μm
ω = 1 Hz
τ_o = 2·10⁻²⁰s
H = 560 kJ/mol
K = 1
K_o = 3·10⁻¹⁹
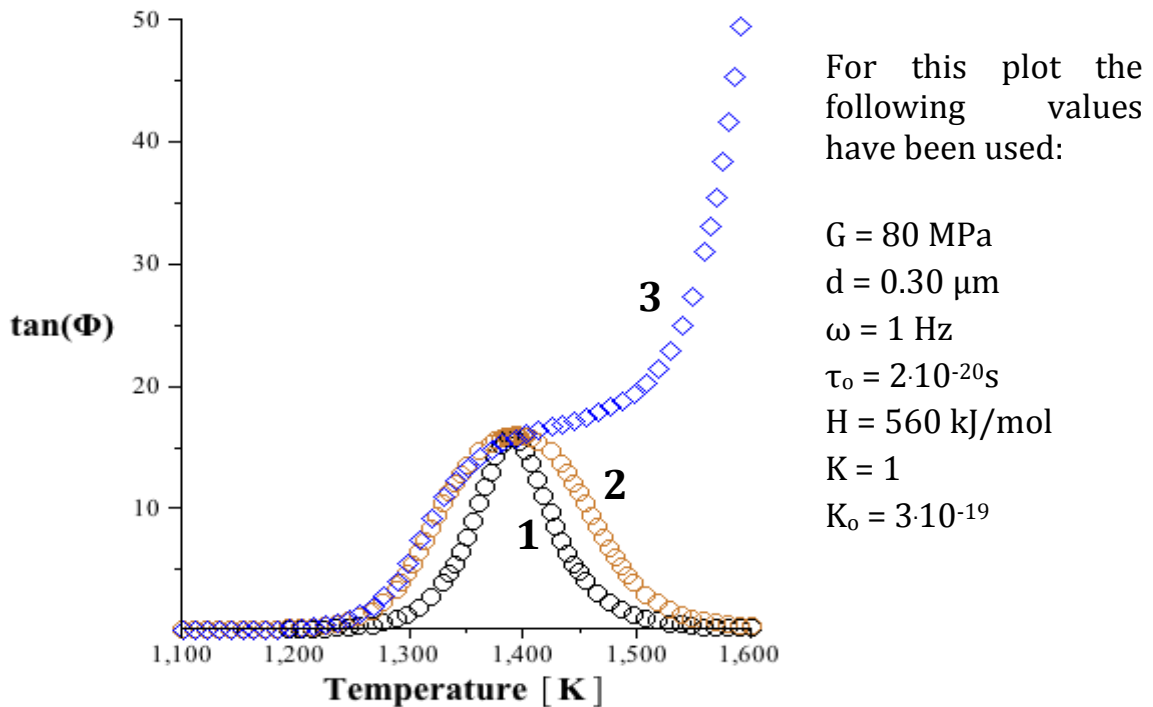
Figure 5.2: Theoretical-mechanical loss spectrum: **1** *K(T) = const.- Debye peak according to equation (5.3),* **2** *K(T) = const. - Broader Debye peak according to equation (5.3),* **3** *K(T) vanishes - Exponential increase of the mechanical loss.*

In real materials, there is a distribution on η and δ, this means a distribution on the activation enthalpy leading to an enlarged Debye peak (peak 2 in Figure 5.2). At higher temperatures than T_p, if the triple junctions can be overcome, the broader peak transforms into an exponential increase because the restoring force decreases strongly. Assuming that the weakening of the pinning triple

junctions is due to diffusion (interface reaction, see §1.2.4), then we can write the following equation for the restoring coefficient K:

$$K = K_0 exp\left(\frac{H}{RT}\right) \qquad (5.5)$$

with H is the enthalpy for diffusion in the GBs or in the intergranular-glassy phase.

The mechanical loss becomes:

$$tan(\Phi) = \frac{G}{dK_0} exp\left(\frac{H}{RT}\right)\left(\frac{\omega\tau}{1+\omega^2\tau^2}\right) \qquad (5.6)$$

and one observes that the peak transforms into an exponential background at higher temperature (in Figure 5.2, curve 3).

5.1.2 Limitation of the grain-boundary sliding by introducing nano-sized pinners

According to GB sliding model (Figure 5.1), when GBs are not limited by obstacles (triple junctions, GB asperities or other defects), creep occur and the exponential increase with temperature is observed in the isochronal-mechanical loss spectrum (Figure 5.2). One way to limit the GB sliding in ceramics is to add extra pinners at their triple points (Figure 5.3).
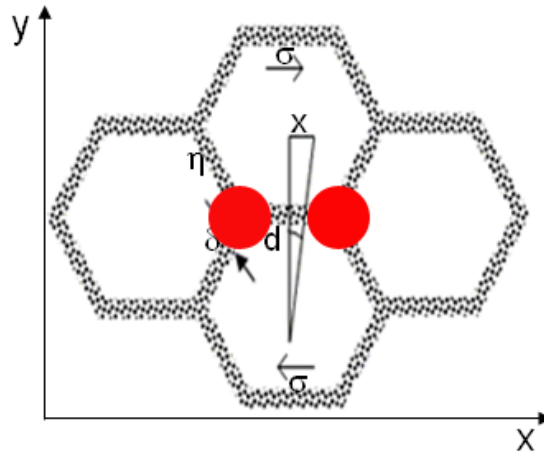
Figure 5.3: Hexagonal grains separated by a viscous film and pinned at the triple junctions by nano-sized pinners.

Addition of pinners at the triple junctions will result in a decrease in the high-temperature exponential background. Therefore, the pinners will modify

K as follows:

$$K = K_1 K_0 exp\left(\frac{H}{RT}\right)\tag{5.7}$$

Thus, the mechanical loss becomes:

$$tan(\Phi) = \frac{G}{dK_1K_o} exp\left(\frac{H}{RT}\right)\left(\frac{\omega\tau}{1+\omega^2\tau^2}\right)\tag{5.8}$$

and the exponential background is decreased in Figure 5.4 (curve 3).

For this plot the following values have been used:

G = 80 MPa

d = 0.30 μm

ω = 1 Hz

τ_0 = $2 \cdot 10^{-20}$s

H = 560 kJ/mol

K = 1

K_o = $3 \cdot 10^{-19}$

K_1 = $2 \cdot 10^{-2}$
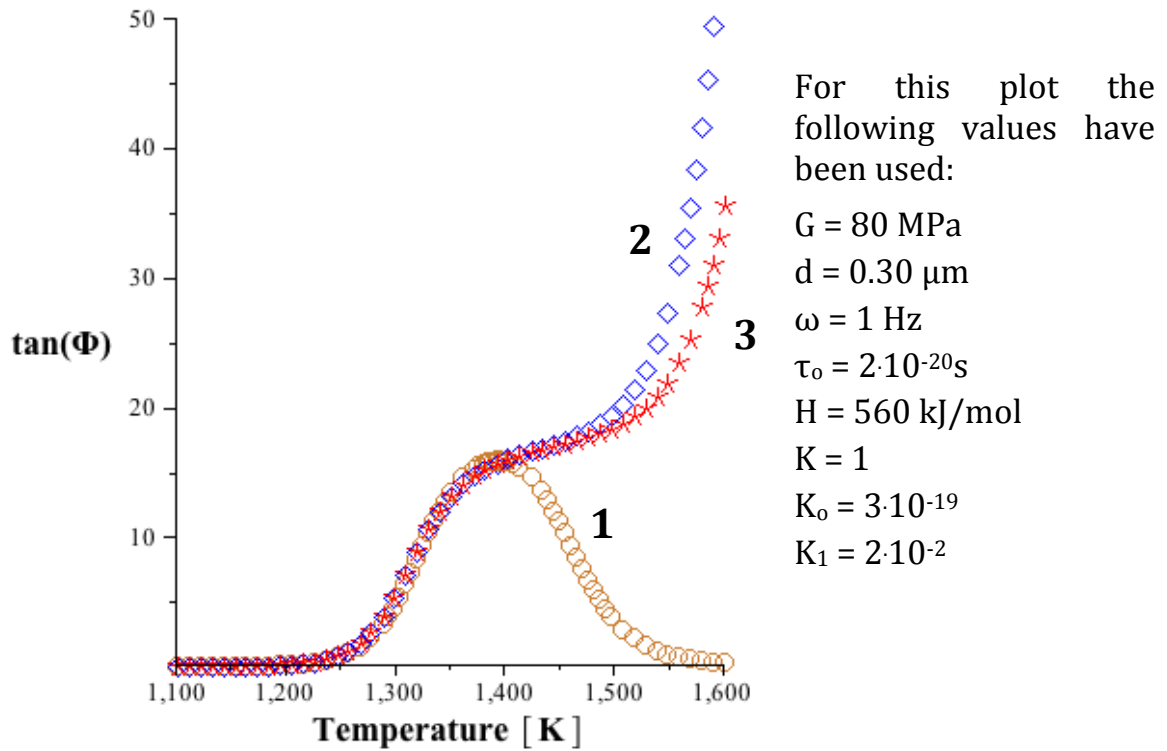
Figure 5.4: Theoretical-mechanical loss spectrum according to GB sliding model:
1 *K(T) = const. - Broader Debye peak,* **2** *K(T) vanishes - Exponential increase of the mechanical loss,* **3** *K(T) strong enough due to pinners on the GBs - leads to a decrease of the exponential background.*

5.1.3   Discussion of the obtained results in zirconia and alumina

At high temperatures the mechanical-loss spectra of pure zirconia and alumina look very similar. Above 1200 K, the isochronal spectrum consists just of an exponential increase of damping accompanied by a decrease of the shear modulus (Figure 4.1 and Figure 4.32). Also, the isothermal spectra look similar

(Figure 4.3 and Figure 4.33a). The origin of the damping in zirconia is well-accounted with the theoretical model of GB sliding with grains separated by an intergranular layer. The GB sliding is limited in the peak domain by a restoring force. When the restoring force is overcome the sliding is not anymore limited and the mechanical loss increases exponentially. In the case of zirconia, the regular shape of the grains does not provide strong pinning points at the triple junctions. This means that the GB sliding is not anymore limited and the creep takes place.

In order to limit GB sliding the microstructure of zirconia and alumina has to be modified. For this reason their GBs have been reinforced with some nano-sized pinners. According to the above model of GB sliding, when pinners are present at the GBs the level of the mechanical-loss spectrum should decrease.

We have seen in Chapter 4 that through insertion of CNTs in zirconia the mechanical-loss level decreases with respect to the level measured in pure zirconia (Figure 4.14). TEM image (Figure 3.7) shows that the CNTs are present at the triple junctions. In the case of SiCw the mechanical-loss level is also decreased (Figure 4.21). The TEM image (Figure 3.9) shows that SiCw can be situated within the zirconia matrix and also at the GBs. On the contrary, the level of the mechanical loss in Z1.5SiCp is higher than in zirconia, while in Z0.5SiCp have the same level at 1600 K (Figure 4.27). The TEM image (Figure 3.10) shows that SiCp are immersed in a SiO_2 phase at the triple junction. Addition of SiCp to alumina leads to a decrease of the damping level. It was found by TEM that SiCp are mostly situated along GBs.

The high-temperature mechanical loss of zirconia and alumina can be well interpreted by a GBs model. However, as values of the activation parameters, especially the activation enthalpy, are surprisingly higher than what is expected for diffusion in GBs. Indeed, these values must be lower than for diffusion in volume and they are higher. We conclude that the values are apparent and must be corrected.

5.2   Analysis of the activation parameters

5.2.1   Methods of correcting the activation enthalpy

The high-temperature mechanical loss spectra of fine-grained ceramics contain more or less resolved peaks with respect to exponential increase (Chapter 4). Considering ceramics as two-component materials – grains and GBs –the origin of the damping can be established by comparing the spectra of the components. Nevertheless, to find a good interpretation of the dissipative mechanism, the activation parameters have to be analyzed.

In this study, it was found that the mechanical-loss spectra are thermally activated. The activation parameters, enthalpy ΔH_{act} and limit attempt frequency ν_o, obtained from the Arrhenius plots are apparent. Apparent values can be obtained when there is a change in the microstructure. If the microstructure evolves as a function of temperature leading to a decrease of the energy barrier, then higher values of the activation parameters will be obtained. Therefore, they must be corrected. Two methods can be used here to correct the apparent values of the activation parameters:

    a) Wert-Marx method [161]
    b) Schoeck [130]-Escaig [162] method

a) Wert-Marx method [161]

A first rough correction, which is indicative of a range of reasonable values for ΔH_{act}, may be obtained by Wert-Marx method [161]. The method refers to the fact that, for a given measuring frequency ν_m, the activation enthalpy level is determined by the peak temperature T_p, that is:

$$\Delta H = RT_p ln\left(\frac{\nu_D}{\nu_m}\right) \qquad (5.9)$$

where ν_D is the Debye frequency ($\sim 10^{13}$ s^{-1}) and R the gas constant.

When the method is applied on the isothermal spectrum, the activation enthalpy level can be determined from the peak frequency ν_p for a given measuring temperature T_m. The activation enthalpy will be given by:

$$\Delta H = RT_m ln\left(\frac{\nu_D}{\nu_p}\right) \qquad (5.10)$$

b) Schoeck [130] - Escaig [162] method

Another method was proposed by Schoeck [130] and then by Escaig [162]. First it has to be pointed out that the Arrhenius plots yield the activation enthalpy ΔH_{act} and not the activation free enthalpy ΔG, which characterizes the obstacle of a thermally activated phenomenon. If ΔG decreases rapidly when temperature increases, then a high value of ΔH_{act} is obtained by means of Arrhenius plot. In other words, the decrease in the energy barrier yields to an apparent ΔH_{act}. Escaig [162] considered that ΔG depends on temperature via elastic constants, for instance shear modulus denoted here μ, according to equation:

$$\Delta G = \frac{\Delta H + [(T/\mu)(d\mu/dT)]\sigma V}{1 - [(T/\mu)(d\mu/dT)]} \qquad (5.11)$$

where σ is the applied stress and V the activation volume. In mechanical spectroscopy measurements, the product "σV" is very small and can be neglected in equation (5.11). From the high-temperature dependence of the shear modulus and by using the equation (5.11), it is possible to correct the apparent values of the activation enthalpy and to calculate ν_o.

5.2.2   Application to zirconia and its composites

In pure zirconia ΔH_{act} and ν_o were found, from the Arrhenius plot (Figure 4.6), to be 679 kJ/mol and $2 \cdot 10^{22}$ s^{-1}, respectively (Table 5.1). ΔH_{act} is higher than the one obtained by creep test 580 kJ/mol [15, 82]. In CNTs- or SiCw-zirconia composites and in ZE ΔH_{act} values are smaller in than in Z0 (Table 5.1). Whereas in SiCp-zirconia composites ΔH_{act} values are higher than in Z0 (Table 5.1). In fact, we would expect that in zirconia composites ΔH_{act} to be higher than in Z0. Also, ν_o is too high with respect to Debye's frequency ($\sim 10^{13}$ s^{-1}). This indicates that the activation parameters are apparent.

Sample	ΔH_{act} [kJ/mol]	ν_o [s^{-1}]
Z0	679	$2 \cdot 10^{22}$
ZE	617	$4 \cdot 10^{20}$
Z0.5CNTs	643	$1 \cdot 10^{21}$
Z1.5CNTs	636	$5 \cdot 10^{20}$
Z0.5SiCw	630	$2 \cdot 10^{20}$
Z1.5SiCw	626	$1 \cdot 10^{20}$
Z0.5SiCp	754	$4 \cdot 10^{26}$
Z1.5SiCp	828	$3 \cdot 10^{27}$

Table 5.1: The activation enthalpy ΔH_{act} and the limit attempt frequency ν_o for zirconia and its composites.

Wert-Marx method can be applied on both isochronal and isothermal measurements. Because in pure zirconia one does not observe a peak in isochronal spectrum, the Wert-Marx correction method will be applied on the isochronal spectrum in all zirconia grades. For example, the peak frequency ν_p can be obtained from the isothermal spectrum measured at Tm = 1600 K, i.e. in pure zirconia (Figure 4.3). By replacing the values of T_m = 1600 K and the peak position 0.316 Hz on equation (5.10) we get ΔH = 414 kJ/mol. In Table 5.2, the corrected activation enthalpies ΔH as predicted by equation (5.10), have been added for all investigated zirconia grades .

Another method which can be used for correction of the activation parameters is Schoeck-Escaig method. From the temperature dependence of the shear modulus in isochronal spectrum in Figure 4.11, Figure 4.15, Figure 4.22, and

Figure 4.28, also by using the equation (5.11), it is possible to correct the activation enthalpies from Table 5.1 and to calculate ν_{corr}. The results are listed in the last two columns of Table 5.2.

Sample	T_m [K]	ν_p [s^{-1}]	[a]ΔH [kJ/mol]	[b]ΔG [kJ/mol]	ν_{corr} [s^{-1}]
Z0	1600	0.316	414	262	$3 \cdot 10^8$
ZE	1600	0.019	450	220	$1 \cdot 10^8$
Z0.5CNTs	1600	0.061	435	370	$2 \cdot 10^{12}$
Z1.5CNTs	1600	0.031	445	397	$2 \cdot 10^{12}$
Z0.5SiCw	1600	0.025	447	184	$2 \cdot 10^6$
Z1.5SiCw	1600	0.019	450	250	$5 \cdot 10^7$
Z0.5SiCp	1600	0.012	457	286	$5 \cdot 10^{10}$
Z1.5SiCp	1600	0.019	450	408	$2 \cdot 10^{13}$

Table 5.2: Corrected values: [a]ΔH corrected by Wert-Marx method [161] and [b]ΔG corrected by Schoeck [130] - Escaig method [162].

The results bring reasonable values of the limit attempt frequency. However, the results obtained by equation (5.11) may be overestimated because it is difficult to distinguish the decrease in the shear modulus because of the microstructural evolution from the modulus defect due to anelastic deformation itself.

5.2.3   Application to alumina and its composites

Decrease in the high-temperature exponential background by addition of SiCp particles may be associated with a limitation of the GB sliding. However, while qualitatively the introduction of SiCp produces a hardening of the material (evidenced by the decrease in the mechanical loss and the increase in the shear modulus Figure 4.38 and Figure 4.39); the activation enthalpy values measured from the Arrhenius plots are somewhat contradictory as we can see in Table 5.3.

Sample	ΔH_{act} [kJ/mol]	τ_o [s]
A0	840	10^{-28}
A05	755	10^{-25}
A5	674	10^{-23}

Table 5.3: The activation enthalpy ΔH_{act} and the relaxation time τ_o for alumina and SiCp-alumina composites.

As well ΔH_{act} of pure alumina (A0) is much higher than the diffusion energy and the limit relaxation time is too low in comparison with the inverse Debye fre-

quency ($\sim 10^{-13}$ s). In fact, we would expect the highest activation energy for the slowest process and therefore for the most refractory material. The values of ΔH_{act} obtained through Arrhenius's plots Figure 4.34, Figure 4.41a and Figure 4.41b are apparent values. This is particularly evident if we consider the values of the limit relaxation time τ_o: $10^{-28}s$ - $10^{-23}s$, which are much lower than the limit value associated with the usual inverse of the Debye frequency.

The correction of the apparent ΔH_{act} obtained from isothermal spectrum at 1600 K in Figure 4.33a, Figure 4.40a and Figure 4.40b and by using the equation (5.10) are given Table 5.4. The corrected ΔH shows similar values, which indicate the same physical processes.

Sample	T_m [K]	ν_p [s^{-1}]	(a)ΔH [kJ/mol]	(b)ΔG [kJ/mol]	ν_{corr} [s^{-1}]
A0	1600	0.001	490	525	$2 \cdot 10^{18}$
A05	1600	0.019	450	515	$7 \cdot 10^{18}$
A5	1600	0.015	454	540	$2 \cdot 10^{19}$

Table 5.4: Corrected values: (a)ΔH_{act} corrected by Wert-Marx method [161] and (b)ΔG corrected by Schoeck [130] or Escaig method [162].

From the temperature dependence of the shear modulus (Figure 4.39) and by using the equation (5.11) ΔG in alumina and its composites were calculated. The calculated values of ΔG and ν_{corr} are given in Table 5.4.

Calculated ΔG for undoped and SiCp-doped alumina (Table 5.4) seems to be reasonable, especially for A0, ΔG is comparable to the ones deduced from creep data [49, 163]. The calculated limit attempt frequency is much higher than Debye's frequency.

5.3   General discussion

5.3.1   Mechanical loss due to grain boundary sliding

Result analysis has shown that the high-temperature mechanical loss behavior of ceramics can be interpreted by a theoretical model of GB sliding. On the microstructural level, the spectrum of zirconia has been interpreted by the relative sliding of equiaxed grains lubricated by an intergranular-glassy phase. In the isochronal spectrum of pure zirconia (Figure 5.5), no well-resolved peak is observed, but only a damping exponential increase at high temperature (between 1200 K – 1600 K). An exponential increase in the mechanical loss would result from GB sliding, which is not limited by strong obstacles (no restoring force, see §5.1.1). Such a behavior may be interpreted as a poor creep resis-

tance of the ceramic. As a matter of fact, the shear modulus of ZE decreases faster at high temperature than the one of pure zirconia (Figure 4.11). This behavior is associated with the presence of SiO_2 in zirconia. Daraktchiev [126] has shown that 5 wt. % SiO_2 doped zirconia enhances the sliding in such a way that as a result the mechanical loss is increased by a factor of 2 with respect to pure zirconia. Moreover a peak has been observed at 1400 K attributed to anelastic relaxation within SiO_2 glassy pockets. It is then easy to conclude that GB sliding is enhanced by the presence of an intergranular-amorphous layer between the zirconia grains. GB sliding will be easier for a higher amount of amorphous SiO_2 between the grains and/or at multiple junctions.
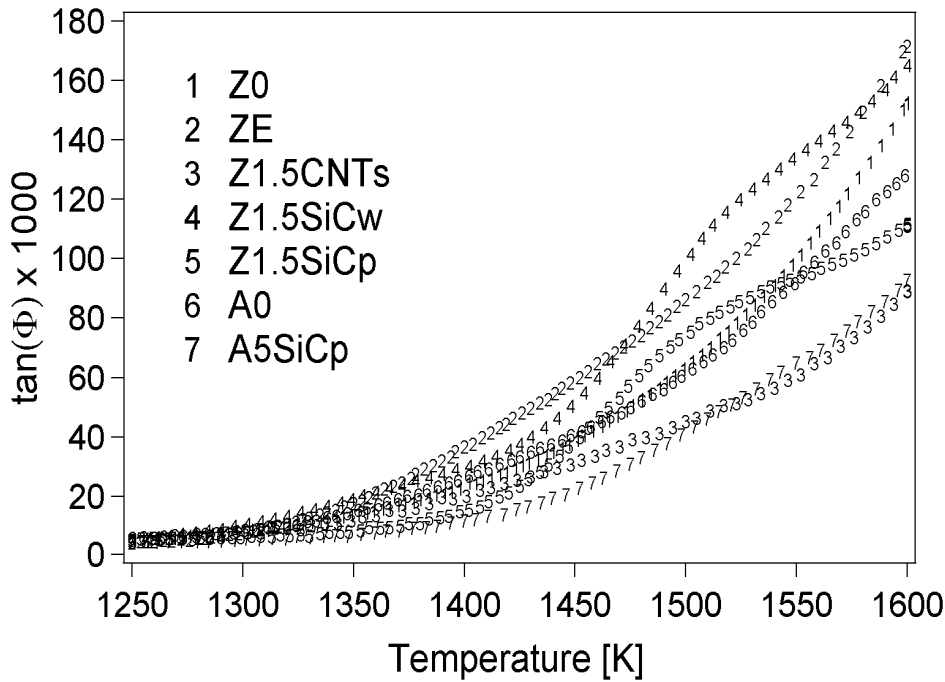
Figure 5.5: Mechanical-loss spectra of zirconia, alumina and their composites.

Another important parameter that influences the energy dissipation in zirconia and plays an important role on the GB sliding mechanism is the grain size. When the grain size is smaller the mechanical-loss level is higher (Figure 4.8 and Figure 4.9). For the same level of the applied stress the small grains slide faster than bigger grains. The low stress creep regime in zirconia has been interpreted as controlled by Coble GB diffusion process [67]. The dependence of the mechanical loss on the grain size yields a grain size parameter p = 1 in zirconia ([132]), which is in good agreement with GB sliding model, but not with Coble creep (p = 3). Lakki et al. [15] have found in zirconia that the dependence of the mechanical loss on the grain size leads to a value of $p \cong 1$.

The low-frequency exponential background as it appears in the isothermal measurements in Figure 4.7 allows us to study the mechanism, which controls creep in the low stress regime. The exponential background exhibits stress de-

pendence with a threshold stress. The threshold effect is similar to the one reported by Jiménez-Melendo and Domínguez-Rodríguez [59] for creep test. Of course, the level of the threshold stress observed in pure zirconia is smaller than 4.9 MPa deduced from creep test [59]. The existence of a threshold stress on zirconia is associated with the transition from local sliding (peak) and extensive sliding at the appearance of creep (exponential background). A relaxation peak is representative for anelastic deformation, in which the restoring force limits the strain. In the case of zirconia and alumina, the regular shape of the grains does not provide strong pinning centers at the multiple junctions. As a consequence the mechanical-loss peak due to GB sliding is not well resolved with respect to the exponential background. And, as already said, the exponential background is the signature of creep. Transition from the peak to the exponential background would be then the signature of the accommodation mechanism (interface reaction), which allows extensive GB sliding. In the present case, the interface reaction, which allows GB sliding over the triple junctions, is believed to be the "solution-diffusion-precipitation" mechanism. In this case the triple points weaken by diffusion process and this justifies our phenomenological expression for the restoring force (K) weakening in equation (5.6).

In order to improve the creep resistance of zirconia and alumina, nano-sized reinforcements have been added to these fine-grained ceramics. These nano-sized particles are believed to reinforce the GB triple junctions, limiting GB sliding. As a result, the high-temperature mechanical loss would be lower and the relaxation peak would be better resolved with respect to the background (Figure 5.5).

5.3.2 How can we improve the high-temperature mechanical properties of zirconia and alumina?

Figure 5.5 shows the influence of nano-reinforcements on the mechanical loss spectrum of zirconia and alumina. It can be seen that addition of CNTs or SiCw to zirconia leads to a decrease in the mechanical-loss spectrum with respect to Z0. On the other hand, additions of SiCp increase the level of damping in zirconia, but decrease the level of damping in alumina.

The decrease of the high-temperature damping may be interpreted as due to the limitation of GB sliding. Limitation of GB sliding through the additions of CNTs or SiCw is also confirmed by creep test in compression. Figure 5.6 shows that the creep strain is much smaller in zirconia composites than in Z0. Thus, addition of CNTs and SiCw increase the creep resistance of zirconia. These results are in good agreement with the mechanical-loss spectra (Figure 5.5): a lower level of the high-temperature damping background means a better creep resistance.
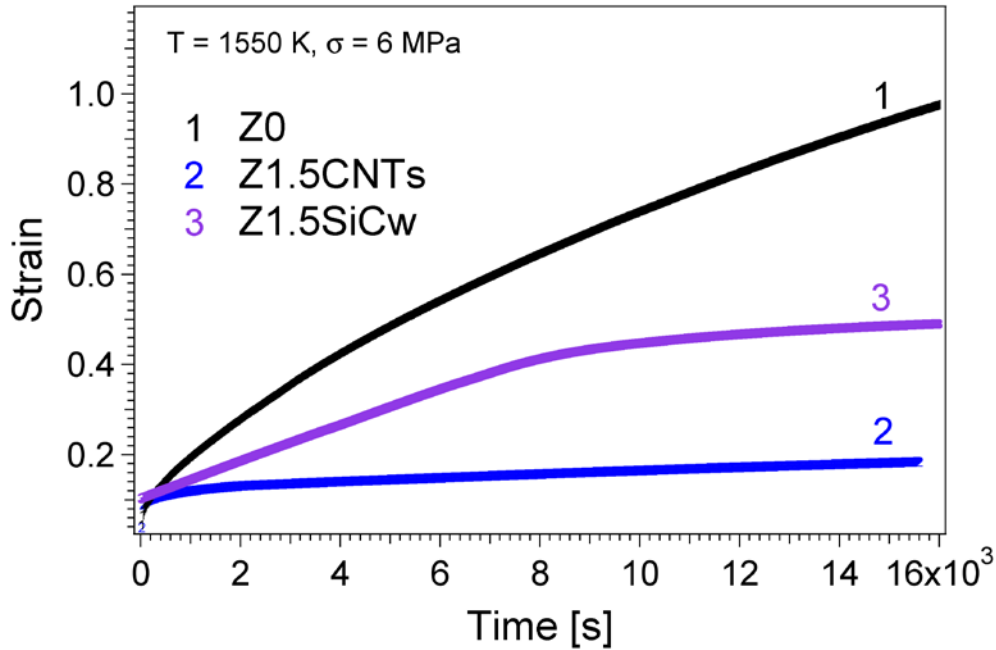
Figure 5.6: Strain recorded as a function of time during compression tests at 1550 K and low stress of 6 MPa in Z0, Z1.5CNTs and Z1.5SiCw.

Therefore, the high-temperature mechanical behavior of reinforced zirconia can be interpreted by the GB sliding model where the triple junctions are pinned with nano-objects (§5.1.2).

However, the pinning efficiency is not as important as it was expected. The high-temperature mechanical loss background is decreased by reinforcements, as it was expected from our model of GB sliding (see §5.1.2), but the relaxation peak due to GB sliding is still not well resolved with respect to the exponential background. The transition from the peak to the exponential background, which accounts for the "interface-reaction" mechanism, is not strongly modified by the reinforcing nano-particles or fibers.

Indeed the GB microstructure evolves with temperature. As a matter of fact, the activation parameters are apparent (too high value of activation enthalpy and too low value of the limit relaxation time) as well in reinforced as in unrein-forced ceramics. As already mentioned, apparent values of the activation para-meters are systematically obtained when microstructure is changing with temperature. In the present case, the result analysis has shown that interface reaction would be a "solution-diffusion-precipitation" process. If this process is controlled by matter diffusion across the triple junction, the energy barrier is the barrier for diffusion. As the GB microstructure changes with temperature, this may lead to an increase in the free volume for diffusion. As a consequence, the energy barrier for diffusion decreases with increasing temperature, and the

mobility of the migrating atoms or molecules increases with temperature more rapidly than by predicted by the classical law of thermal activation. Drawing an Arrhenius plot yields an apparent too high value of the activation enthalpy.

In such a model of creep, where GB sliding is accommodated by a "solution-diffusion-precipitation" process, the nano-sized reinforcements located at the triple junctions are easily overcome by diffusion short circuits. They are only able to delay creep leading to the reduction of creep strain in the low stress regime, as observed in Figure 5.6. As a matter of fact, additions of SiCp to zirconia have not led to a decrease in the high-temperature mechanical loss although these particles were located on the GBs (Figure 5.5). Indeed, adding SiCp to zirconia has induced the formation of amorphous SiO_2 during sintering. This glassy phase is responsible for lubricating the GB sliding process and has then a screening effect on the pinning efficiency of the remaining SiC particles.

From the above results, it can be concluded that nano-sized particles at the triple junctions are perhaps not the best pinning centers for reducing creep. Stronger pinning effect could be obtained by nano-sized fibers such as CNTs or SiCw, which would be entrapped in two adjacent grains. Such configurations have been sometimes observed by TEM (Figure 3.8a and Figure 3.9). In this case, the reinforcing nano-fibers cannot be overcome by GB diffusion, because they are strongly bound to two crystalline grains. They will provide a restoring force, which would be more stable when temperature varies. In order to create such pinning centers, research must be focused on working the wettability of the nano-sized reinforcements on the ceramic grains, in order to favor a strong bonding between the reinforcements and the ceramic grains.

5.4 Proposition for further research

Industrial equipment, particularly advanced technologies, operates more and more in extreme conditions and must be resistant for example to extreme temperature, high pressure, corrosion, erosion, etc. Examples of applications requiring highly resistant materials are turbines, engines, heat exchangers, aerospace, sensors and the chemical industry. A class of materials to be investigated for these applications are the ceramic matrix composites (CMCs).

Here above it has been shown that the mechanical properties of a classical ceramic such as zirconia may be improved by nano-sized reinforcements. The obtained results open an interesting way for the investigation of new CMCs, in which the reinforcing elements are nano-sized objects: alumina or silicon carbide matrices reinforced with CNTs or SiCw. Also, the size of the grain matrix plays an important role on the mechanical behaviour as shown by the results here above.

To control the grain size of the sintered ceramic, SPS (Spark Plasma Sintering) processing may be used. SPS is known to reach high density within nano-crystallized ceramic under lower temperature than conventional high-isostatic pressing (HIP). It will be very interesting to study the thermo-mechanical behaviour of new nano-structured ceramic matrix composites (CMCs), which were processed by SPS, by mechanical spectroscopy, such as for instance:
- nano-structured alumina matrix reinforced with SiC nanoparticles or fibers,
- nano-structured silicon nitride matrix reinforced with carbon nanotubes or SiC fibers.

Conclusions

Polycrystalline zirconia (3Y-TZP grade), unreinforced and reinforced with CNTs or SiCw or SiCp, as well as alumina and SiCp doped alumina have been processed and studied by mechanical spectroscopy with complementary observations of electron microscopy.

The high-temperature mechanical loss spectra of fine-grained zirconia and alumina are mainly composed of a relaxation peak, which turns into an exponential background at higher temperature or lower frequency. The components of these spectra can be interpreted by a theoretical model of GB sliding, in which the grains are separated by an amorphous layer. When GB sliding is not limited by obstacles like three point junctions or GB asperities or other defects, creep occurs and an exponential background (exponential increase with temperature) is observed in the mechanical loss. It was found that additions of nano-sized reinforcements, such as CNTs or SiCw on the GBs of zirconia lead to a decrease in the high-temperature exponential background. Also, addition of SiCp on the GBs of alumina leads to a decrease of the exponential background with respect to pure alumina. According to GB sliding model, this means that GB sliding is more difficult and, as a consequence, a better resistance to creep will be observed.

The creep results obtained in zirconia doped with CNTs or SiCw are in good agreement with the ones performed in mechanical spectroscopy. Creep strain is sensitively reduced in the reinforced ceramics, which exhibit a lower level of the high-temperature mechanical loss background.

The activation parameters obtained from the Arrhenius plots were apparent. Two methods have been used to correct the apparent values. However, even if the corrected values seem more reasonable than the values obtained from the Arrhenius plots, they do not bring useful information. Indeed activation enthalpy values are sometimes surprisingly lower in the case of reinforced materials, in which GB sliding would be more difficult. As all the other obtained results argue for the interpretation of plastic deformation as due to GB sliding, we keep this interpretation and we admit that the apparent too high values of the activation enthalpy account for a change of the GB microstructure with temperature. Thermal change in the GB microstructure is believed to offer short circuit paths for GB diffusion, which allows the pinning nano-sized reinforcements to be overcome reducing their efficiency.

Bibliography

[1] Musikant, S., *What every engineer should know about ceramics*, edited by Marcel Dekker, I. (New York - Basel - Hong Kong, 1990).

[2] Munz, D. and Fett, T., *Ceramics. Mechanical properties, failure behavior, materials selection*, edited by Hull, R., Osgood, R. M., Sakaki, H. and Zunger, A. (Springer series in Materials Science, 2001).

[3] Swain, M., *Structure and properties of ceramics, Materials Science and Technology. A comprehensive treatment. Volume 11*, edited by Cahn, R. W., Haasen, P. and Kramer, E. (Wiley-VCH, 1994).

[4] Scott, H. G., *Phase relations in the zirconia-yttria system*, Journal of Material Science **10**, 1527-1535 (1975).

[5] Stubican, V. S. and Ray, S. P., *Phase equilibria and ordering in the system ZrO_2-CaO* Journal of the American Ceramic Society **60**, 534-537 (1977).

[6] Poluboyarinov, D. N., Kalliga, G. P. and Lyutsareva, L. A., *The question of the stabilization and sintering of high purity zirconium dioxide*, Refractories **4**, 192-197 (1963).

[7] Rew, C., *Electrical conductivity of ceria-stabilized zirconia*, Physica Status Solidi (A) Applied research **1**, 787-794 (1970).

[8] Tietz, F., Buchkremer, H. P. and Stöver, D., *10 years of materials research for solid oxide fuel cells at Forschungszentrum Jülich*, Journal of Electroceramics **17**, 1385-3449 (2006).

[9] Staff, A. I., *Apple seeks patent on radio-transparent zirconia CE casing*, http://www.appleinsider.com/articles/06/11/30/apple_seeks_patent_on_radio_transparent_zirconia_ce_casings.html (2006).

[10] Clarke, D., *On the equilibrium thickness of intergranular glass phases in ceramics materials*, Journal of the American Ceramic Society **70**, 15-22 (1987).

[11] Donzel, L., Conforto, E. and Schaller, R., *High-temperature mechanical spectroscopy of yttria-stabilized tetragonal zirconia polycrystals (Y-TZP) with different amounts of intergranular phase*, Acta Materialia **48**, 777-787 (2000).

[12] Wakai, F., *Superplasticity of ceramics*, Ceramics International **17**, 153-163 (1991).

[13] Wakai, F., Sakaguki, S. and Matsuno, Y., *Superplasticity of yttria-stabilized tetragonal ZrO_2 polycrystals*, Advanced Ceramic Materials **1**, 259-163 (1986).

[14] Wakai, F., Kondo, N. and Shinoda, Y., *Ceramics superplasticity*, Current Opinion

Solid State and Materials Science **4**, 461-465 (1999).

[15] Lakki, A., Schaller, R., Nauer, M. and Carry, C., *High temperature superplastic creep and internal friction of yttria doped zirconia polycrystals*, Acta Metallurgica et Materialia **41**, 2845-2853 (1993).

[16] Chokshi, A. H., Mukherjee, A. K. and Langdon, T. G., *Superplasticity in advanced materials*, Materials Science and Engineering R: Reports **10**, 237-274 (1993).

[17] Domínguez-Rodríguez, A., Gomez-Garcia, D. and Jiménez-Melendo, M., *High temperature plasticity in the ZrO_2-Y_2O_3 system*, Ceramic Engineering and Science Proceedings **19**, 395-406 (1998).

[18] Chokshi, A. H., *An evaluation of the grain boundary sliding contribution to creep deformation in polycrystalline alumina*, Journal of Material Science **25**, 3221-3228 (1990).

[19] Langdon, T. G., *The role of grain boundaries in high temperature deformation*, Materials Science and Engineering **A166**, 67-69 (1993).

[20] Chokshi, A. H., Mukherjee, A. K. and Langdon, T. G., *Superplasticity in ceramics*, Materials Science and Engineering **R10**, 237-274 (1993).

[21] Jiménez-Melendo, M., Domínguez-Rodríguez, A. and Holgado-Salado, M., *Superplastic characteristics of high purity yttria-stabilized zirconia polycrystals*, International Journal of Plasticity **17**, 341-352 (2001).

[22] Jiménez-Melendo, M. and Domínguez-Rodríguez, A., *Like-Metal superplasticity of fine-grained Y_2O_3-stabilized zirconia ceramics*, Philosophical Magazine A **79**, 1591-1608 (1999).

[23] Rouxel, T. and Wakai, F., *The brittle to ductile transition in a Si_3N_4/SiC composite with a glassy grain boundary phase*, Acta Metallurgica et Materialia **41**, 3203-3213 (1993).

[24] Hiraga, K., Yasuda, H. Y. and Sakka, Y., *The tensile creep behavior of superplastic tetragonal zirconia doped with small amounts of SiO_2*, Materials Science and Engineering: A **234-236**, 1026-1029 (1997).

[25] Morita, K., Hiraga, K. and Kim, B. N., *Effect of SiO_2 addition on the creep behavior of superplastic tetragonal ZrO_2*, Acta Materialia **52**, 3355-3364 (2004).

[26] Gremillard, L., *Relation microstructure-durabilité dans une zircone biomédicale*, Nº 0026, École doctorale matériaux de Lyon (2002).

[27] Nabarro, F. R. N., *Deformation of crystals by motion of a single ion. In Strength of solids*, Report of a conference on the Strength of Solids, Physical Society, London, edited by Mott, N. F. (Bristol 7th-9th July, 1947).

[28] Herring, C., *Diffusional viscosity of a polycrystalline solid*, Journal of Applied Phys-

ics **21**, 437-445 (1950).

[29] Coble, R. L., *A model for boundary diffusion controlled creep in polycrystalline materials*, Journal of Applied Physics **34**, 1679-1682 (1963).

[30] Blum, W., *Role of dislocation annihilation during steady-state deformation*, Physica Status Solidi B **45**, 561-571 (1971).

[31] Ashby, M. F., *Boundary defects and mechanism of particle movement through crystals*, Scripta Metallurgica **3**, 843-848 (1969).

[32] Artz, E., Ashby, M. F. and Verrall, R. A., *Interface controlled diffusional creep*, Acta Metallurgica **31**, 1977 (1983).

[33] Burton, B., *Interface reaction controlled diffusional creep: A consideration of grain boundary dislocation climb sources*, Materials Science and Engineering **10**, 9-14 (1972).

[34] Gu, H. and Wakai, F., *Segregation and local structure at grain boundaries in SiO_2-dopped tetragonal ZrO_2 polycrystalline materials*, Journal of Materials Synthesis and Processing **6**, 393-399 (1998).

[35] Raj, R. and Ashby, M. F., *On grain boundary sliding and diffusional creep*, Metallurgical and Materials Transactions B **2**, 1113-1127 (1971).

[36] Mecartney, M. L., *Influence of an amorphous second phase on the properties of yttria-stabilized tetragonal zirconia polycrystals (Y-TZP)*, Journal of the American Ceramic Society **70**, 54-58 (1987).

[37] Hwang, C. M. J. and Chen, I. W., *Effect of a liquid phase on superplasticity of 2-mol % -Y_2O_3 - stabilized tetragonal zirconia polycrystals*, Journal of the American Ceramic Society **73**, 1626-1632 (1990).

[38] Wakai, F., Kondo, N., Ogawa, H., Nagano, T. and Tsurekawa, S., *Ceramics superplasticity: deformation mechanism and microstructure*, Materials Characterization **37**, 331-341 (1996).

[39] Besson, J. L., Rouxel, T. and Goursat, P., *Ductility and creep resistance of a silicon nitride ceramic*, Scripta Materialia **39**, 1339-1343 (1998).

[40] Raj, R. and Chyung, C. K., *Solution-precipitation creep in glass ceramics*, Acta Metallurgica **29**, 159-166 (1981).

[41] Tsai, R. L. and Raj, R., *Creep fracture in ceramics containing small amounts of liquid phase*, Acta Metallurgica **30**, 1043-1058 (1982).

[42] Pharr, G. M. and Ashby, M. F., *On creep enhanced by a liquid phase*, Acta Metallurgica **31**, 129-138 (1983).

[43] Wang, J. W. and Raj, R., *Mechanism of superplastic flow in a fine-grained ceramic containing some liquid phase*, Journal of the American Ceramic Society **67**, 399-409

(1984).

[44] Wakai, F., *Step model of solution-precipitation creep*, Acta Metallurgica et Materialia **42**, 1163-1172 (1994).

[45] Hart, J. L. and Chaklader, A. C. D., *Superplasticity in pure ZrO₂*, Materials Research Bulletin **2**, 521-526 (1967).

[46] Maehara, Y. and Langdon, T. G., *Review: Superplasticity in ceramics*, Journal of Materials Science **25**, 2275-2286 (1990).

[47] Nieh, T. G. and Wadsworth, J., *Ceramics superplasticity*, Annual Review of Materials Science **20**, 117-140 (1990).

[48] Chen, I. W. and Xue, L. A., *Development of superplastic structural ceramics*, Journal of the American Ceramic Society **73**, 2585-2609 (1990).

[49] Kim, B. N., Hiraga, K., Morita, K. and Sakka, Y., *A high-strain-rate superplastic ceramic*, Nature **413**, 288-291 (2001).

[50] Kim, B. N., Morita, K., Hiraga, K., Sakka, Y. and Yamada, T., *Enhanced tensile ductility in ZrO₂- Al₂O₃-spinel composite ceramic*, Scripta Materialia **47**, 775-779 (2002).

[51] Wittenauer, J., *Plastic deformation of ceramics*, 321-331, edited by Bradt, R., Brookes, C. and Routbort, J. L. (Plenum New York, 1995).

[52] Ashby, M. F. and Verrall, R. A., *Diffusion-accommodated flow and superplasticity*, Acta Metallurgica **21**, 149-163 (1973).

[53] Gifkins, R. C., *Grain boundary sliding and its accommodation during creep and superplasticity*, Metallurgical and Materials Transactions B **7A**, 1225-1232 (1976).

[54] Wakai, F., Shinoda, Y., Ishihara, S. and Domínguez-Rodríguez, A., *Topological transformation of grains in superplastic-like deformation*, Acta Materialia **50**, 1177-1186 (2002).

[55] Wakai, F., Akatsu, T. and Shinoda, Y., *Dynamics of grain boundary networks in superplasticity*, Material Science Forum **447-448**, 49-54 (2004).

[56] Jiménez-Melendo, M., Domínguez-Rodríguez, A. and Bravo-León, A., *Superplastic flow of fine-grained yttria-stabilized zirconia polycrystals: constitutive equation and deformation mechanism*, Journal of the American Ceramic Society **81**, 2761-2776 (1998).

[57] Owen, D. M. and Chokshi, A. H., *The high temperature mechanical characteristics of superplastic 3 mol % yttria-stabilized zirconia*, Acta Materialia **46**, 667-679 (1998).

[58] Owen, D. M. and Chokshi, A. H., *Analysis of deformation mechanism in superplastic yttria-stabilized tetragonal zirconia*, International Journal of Plasticity **17**, 353-368 (2001).

[59] Jiménez-Melendo, M. and Domínguez-Rodríguez, A., *High temperature mechanical*

characteristics of superplastic yttria-stabilized zirconia. An examination of the flow process., Acta Materialia **48**, 3201-3210 (2000).

[60] Satou, T., Hosaka, F., Sato, E., Matushita, J., Otsuka, M. and Kuribayashi, K., *Superplastic deformation behavior of undoped and doped high-purity 3Y-TZP*, Materials Science Forum **357-359**, 117-122 (2001).

[61] Balasubramanian, N. and Langdon, T. G., *Flow process in superplastic yttria-stabilized zirconia: A deformation limit diagram*, Materials Science and Engineering: A **409**, 46-51 (2005).

[62] Balasubramanian, N. and Langdon, T. G., *Comment on the role of intergranular dislocations in superplastic yttria-stabilized zirconia*, Scripta Materialia **48**, 599-604 (2003).

[63] Chokshi, A. H., *Diffusion creep in oxide ceramics*, Journal of the American Ceramic Society **22**, 2469-2478 (2002).

[64] Arellano-López, A. R., Domíniguez-Rodríguez, A. and Routbort, J. L., *Microstructural constrains for creep in SiC-whiskers-reinforced Al_2O_3*, Acta Materialia **46**, 6361-6373 (1998).

[65] Chokshi, A. H. and Langdon, T. G., *Characteristics of creep deformation in ceramics*, Material Science and Technology **7**, 577-584 (1991).

[66] Chokshi, A. H., *The effect of pipe diffusion on Harper-Dorn creep and low stresses*, Scripta Metallurgica **19**, 529-534 (1985).

[67] Charit, I. and Chokshi, A. H., *Experimental evidence for diffusion creep in the superplastic 3 mol % yttria-stabilized tetragonal zirconia*, Acta Materialia **49**, 2239-2249 (2001).

[68] Chokshi, A. H., *Observations of the primary regions in the tensile creep deformation of a superplastic zirconia-alumina composite*, Scripta Metallurgica et Materialia **29**, 869-874 (1993).

[69] Wiederhorn, S. M., Roberts, D. E., Chuang, T. J. and Chuck, L., *Damage-enhanced creep in a siliconized silicon carbide: Phenomenology*, Journal of the American Ceramic Society **71**, 602-608 (1988).

[70] Chokshi, A. H., *Superplasticity in fine grained ceramics and ceramic composites: current understanding and future prospects*, Materials Science and Engineering **A166**, 119-133 (1993).

[71] Wakai, F. and Nagano, T., *Effects of solute ion and grain size on superplasticity of ZrO_2 polycrystals*, Journal of Material Science **26**, 241-247 (1991).

[72] Chokshi, A. H., *An evaluation of the grain-boundary sliding contribution to creep deformation in polycrystalline alumina*, Journal of Materials Science **25**, 3221-3228 (1990).

[73] Hines, J. A., Ikuhara, A., Chokshi, A. H. and Sakuma, T., *The influence of the trace impurities on the mechanical characteristics of a superplastic 2 mol % yttria stabilized zirconia*, Acta Materialia **46**, 5557-5568 (1998).

[74] Nieh, T. G., McNally, C. M. and Wadsworth, J., *Superplastic properties of a fine-grained yttria-stabilized tetragonal polycrystal of zirconia*, Scripta Materialia **22**, 1297-1300 (1988).

[75] Wakai, F., *The role of interface controlled diffusion creep on superplasticity of yttria-stabilized tetragonal ZrO_2 polycrystals*, Journal of the Materials Science Letter **6**, 607-609 (1988).

[76] Duclos, R., Crampon, J. and Amana, B., *Structural and topological study of superplasticity in zirconia polycrystals*, Acta Metallurgica **37**, 877-883 (1989).

[77] Domínguez-Rodríguez, A., Bravo-León, A., Ye, J. D. and Jiménez-Melendo, M., *Grain size and temperature dependence of the threshold stress for superplastic deformation in yttria-stabilized zirconia polycrystals*, Materials Science and Engineering: A **247** 97-101 (1998).

[78] Domínguez-Rodríguez, A., Gutiérrez-Mora, F., Jiménez-Melendo, M., Routbort, J. and Chaim, R., *Current understanding of superplastic deformation of Y-TZP and its applications*, Materials Science and Engineering: A **302**, 154-161 (2001).

[79] Domínguez-Rodríguez, A., *Superplasticity of YTZP: New approach and application*, Materials Transactions, JIM **40**, 830-835 (1998).

[80] Ma, Y. and Langdon, T. G., *Critical assessment of flow and cavity formation in a superplastic yttria-stabilized zirconia*, Acta Metallurgica et Materialia **42**, 2753-2761 (1994).

[81] Debschütz, K. D., Caspers, D. B., Schneider, G. A. and Petzow, G., *Critical evaluation of the compression creep test*, Journal of the American Ceramic Society **76**, 2468-2474 (1993).

[82] Nauer, M. and Carry, C., *Creep parameters of yttria doped zirconia materials and superplastic deformation mechanism*, Scripta Metallurgica et Materialia **24**, 1459-1463 (1990).

[83] Lakki, A., *Mechanical spectroscopy of fine-grained zirconia, alumina and silicon nitride*, Ph.D. Thesis Nº 1266, Ècole Polytechnique Fédérale de Lausanne (1994).

[84] Primdahl, S., Tholen, A. and Langdon, T. G., *Microstructural examination of a superplastic yttria-stabilized zirconia: implications for the superplastic mechanism*, Acta Metallurgica et Materialia **43**, 1211-1218 (1995).

[85] Sato, E., Morita, H., Kurubiyashi, K. and Sundararan, D. J., *Effect of small amount of alumina doping on superplastic behavior of tetragonal zirconia*, Journal of Materials Science **34**, 4511-4518 (1999).

[86] Chaudhury, P. K. and Mohamed, F. A., *Effect of impurity content on superplastic flow in the Zn - 22 % Al alloy*, Acta Metallurgica **36**, 1099-1110 (1988).

[87] Chaudhury, P. K., Sivaramakrishnan, V. and Mohamed, F. A., *Superplastic deformation behavior in commercial and high purity Zn-22 % Al*, Metallurgical and Materials Transactions; A: Physical Metallurgy and Materials Science **19 A**, 2741-2752 (1988).

[88] Martinez-Fernandez, J., Jiménez-Melendo, M., Domínguez-Rodríguez, A. and Heuer, A. H., *High-temperature creep of yttria-stabilized zirconia single crystals*, Journal of the American Ceramic Society **73**, 2452-2456 (1990).

[89] Gómez-García, D., Martinez-Fernandez, J., Domínguez-Rodríguez, A. and Westmacott, K. H., *Electron-beam-induced loop formation on dislocations in yttria-fully-stabilized zirconia*, Journal of the American Ceramic Society **79** 2733-2738 (1996).

[90] Domínguez-Rodríguez, A., Gómez-García, D., Lorenzo-Martín, C. and Muñoz-Bernabé, A., *Influence of the yttrium segregation at grain boundaries in the superplasticity of yttria tetragonal zirconia polycrystals*, Journal of the European Ceramic Society **23**, 2969-2973 (2003).

[91] Murty, G. S. and Koczak, *Superplastic behavior of an Al - 4 wt. % Ti alloy processes by a powder metallurgy route*, Materials Science and Engineering **100**, 37-43 (1988).

[92] Berbon, M. Z. and Langdon, T. G., *Examination of the flow process in superplastic yttria-stabilized tetragonal zirconia*, Acta Materialia **47** 2495 (1999).

[93] Berbon, M. Z. and Langdon, T. G., *The variation of strain rate with stress in superplastic zirconia*, Material Science Forum **243-245**, 357-362 (1997).

[94] Winnubst, L., Keizer, K. and Burggraaf, A. J., *Mechanical properties and fracture behavior of ZrO_2 - Y_2O_3*, Journal of Materials Science **18**, 1958-1966 (1983).

[95] Theunissen, G. S. A. M., Winnubst, A. J. A. and Burggraaf, A. J., *Effect of dopants on the sintering behavior and stability of tetragonal zirconia ceramics*, Journal of the European Ceramic Society **9**, 251-263 (1992).

[96] Stemmer, S., Vleugels, J. and Van Der Biest, O., *Grain boundary segregation in high-purity, yttria-stabilized tetragonal zirconia polycrystals (Y-TZP)*, Journal of the European Ceramic Society **18**, 1565-1570 (1988).

[97] Nieh, T. G. and Wadsworth, J., *Superplastic behavior of fine-grained yttria-stabilized, tetragonal zirconia polycrystal (Y-TZP)*, Acta Metallurgica et Materialia **38**, 1121-1133 (1990).

[98] Morita, K. and Hiraga, K., *High temperature deformation behavior of a fine-grained tetragonal zirconia*, Scripta Materialia **42**, 183-188 (1999).

[99] Morita, K., Hiraga, K. and Sakka, Y., *Creep behavior of a fine-grained tetragonal zirconia*, Key Engineering Materials **171-174**, 847-854 (2000).

[100] Morita, K. and Hiraga, K., *Deformed substructures in fine-grained tetragonal zirconia*, Philosophical Magazine Letter **81**, 311-319 (2001).

[101] Bravo-Leon, A., Jimenez-Melendo, M., Dominguez-Rodriguez, A. and Chokshi, A. H., *The role of a threshold stress in the superplastic deformation of fine-grained yttria-stabilized zirconia polycrystals*, Scripta Materialia **34**, 1155-1160 (1996).

[102] Guitiérez-Mora, F., Domínguez-Rodríguez, A., Jiménez-Melendo, M., Chaim, R. and Hefetz, R., *Creep of nanocrystalline Y-TZP ceramics*, Nanostructured Materials **11**, 531-537 (1999).

[103] Domínguez-Rodríguez, A., Lagerlöf, K. P. D. and Heuer, A. H., *High-temperature precipitation hardening of two-phase Y_2O_3 partially stabilized ZrO_2 single crystals: a first report*, Journal of the American Ceramic Society **69**, 281-284 (1986).

[104] Cannon, W. R. and Langdon, T. G., *Review: Creep of ceramics*, Journal of Materials Science **23**, 1-20 (1988).

[105] Morita, K. and Hiraga, K., *Critical assessment of high-temperature deformation and deformed microstructure in high-purity tetragonal zirconia containing 3 mol. % yttria*, Acta Materialia **50**, 1075-1085 (2002).

[106] Davies, C. K. L. and Sinha Ray, S. K., *Special Ceramics*, edited by P. Popper (The British Ceramic Research Association , Stroke-on-Trent, UK, 1972).

[107] Sudhir, B. and Chokshi, A. H., *Compression Creep Characteristics of 8-mol%-Yttria-Stabilized Cubic-Zirconia*, Journal of the American Ceramic Society **84**, 2625-2632 (2001).

[108] Kottada, R. S. and Chokshi, A. H., *The high temperature tensile and compressive deformation characteristics of magnesia doped alumina*, Acta Materialia **48**, 3905-3915 (2000).

[109] Chokshi, A. H., *On the emergence of new surface grains during superplastic deformation*, Scripta Materialia **44**, 2611-2615 (2001).

[110] Chokshi, A. H., *Role of diffusion creep in the superplastic deformation of 3 mol% yttria stabilized tetragonal zirconia*, Scripta Materialia **42**, 241-248 (2000).

[111] Kohlrausch, R., Annalen der Physik **12**, 393 (1847).

[112] Zener, C., *Elasticity and anelasticity of metals*, edited by Zener, C. (University of Chicago Press, Chicago, Illinois, 1948).

[113] Nowick, A. S. and Berry, B. S., *Anelastic relaxation in crystalline solids*, edited by Alper, A. M., Margrave, L. J. and Nowick, A. S. (Acad. Press New York and London, 1972).

[114] Schaller, R., Fantozzi, G. and Gremaud, G., *Mechanical Spectroscopy Q^{-1} 2001 with Application to Materials Science*, edited by Schaller, R., Fantozzi, G. and Gremaud, G.

(TRANS TECH PUBLICATIONS LTD, Switzerland - Germany - UK - USA, 2001).

[115] Fantozzi, G., *Phenomenology and definitions*, 3-31, edited by Schaller, R., Fantozzi, G. and Gremaud, G. (TRANS TECH PUBLICATIONS LTD, Switzerland - Germany - UK - USA, 2001).

[116] Schoeck, G., Bisogni, E. and Shyne, J., The activation energy of high temperature internal friction, Journal **12**, 1466-1468 (1964).

[117] Weller, M., *Defects in oxide ceramics and their characterization - General properties of oxides*, Journal of Materials Education **17**, 1-32 (1995).

[118] Lakki, A., Schaller, R., Carry, C. and Benoit, W., *High-temperature anelastic and viscoplastic deformation of fine-grained MgO-doped Al_2O_3*, Journal of the American Ceramic Society **82** 2181-2187 (1998).

[119] Koehler, *Imperfections in nearly perfect crystal*, Symposium held at Pocono Manor, Penna., U. S. A., 12-14 October 1950, Willey, New York; 1950; London: Chapman and Hall. , edited by Shocley, W., Hollomn, J. H., MAURER, R. and SEITZ, F., 1952).

[120] Granato, A. V. and Lücke, K., *Theory of the mechanical damping due to dislocations*, Journal of Applied Physics **27**, 583 (1956).

[121] Gremaud, G., *Dislocation string models*, 190-192, edited by Schaller, R., Fantozzi, G. and Gremaud, G. (TRANS TECH PUBLICATIONS LTD, Switzerland - Germany - UK - USA, 2001).

[122] Gruffel, P., *Évolution structurales d'alumines à grains fins dopées a l'yttrium et fluage superplastique*, Ph.D. Thesis Nº 951, Ècole Politechnique Fédérale de Lausanne (1991).

[123] Zener, C., *Theory of elasticity of polycrystals with viscous grain boundaries*, Physical Review **60**, 906-908 (1941).

[124] Kê, T. S., *Experimental evidence of the viscous behavior of grain boundaries in metals*, Physical Review **71**, 533-546 (1947).

[125] Kê, T. S., *Viscous slip along grain boundary and diffusion of zinc in alpha-brass*, Applied Physics **19**, 285-290 (1948).

[126] Daraktchiev, M., *High-temperature mechanical loss in yttria-stabilized tetragonal zirconia and in calcium hexaluminate*, Ph.D. Thesis Nº 2802, Ècole Polytechnique Fédérale de Lausanne (2003).

[127] Daraktchiev, M. and Schaller, R., *Mechanical loss in 3 mol % yttria doped tetragonal zirconia polycrystals (3Y-TZP)*, Defect and Diffusion Forum **206-207**, 163-167 (2002).

[128] Daraktchiev, M. and Schaller, R., *High temperature mechanical loss behavior of 3 mol % yttria-stabilized tetragonal zirconia polycrystals (3Y-TZP)*, Physica Status Solidi

A **195**, 293-304 (2003).

[129] Mosher, D. R., Raj, R. and Kossowski, R., *Measurement of viscosity of the grain-boundary phase in hot-pressed silicon nitride*, Journal of Materials Science **11**, 49-53 (1976).

[130] Schoeck, G., *The activation energy of dislocation movement*, Physica Status Solidi **8**, 449-507 (1965).

[131] Daraktchiev, M. and Schaller, R., *High temperature mechanical spectroscopy and creep of calcium hexaluminate*, Materials Science and Engineering: A **370**, 199-203 (2003).

[132] Daraktchiev, M., Schaller, R. and Testu, S., *Creep behavior of ceramics studied by mechanical loss measurements*, Materials Science and Engineering A **387-389 (1-2 SPEC. ISS.)**, 687-691 (2004).

[133] Dorn, J. E., *Some fundamental experiments on high temperature creep*, Journal of the Mechanics and Physics of Solids **8**, 85-116 (1954).

[134] Donzel, L., *Intra- and intergranular high-temperature mechanical loss in zirconia and silicon nitride*, Ph.D. Thesis Nᵒ 1851, Ècole Polytechnique Fédérale de Lausanne (1998).

[135] Couteau, E., Hernadi, K., Seo, J. W., Thien-Nga, L., Miko, C., Gaal, R. and Forro, L., *CVD synthesis of high-purity multiwalled carbon nanotubes using CaCO₃ catalyst support for large-scale production*, Chemical Physics Letter **378**, 9-17 (2003).

[136] Magrez, A., Seo, J. W., Miko, C., Hernadt, K. and Forro, L., *Growth of Carbon Nano-tubes with Alkaline Earth Carbonate as Support*, Journal of Physical Chemistry B **109**, 10087-10091 (2005).

[137] Sammalkorpi, M., Krasheninnikov, A., Kuronen, A., Nordlund, K. and Kaski, K., *Mechanical properties of carbon nanotubes with vacancies and related defects*, Physical Review B **70**, 2454161-24541618 (2004).

[138] Forro, L., Salvetat, J.-P., Bonard, J.-M., Bacsa, R., Thomson, N. H., Garaj, S., Thien-Nga, L. R., Gaal, R., Kulik, A., B., R., Degiorgi, L., Bachtold, A., Schonenberger, C., Pekker, S. and Hernadi, K., *Electronic and mechanical properties of carbon nanotubes in Science and Application of Nanotubes*, edited by   (Springer U.S., 297-320, 1999).

[139] Lukic, B., Seo, J. W., Couteau, E., Lee, K., Gradecak, L., Berkecz, R., Hernadi, K., Delpeux, S., Cacciaguerra, T., Béguin, F., B., N. J., Csanyi, G., Kiss, A., Kulik, A. J. and For-ro, L., *Elastic modulus of multi-walled carbon nanotubes produced by catalytic chemical vapor deposition* Applied Physics **A 80**, 695-700 (2005).

[140] Qian, D., W., G. J., Wing, K. L., Ming-Feng, Y. and Rodney, S. R., *Mechanics of carbon nanotubes*, Applied Mechanics Reviews **55**, 495-533 (2002).

[141] Schwartz, M., *Handbook of structural ceramics* edited by Schwartz, M.

(McGraw-Hill, Inc, 1992).

[142] Bjork, L. and Hermansson, L. A. G., *Hot isostatically pressed alumina - silicon carbide whiskers composites*, Journal of the American Ceramic Society **72**, 1436-1438 (1989).

[143] Ohji, T., *Creep inhibition of ceramic/ceramic nanocomposites*, Scripta Materialia **44**, 2083-2086 (2001).

[144] Niihara, K., *New design concept of structural ceramics. Ceramic nanocomposites*, Journal of Ceramic Society Japan. International ed. **99** 523-526 (1991).

[145] Niihara, K. and Nakahira, A., *Particle-Strengthened oxide ceramics, nanocomposite*, Advanced Structural Inorganic Composites, Elsevier Science Publishing, edited by Vincentini, P. (Trieste, Italy, 1990).

[146] Nikahira, A., Sekino, T., Suzuki, Y. and Niihara, K., *Creep and deformation behavior of Al_2O_3/SiC nanocomposites*, Annales de Chimie (Paris) **18**, 403-408 (1993).

[147] Sciti, D., Vicens, J. and Bellosi, A., *Microstructure and properties of alumina-SiC nanocomposites prepared from ultrafine powders*, Journal of Materials Science **37**, 3747-3758 (2002).

[148] Bellosi, A., Sciti, D. and Guicciardi, S., *Synergy and competition in nano- and micro-design of structural ceramics*, Journal of the European Ceramic Society **24**, 3295-3302 (2004).

[149] Nikahira, A. and Niihara, K., *Sintering behaviors and consolidation process for Al2O3/SiC nanocomposites*, Journal of Ceramic Society Japan **100**, 448-453 (1992).

[150] Stearns, L. C., Zhao, J. and Harmer, M. P., *Processing and microstructure development in Al_2O_3 - SiC nanocomposites*, Journal of the European Ceramic Society **10**, 473-477 (1992).

[151] Stearns, L. C. and Harmer, M. P., *Particle-Inhibited Grain Growth in AI_2O_3-SiC: I, Experimental Results*, Journal of the American Ceramic Society **79**, 3013-3119 (1996).

[152] Xue, Y., Zangvil, A. and Kerber, A., *SiC nanoparticles-reinforced Al_2O_3 matrix composites: Role of intra- and intergranular particles*, Journal of the European Ceramic Society **17**, 921-928 (1997).

[153] Deng, J. Y., Shi, J. L., Zhang, Y. F., Jiang, D. Y. and Guo, J. K., *Pinning effect of SiC particles on mechanical properties of Al_2O_3-SiC ceramic matrix composites*, Journal of the European Ceramic Society **18**, 501-508 (1998).

[154] Gadaud, P., Guisolan, B., Kulik, A. and Schaller, R., *Apparatus for high-temperature internal friction differential measurements*, Review of Science Instruments **61**, 2671-1675 (1990).

[155] Tsukamoto, T., Triskone, G., Genoud, G. Y., Wang, K. Q., Janod, E., Junod, A. and

Müller, J., *Preparation and superconducting properties of high-quality Bi - 2212 ceramics*, Journal of Alloys and Compounds **209**, 225-229 (1994).

[156] Feusier, G., *Études des propriétés mécaniques a haut température des cermets Ti(C, N)-Mo-Co par mesures de frottement interne et par essai de flexion trois points*, Ph.D. Thesis Nº 1659, Ècole Polytechnique Fédérale de Lausanne (1997).

[157] Weller, M. and Schubert, H., *Internal Friction, Dielectric Loss, and Ionic Conductivity of Tetragonal ZrO_2 - 3 % Y_2O_3 (3Y-TZP)*, Journal of the American Ceramic Society **69**, 573-577 (1986).

[158] Weller, M., *Point defect relaxation - Defects in oxides in Mechanical Spectroscopy Q^{-1} 2001 with Application to Materials Science*, 95-137, edited by Schaller, R., Fantozzi, G. and Gremaud, G. (TRANS TECH PUBLICATIONS LTD, Switzerland - Germany - UK - USA, 2001).

[159] Poirier, J. P., *Creep polygonization and dynamic recrystallisation in Creep of crystals. High temperature deformation processes in metals, ceramics and minerals*, 169-1993, edited by Cook, A. H., Harland, W. B., Hughes, N. F. P. A., Sclater, J. G. and Thomson, M. R. A. (Cambridge University Press, Cambridge, 1985).

[160] Schaller, R., *Mechanical spectroscopy of the high-temperature brittle-to-ductile transition in ceramics and cermets*, Journal of Alloys and Compounds **310**, 7-15 (2000).

[161] Wert, C. and Marx, J., *A new method for determining the heat of activation for relaxation processes*, Acta Metallurgica **1**, 113-115 (1953).

[162] Escaig, B. and Lefebvre, J. M., *Thermodynamic and kinetic analysis of non elastic deformation in polymeric glasses*, Revue de Physique Appliquée **13**, 285 (1978).

[163] French, J. D., Zhao, J., Harmer, M. P., Chan, H. M. and Miller, G. A., *Creep of Duplex Microstructures*, Journal of the American Ceramic Society **77**, 2857-2865 (1994).

Acknowledgments

Curriculum Vitae

Claudia IONASCU

born on December 22nd, 1975 in Onesti, Romania
nationality: Romanian

Education:

2004-2007:	PhD. Student at EPF Lausanne, Institute of Physics of Complex Mater under direction of Prof. R. Schaller.
1999-2000:	Master at West University of Timisoara, Faculty of Physics, Romania Dissertation work: *Study of the dynamic processes of ferrites*.
1994-1998:	Physical-Chemistry at West University of Timisoara, Faculty of Physics, Romania Diploma work: *Lasers with active solid media*.

Teaching:

2007	Assistant for "Introduction à la Métrologie", 1st year, Materiaux, with G. Gremaud and R. Schaller
2006-2007	Assistant for "Travaux pratiques du physique - Mécanique de solides", 2nd year, Physics, with G. Gremaud
2005-2006	Assistant for "Travaux pratiques du physique - Physique de matériaux", 2nd year, Physics, with G. Gremaud
2005	Assistant for "Introduction à la Métrologie", 1st year, Physics, with G. Gremaud and R. Schaller
2004	Assistant for "Travaux pratiques du physique - Optique", 1st year, Science de la Vie, with R. Schaller

Conferences:

IIAPS XI Imperfections Interactions and Anelastic Phenomena in Solids, Tula, Rusia, 2007.
Oral presentation entitled: *High temperature mechanical loss spectrum of 3Y-TZP zirconia reinforced with carbon nanotubes or silicon carbide whiskers.* (C. Ionascu and R. Schaller).

Journées Annuelles du Groupe Français de la Céramique, Cherbourg, France, 2007
Oral presentation entitled: *Carbone nanotubes et carbure de silicium whiskers en zircone: l'influence en microstructure et les propretés mécanique.* (C. Ionascu and R. Schaller).

10th European Inter-regional Conference on Ceramics, Swansea, UK, 2006
Oral presentation entitled: *Effect of SiC particles on the mechanical loss of alumina.* (C. Ionascu, D. Sciti and R. Schaller).

Journées Annuelles du Groupe Français de la Céramique, Toulouse, France, 2006
Poster entitled: *High-temperature mechanical behavior of 3Y-TZP zirconia doped with carbon nanotubes.* (C. Ionascu and R. Schaller).

Annual meeting of the Swiss Physical Society, Lausanne, Switzerland, 2005
Poster entitled: *High-Temperature Mechanical Behavior of Reinforced 3Y-TZP with MWCNTs or SiCw.* (C. Ionascu and R. Schaller).

14th International Conference on Internal Friction and Mechanical Spectroscopy, Kyoto, Japan, 2005
Oral presentation entitled: *Influence of carbon nanotubes and silicon carbide whiskers on the mechanical loss due to grain boundary sliding in 3 mol%-yttria stabilized zirconia polycrystals.* (C. Ionascu and R. Schaller).

Journées Annuelles du Groupe Français de la Céramique, Paris, France, 2005
Poster entitled: *High-temperature mechanical behavior of 3Y-TZP zirconia doped with carbon nanotubes.* (C. Ionascu and R. Schaller).

9th European Inter-regional Conference on Ceramics, Bardoneccchia, Italy, 2004
Poster entitled: *Carbon nanotubes in 3Y-TZP zirconia: Influence on microstructure and mechanical properties.* (B. Van de Moortèle, C. Ionascu, M. Daraktchiev, and R. Schaller).

Publications:

Ionascu, C and Schaller, R, *High temperature mechanical loss spectrum of 3Y-TZP zirconia reinforced with carbon nanotubes or silicon carbide whiskers*, to be published in Solid State Phenomena.

C. Ionascu, D. Sciti and R. Schaller, *Effect of SiC particles on the mechanical loss of alumina*, Proceeding of the 10th European Inter-regional Conference on Ceramics, Ed. B. Wilshire, M. R. Bache, Swansea Materials Research, pp. 151-156, Swansea, U.K., September 3-5, 2006.

C. Ionascu and R. Schaller, *Influence of carbon nanotubes and silicon carbide whiskers on the mechanical loss due to grain boundary sliding in 3-mol% yttria-stabilized tetragonal zirconia polycrystals*, Materials Science and Engineering A, Vol. 442, pp. 175-178, 2006.

B. Van de Moortèle, C. Ionascu, M. Daraktchiev, R. Schaller, "*Carbon nanotubes in 3Y-TZP zirconia: Influence on microstructure and mechanical properties*", Proceeding of the 9th European Inter-regional Conference on Ceramics, Ed. Alfredo Negro and Laura Montanaro, pp. 307-312, Bardonecchia, Italy, September 5-7, 2004.

I. Mihalca, A. Ercuta, Ionascu, C., *The Villari effect in Fe–Cr–B amorphous ribbons*, Sensors and Actuators A, Vol. 106, pp. 61-64, 2003.